CrossMark

J. Fluid Mech. (2021), *vol*. 907, A26. © The Author(s), 2020.
Published by Cambridge University Press
doi:10.1017/jfm.2020.827

Enhanced velocity fluctuations in interacting swimmer suspensions

Sankalp Nambiar[1],‡, **Piyush Garg**[1] **and Ganesh Subramanian**[1],†

[1]Engineering Mechanics Unit, Jawaharlal Nehru Centre for Advanced Scientific Research, Jakkuru, Bangalore 560064, India

(Received 19 December 2019; revised 22 September 2020; accepted 25 September 2020)

This paper characterizes the nature of velocity fluctuations in swimmer suspensions by determining the fluid velocity variance and the diffusivity of immersed passive tracers in dilute suspensions of hydrodynamically interacting slender microswimmers. The swimmers considered include straight-swimmers whose orientations change only on account of hydrodynamic interactions, and run-and-tumble particles (RTPs) whose orientations change in addition due to tumble events obeying Poisson statistics. In a dilute non-interacting swimmer suspension, the fluid velocity variance is finite and the covariance is short ranged, decaying for distances larger than the swimmer length. In contrast, we show, for a suspension of interacting straight-swimmers, that pair interactions lead to a non-decaying velocity covariance, and a variance that diverges logarithmically with system size. For suspensions of RTPs, the aforementioned divergence is arrested due to tumbling. While the variance remains finite, and the covariance short ranged, for suspensions of interacting rapid tumbling RTPs (short run lengths), the underlying straight-swimmer divergence manifests as a logarithmic increase of the variance with the swimmer run length for persistent RTPs (long run lengths), with a correspondingly long-ranged covariance. The tracer mean squared displacement undergoes an increasingly broad crossover from the ballistic to the diffusive regime for persistent RTPs, with the tracer diffusivity exhibiting a stronger linear increase with the swimmer run length. Our analysis explains the bifurcation of the velocity variance and tracer diffusivities between pusher and puller suspensions, as well as numerous observations of a volume-fraction-dependent crossover time for passive tracer dynamics.

Key words: micro-organism dynamics, suspensions, particle/fluid flow

1. Introduction

Suspensions of rear-actuated swimming microorganisms (pushers), such as bacteria *Escherichia coli* and *Bacillus subtilis*, exhibit a state of large-scale coherent motion that arises, in part, due to long-ranged hydrodynamic interactions (Simha & Ramaswamy 2002; Toner, Tu & Ramaswamy 2005; Saintillan & Shelley 2007, 2008; Underhill, Hernandez-Ortiz & Graham 2008; Subramanian & Koch 2009; Ramaswamy 2010;

† Email address of correspondence: sganesh@jncasr.ac.in
‡ Present address: Nordita, KTH Royal Institute of Technology and Stockholm University, Stockholm 10691, Sweden.

https://doi.org/10.1017/jfm.2020.827 Published online by Cambridge University Press

Koch & Subramanian 2011; Subramanian & Nott 2011; Underhill & Graham 2011; Marchetti *et al.* 2013; Krishnamurthy & Subramanian 2015; Clement *et al.* 2016). Experiments (Dombrowski *et al.* 2004; Gachelin *et al.* 2014) and simulations (Saintillan & Shelley 2007; Wensink *et al.* 2012; Krishnamurthy & Subramanian 2015) have shown that the transition to collective dynamics occurs beyond a threshold concentration, leading to 'bacterial turbulence' (Aranson *et al.* 2007; Sokolov *et al.* 2009; Sokolov & Aranson 2012; Wensink *et al.* 2012); very recent experiments, in fact, point to the dominant role of hydrodynamic interactions in this regard (Colin, Drescher & Sourjik 2019). This state of collective motion or bacterial turbulence is characterized by length and time scales much larger than the elementary microscopic scales that characterize bacterial swimming (for instance, the run length and inverse tumble frequency characterizing the run-and-tumble motion of *E. coli*; see Berg (1993)), and therefore, has important consequences for both transport and rheology; experiments and mean-field theories have shown a reduction in viscosity, leading to apparent superfluidity and unexpected shear-banding behaviour (Sokolov & Aranson 2009; Saintillan 2010; Lopez *et al.* 2015; Nambiar, Nott & Subramanian 2017; Guo *et al.* 2018; Laxminarsimharao, Garg & Subramanian 2018; Saintillan 2018; Liu, Zhang & Cheng 2019; Nambiar *et al.* 2019; Martinez *et al.* 2020). The transition to collective motion has often been inferred from an anomalous enhancement in the diffusivities of passive tracer particles (Wu & Libchaber 2000; Chen *et al.* 2007; Underhill *et al.* 2008; Leptos *et al.* 2009; Lin, Thiffeault & Childress 2011; Jepson *et al.* 2013; Kasyap, Koch & Wu 2014; Krishnamurthy & Subramanian 2015; Thiffeault 2015; Stenhammar *et al.* 2017; Bárdfalvy *et al.* 2019).

A large body of theoretical work studying swimmer suspensions has relied on phenomenological and mean-field models (Simha & Ramaswamy 2002; Aranson *et al.* 2007; Saintillan & Shelley 2008; Underhill *et al.* 2008; Subramanian & Koch 2009; Wensink *et al.* 2012; Dunkel *et al.* 2013*a*,*b*; Marchetti *et al.* 2013; Heidenreich *et al.* 2016). For a dilute swimmer suspension, stability analysis within a mean-field framework has shown that it is the long-ranged hydrodynamic interactions (Saintillan & Shelley 2008; Underhill *et al.* 2008; Subramanian & Koch 2009) between pushers and the mutually reinforcing orientation and velocity fluctuations that are responsible for the said transition to collective motion. Recently, however, there have been a few efforts that have attempted to address the role of interactions, and their role on the onset of collective motion (Stenhammar *et al.* 2017; Qian, Kramer & Underhill 2017; Bárdfalvy *et al.* 2019). Qian *et al.* (2017) wrote down a kinetic equation for the position–orientation phase space swimmer probability density in two dimensions, with an additional nonlinear stochastic noise term to represent fluctuations that emerge from correlated swimming. For small fluctuations, the authors were able to linearize the governing equations, and solve them numerically. The numerics was complemented with analytical expressions, albeit, in the limit of weak swimmer persistence; that is to say, in the limit of the run length being much smaller than the swimmer length. While the authors were able to predict enhanced tracer diffusivities in suspensions of pushers and long-ranged correlations, owing to the limitation of employing a mean-field equation with an *ad hoc* stochastic fluctuation term, the role of swimmer persistence could not be ascertained. Stenhammar *et al.* (2017), on the other hand, carried out large-scale lattice-Boltzmann simulations with $O(10^6)$ swimmers, and complemented the simulations with a kinetic theory appropriate for interacting 'shakers' – particles that generate an active disturbance in the fluid, but do not swim. While both the aforementioned studies were able to sample concentration regimes up until the collective motion threshold, analytical expressions were nevertheless available only in the weak- or no-swimming limit.

https://doi.org/10.1017/jfm.2020.827 Published online by Cambridge University Press

Persistent swimming is, however, a crucial underlying element in the physics of swimmer suspensions. The early simulations that rigorously incorporated the effects of interswimmer hydrodynamic interactions (Underhill *et al.* 2008; Saintillan & Shelley 2011; Underhill & Graham 2011), observing signatures of collective motion in the process, had swimmers whose orientations changed solely on account of hydrodynamic interactions, and thereby remained correlated in the time taken to swim through the computational domain (periodic box). Persistent swimmers have, in fact, been found to develop long-ranged correlations even in the absence of collective motion (Saintillan & Shelley 2011; Underhill & Graham 2011; Krishnamurthy & Subramanian 2015; Stenhammar *et al.* 2017; Bárdfalvy *et al.* 2019). That persistent swimming is also imperative to the onset of collective motion in a dilute swimmer suspension may be seen from the following argument. With the neglect of passive (stabilizing) stresses, the threshold for the onset of collective motion, in a suspension of run-and-tumble swimmers, may be written in the form $nUL^2\tau = 5/C$ (Subramanian & Koch 2009); here, n is the swimmer number density, U the swimming speed, L the swimmer length and τ the inverse tumble frequency, with C being a non-dimensional dipole strength (also interpreted as a measure of the strength of the disturbance field relative to the swimming speed). Assuming C to be $O(1)$ for a typical microscopic swimmer, the above threshold may be rewritten as $(nL^3)(U\tau/L) \sim O(1)$, where nL^3 is the swimmer (hydrodynamic) volume fraction and $U\tau/L$, the non-dimensional run length, is a measure of swimmer persistence. In the dilute regime, $nL^3 < O(1)$, implying that one must have $U\tau/L$ greater than order unity, in order to have a transition to a state of collective motion. In other words, a dilute swimmer suspension can transition to a state of turbulence only if the individual swimmers are persistent. Therefore, an analysis of the onset of collective motion in the theoretically amenable case of a dilute swimmer suspension should ideally resolve the likely subtle transition between the long-ranged bare correlations that arise due to the disturbance velocity fields of individual persistent swimmers, and the longer-ranged correlations induced by long wavelength velocity fluctuations that become dominant close to the threshold.

In the present work, we go beyond the limiting mean-field assumption, and analyse hydrodynamically induced correlations in a swimmer suspension for arbitrary values of the swimmer persistence (as defined by the parameter $U\tau/L$ above). The emphasis in this paper is on the aforementioned bare correlations, that develop between persistent swimmers, even in the absence of collective motion. The nature of correlations induced by 'collective modes' (long wavelength orientation and velocity fluctuations that characterize collective motion) will be reported in a future communication. While the present effort, in effect, determines the bulk correlation length for an unsheared swimmer suspension, as a function of the individual swimmer persistence, and prior to onset of the turbulent regime, the analysis may also be of relevance to suspensions under confinement. The primary focus of the early efforts referenced above was on statistically characterizing the bulk turbulent state of a swimmer suspension via appropriate spatio-temporal measures. In contrast, more recent efforts (Woodhouse & Goldstein 2012; Lushi, Wioland & Goldstein 2014; Pushkin & Yeomans 2014; Wioland, Lushi & Goldstein 2016; Wu *et al.* 2017) have attempted to characterize the seemingly spontaneous transition from the bulk disorderly flow to a coherent one with increasing confinement. Some of these efforts (Lushi *et al.* 2014; Wioland *et al.* 2016) do indicate that the transition occurs when the confining length scale is of order the aforementioned bulk correlation length (in which case, the analysis here suggests that a suspension of more persistent swimmers would exhibit this transition for a weaker confinement). However, more recent efforts suggest a more involved scenario (Wu *et al.* 2017).

https://doi.org/10.1017/jfm.2020.827 Published online by Cambridge University Press

We show, for the first time, that the interplay of swimming with long-ranged hydrodynamic interactions leads to a larger velocity variance and, thence, larger tracer diffusivities, in suspensions of run-and-tumble pushers *vis-á-vis* pullers (the swimming mechanism for pullers is front-actuated, as is typically the case for algae; see Kessler (1986); Saintillan & Shelley (2007); Lauga & Powers (2009); Saintillan (2010); Koch & Subramanian (2011); Guasto, Rusconi & Stocker (2012); Goldstein (2015); Krishnamurthy & Subramanian (2015)). This correlation-induced enhancement in the velocity variance for pushers exhibits a logarithmic scaling for large but finite swimmer persistence ($U\tau/L \gg 1$), eventually culminating in a logarithmic divergence in the straight-swimmer (pusher) limit; the latter divergence has indeed been observed in earlier simulations (Underhill & Graham 2011). The prediction of larger velocity fluctuations in pusher suspensions is consistent with more recent simulations which have revealed a bifurcation of the fluid velocity variance in pusher and puller suspensions with increasing swimmer concentration (Krishnamurthy & Subramanian 2015; Stenhammar *et al.* 2017; Bárdfalvy *et al.* 2019).

The remainder of the manuscript is organized as follows. Before delving into the detailed analysis in subsequent sections, we first obtain the principal results concerning both the velocity variance and tracer diffusivities, using scaling arguments alone, in § 2. The arguments for the velocity variance serve as an interesting contrast to sedimenting suspensions of passive spherical particles, where the nature of velocity fluctuations have previously attracted a considerable amount of interest, following the initial prediction of a divergent velocity variance in the dilute limit (Caflisch & Luke 1985; Guazzelli & Hinch 2011). In § 3, we examine the fluid velocity covariance in a suspension of slender swimmers. Following the formulation of the general expression, in § 3.1, we determine the covariance for suspensions of non-interacting swimmers. In this case, the covariance is independent of the mechanism by which the swimmer orientation decorrelates, since the decorrelation events are assumed to not have an accompanying velocity signature. The resulting covariance is short ranged, starting off with an $O(nL^3)$ plateau (the finite variance at this order), and transitioning to an $O(1/r)$ decay for separations greater than the swimmer length ($r \gg 1$, r being the non-dimensional distance in units of the swimmer length). Since swimmer pair-correlations depend sensitively on the degree of swimmer persistence, it is necessary to discuss the velocity fluctuations in suspensions of interacting straight-swimmers and run-and-tumble particles (RTPs) separately. In § 3.2, we examine the covariance of a dilute suspension of interacting straight-swimmers. The calculation of pair-correlations requires determining the steady-state pair-probability density, to $O(nL^3)^2$, in position–orientation (phase) space. This, in turn, requires obtaining an expression for the rotation rate experienced by a slender swimmer, due to the disturbance velocity field generated by another, and this is derived in appendix A. Even with known disturbance velocity fields, and the associated rates of rotation, the calculation of the pair-probability density is in general a difficult exercise owing to the complex functional form of the velocity fields. For slender swimmers, however, a simplification arises owing to the disturbance velocity being smaller than the swimming speed by the inverse logarithm of the (large) swimmer aspect ratio κ. This allows one to perturb about the leading-order uncorrelated state by expanding in the small parameter $(\ln\kappa)^{-1}$, and the pair-correlations at leading order develop due to cumulative rotation of one swimmer by the other's disturbance field along straight trajectories determined by swimming. With the simplification that arises for slender swimmers above, the phase space pair-probability density for straight-swimmers, to $O(\ln\kappa)^{-1}$ is directly obtained in terms of generalized functions. It is this generalized functional form of the pair-probability that yields a logarithmically divergent variance in a suspension of interacting straight-swimmers.

https://doi.org/10.1017/jfm.2020.827 Published online by Cambridge University Press

Next, in § 3.3, the pair-probability density is determined in closed form, again to $O(\ln\kappa)^{-1}$ for RTPs, and is now additionally a function of the dimensionless run length $U\tau/L$. Recovering the result for straight-swimmers involves a subtle limiting process, and this is explained in appendix B. The correlated component of the variance, at $O(nL^3)^2$, obtained using the pair-probability density for RTPs, is shown to scale linearly with $U\tau/L$ in the limit $U\tau/L \ll 1$, while increasing logarithmically in the limit $U\tau/L \gg 1$ corresponding to persistent swimmers; straight-swimmers correspond to $U\tau/L \to \infty$, and therefore, a logarithmically divergent correlated variance as mentioned above. For $U\tau/L \ll 1$, the correlated component of the covariance transitions directly from the variance plateau for $r \ll 1$ to an $O(1/r)$ far-field decay for $r \gg 1$, this scaling behaviour being similar to the non-interacting component of the variance at $O(nL^3)$. However, for large $U\tau/L$, the correlated covariance becomes long-ranged. Starting from the variance plateau, the correlated component of the covariance only exhibits a weak decay in the interval $1 \ll r \ll U\tau/L$, and transitions to an $O(1/r)$ far-field decay only for $r \gg U\tau/L$; the covariance remains non-decaying in the singular straight-swimmer limit. The aforementioned weak decay of the covariance in the intermediate regime ($1 \ll r \ll U\tau/L$) turns out to be a logarithmic one, and this is established using an alternate matched asymptotic expansions approach in appendix C. Next, in § 4, we study the diffusivity of immersed passive tracers. Here too, we first consider suspensions of non-interacting swimmers in § 4.1, and then interacting swimmers in § 4.2. Importantly, in a suspension of interacting RTPs, for $U\tau/L \gg 1$, the tracer diffusivity at $O(nL^3)$ is independent of $U\tau/L$, whereas, at $O(nL^3)^2$ it grows linearly in $U\tau/L$. As a result, with increasing nL^3, tracer diffusivities in suspensions of persistent pushers are predicted to become considerably larger than those in puller suspensions. Further, the differing durations of the tracer–single-swimmer (a time of $O(L/U)$) and tracer–swimmer-pair interactions (a time scale of $O(\tau)$) lead to the tracer mean squared displacement (MSD) exhibiting a broad crossover from the ballistic to the diffusive regime for large $U\tau/L$. Finally, in § 5, we present concluding remarks and a course for future work.

2. Scaling arguments for the covariance and tracer diffusivity: comparison with passive sedimenting suspension

In a homogeneous Stokesian suspension of sedimenting particles with a random microstructure, the velocity variance is predicted to diverge linearly with system size (Caflisch & Luke 1985; Hinch 1988; Koch & Shaqfeh 1991; Nicolai *et al.* 1995; Ladd 1996, 1997; Segre, Herbolzheimer & Chaikin 1997; Levine *et al.* 1998; Ramaswamy 2001; Guazzelli & Hinch 2011; Goldfriend, Diamant & Witten 2017). It arises due to the long-ranged $O(1/r)$ disturbance velocity fields of the individual particles acting as point forces (monopoles), as shown in figure 1(*a*). The fluid velocity variance at a given point $\boldsymbol{x}$ may be estimated as $\langle \boldsymbol{u}(\boldsymbol{x}) \cdot \boldsymbol{u}(\boldsymbol{x}) \rangle \equiv \int nL^3 U_s^2 (1/r)^2 \, \mathrm{d}\boldsymbol{r} \sim (nL^3) U_s^2 L_{box}/L$, where we have set the pair-distribution function (that must appear in the volume integral above) to unity, consistent with the above assumption of a random microstructure on scales larger than the particle size; here, U_s is the mean sedimenting speed and L_{box} the system size. The resolution of this system-size-dependent divergence has been a long-standing theoretical challenge (Hinch 1988; Ramaswamy 2001; Guazzelli & Hinch 2011). While theoretical analyses have predicted a finite variance due to the screening of the long-ranged hydrodynamic interactions (Koch & Shaqfeh 1991), in experiments the divergence is cut off on account of container-scale stratification (Luke 2000; Guazzelli & Hinch 2011; Ramaswamy 2001).

https://doi.org/10.1017/jfm.2020.827 Published online by Cambridge University Press

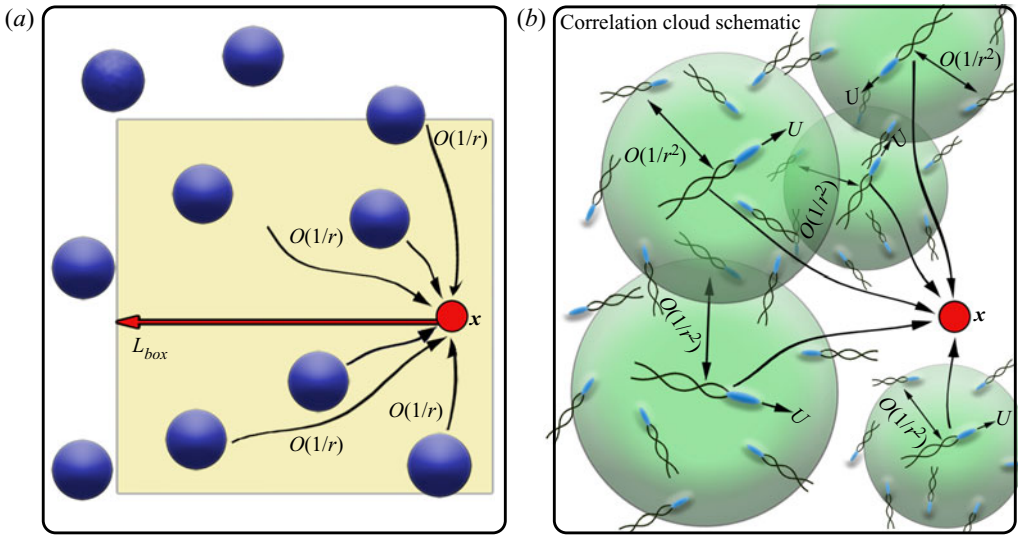


FIGURE 1. (*a*) The $O(1/r)$ contributions due to individual passive spheres contributing to the variance at $\boldsymbol{x}$ in an (infinite) sedimenting suspension. (*b*) An interacting suspension of active straight-swimmers, with each swimmer surrounded by a pair-correlation cloud wherein correlations decay as $O(1/r^2)$. The variance at $\boldsymbol{x}$ is the sum of the contributions of these individual correlation clouds, and is logarithmically divergent.

Unlike passive particles, microswimmers, both pushers and pullers, act as force-dipoles in the far-field, leading to a disturbance velocity field that decays more rapidly with distance as $O(1/r^2)$. An argument along lines similar to that for the passive Stokesian suspension above gives $\langle \boldsymbol{u}(\boldsymbol{x}) \cdot \boldsymbol{u}(\boldsymbol{x}) \rangle \equiv \int nL^3U^2(1/r)^4 \,\mathrm{d}\boldsymbol{r} \sim (nL^3)U^2$, U being the swimming speed, implying that the velocity variance remains finite in the limit $nL^3 \ll 1$ with correlations between swimmers being neglected at leading order. The divergence at small r implied in the scaling integral above is regularized once the finite swimmer size is accounted for. For slender swimmers, in particular, this regularization occurs for $r < O(L)$, when the disturbance velocity field is $O(U/\ln\kappa)$, and the variance is therefore proportional to $nL^3U^2/(\ln\kappa)^2$. Now, the covariance for a suspension of non-interacting swimmers may be similarly written as $\langle \boldsymbol{u}(\boldsymbol{x}) \cdot \boldsymbol{u}(\boldsymbol{x}+\boldsymbol{r}) \rangle \sim (nL^3) \int (U/r'^2) \cdot (U/|\boldsymbol{r} - \boldsymbol{r}'|^2) \,\mathrm{d}\boldsymbol{r}'$. For $r \ll r'$, one obtains the variance estimate above. In the other extreme, corresponding to the pair of points being separated by a distance much greater than the swimmer length, the dominant contribution to the covariance integral arises from swimmers in a volume of $O(r^3)$ around the pair of points considered; thus, r', $|\boldsymbol{r} - \boldsymbol{r}'| \sim O(r)$, and the covariance integrand scales as $O(1/r^4)$. This then leads to the far-field covariance decaying as $O(1/r)$ for $r \gg L$, a result that has already been obtained in the literature, although not for the specific case of slender swimmers (Underhill *et al.* 2008; Underhill & Graham 2011; Zaid, Dunkel & Yeomans 2011).

With the introduction of pair-correlations, the scaling arguments may proceed in terms of 'pair-correlation clouds'. As illustrated in figure 1(*b*), one first adds up the contributions of all swimmers correlated to a given test swimmer; owing to the eventual divergence that results (see below), the volume over which these swimmers range may be regarded as finite in extent to begin with, and is termed a correlation cloud. One then sums up the contributions over all correlation clouds in an infinite domain, while also letting the size of the individual correlation cloud increase to infinity. To estimate the correlated

https://doi.org/10.1017/jfm.2020.827 Published online by Cambridge University Press

contribution to the variance, it suffices to note that the pair-orientation probability density decays as $O(1/r^2)$ in the far-field ($r \gg L$). Each swimmer in a particular pair rotates the other by the disturbance velocity field it generates, and pair-correlations arise due to the cumulative rotation that occurs as the swimmers swim past each other. The force-dipole velocity fields are $O(1/r^2)$, the velocity gradients responsible for rotation are $O(1/r^3)$, and the cumulative rotation that leads to correlations involves integrating the rotation rate over the relative swimming trajectories, and therefore, again scale as $O(1/r^2)$ – these correlations, within individual clouds, are indicated in figure 1(*b*). As already mentioned above, a given swimmer interacts pairwise with a cloud of swimmers surrounding it, and one therefore has the fluid velocity variance due to each correlation cloud scaling as $[\boldsymbol{u}(\boldsymbol{x})\cdot\boldsymbol{u}(\boldsymbol{x})]_{cloud} \equiv nL^3\int U^2 r'^2\,\mathrm{d}r'/(r^4 r'^2) \sim nL^3U^2/r^3$, which when integrated over all such correlation clouds gives $\langle \boldsymbol{u}(\boldsymbol{x})\cdot\boldsymbol{u}(\boldsymbol{x})\rangle|_{corr} \equiv (nL^3)^2U^2\ln(L_{box}/L)$, a logarithmically diverging variance. For persistent RTPs, $L_{box} = U\tau \gg O(L)$, and one obtains $\langle \boldsymbol{u}(\boldsymbol{x})\cdot\boldsymbol{u}(\boldsymbol{x})\rangle|_{corr} \equiv (nL^3)^2U^2\ln(U\tau/L)$. For the specific case of slender swimmers, the contribution due to each correlation cloud scales as $[\boldsymbol{u}(\boldsymbol{x})\cdot\boldsymbol{u}(\boldsymbol{x})]_{cloud} \equiv nL^3/(\ln\kappa)\int (U/\ln\kappa)^2 r'^2\,\mathrm{d}r'/(r^4 r'^2) \sim nL^3U^2/[(\ln\kappa)^3 r^3]$, where an additional $(\ln\kappa)^{-1}$ denotes the logarithmically weak pair-correlations that develop on account of such velocity fields. Integration over all such correlation clouds of slender swimmers gives the correlated component of the variance for a suspension of persistent slender RTPs as $\langle \boldsymbol{u}(\boldsymbol{x})\cdot\boldsymbol{u}(\boldsymbol{x})\rangle|_{corr} \equiv (nL^3)^2/(\ln\kappa)^3U^2\ln(U\tau/L)$. Clearly, the fact that correlations in active suspensions (of straight-swimmers) act to yield a divergent variance is in sharp contrast to the nature of velocity fluctuations in passive sedimenting suspensions described above, and highlights the novel consequences of activity when combined with persistent swimming. Note that, for rapid tumblers (RTPs with $U\tau/L \ll 1$), the pair-correlations decay much more rapidly, resulting in a pair-orientation probability density scaling linearly in $U\tau/L$, and that decays rapidly with r. In this case, the correlated component of the velocity variance may be written as $\langle \boldsymbol{u}(\boldsymbol{x})\cdot\boldsymbol{u}(\boldsymbol{x})\rangle|_{corr} \equiv (nL^3)^2U^2/(\ln\kappa)^3(U\tau/L)$. Thus, for a swimmer suspension, one may write down the total variance by combining both the non-interacting and interacting component scalings given above, to get

$$\langle \boldsymbol{u}(\boldsymbol{x})\cdot\boldsymbol{u}(\boldsymbol{x})\rangle \equiv \frac{nL^3U^2}{(\ln\kappa)^2}\left(\tilde{c}_1 + \tilde{c}_2\frac{nL^3}{\ln\kappa}\frac{U\tau}{L}\right) \tag{2.1}$$

for rapid tumblers ($U\tau/L \ll 1$), and

$$\langle \boldsymbol{u}(\boldsymbol{x})\cdot\boldsymbol{u}(\boldsymbol{x})\rangle \equiv \frac{nL^3U^2}{(\ln\kappa)^2}\left(c_1 + c_2\frac{nL^3}{\ln\kappa}\ln\left(\frac{U\tau}{L}\right)\right) \tag{2.2}$$

for persistent RTPs ($U\tau/L \gg 1$); the constants c_i and $\tilde{c}_i$ ($i = 1, 2$) are determined by the analysis in subsequent sections.

The scalings for the velocity variance may now be used for obtaining corresponding scalings for tracer diffusivities on account of the Green–Kubo relation which gives the diffusivity as an integral of the velocity autocorrelation function; recall that tracer diffusivities have often been used to infer the onset of collective motion in swimmer suspension (Wu & Libchaber 2000; Guazzelli & Hinch 2011; Kasyap *et al.* 2014), and the scalings given here therefore have immediate implications with regard to interpreting the results of such experiments. The tracer diffusivity may be written as $D_t \sim \langle u^2\rangle t_c$. In the absence of correlations, the correlation time t_c is the time scale of the tracer–swimmer interaction. For rapid tumblers, corresponding to $U\tau/L \ll 1$, $t_c \sim \tau$, while for nearly straight-swimmers, $t_c \sim L/U$. Using these estimates, and the expression

https://doi.org/10.1017/jfm.2020.827 Published online by Cambridge University Press

for the non-interacting velocity variance obtained above, for $\langle u^2 \rangle$, one obtains, $D_t|_{uncorr} \sim nL^3U^2\tau/(\ln\kappa)^2$ in the limit $U\tau/L \ll 1$ and $D_t|_{uncorr} \sim nL^3UL/(\ln\kappa)^2$ for $U\tau/L \gg 1$ (Kasyap *et al.* 2014). On the other hand, for correlated swimmers at $O(nL^3)^2$, decorrelation occurs only due to tumbling and hence the correlation time t_c is $O(\tau)$ regardless of the run length ($U\tau/L$). Using the expressions for the correlated variance above, we therefore have $D_t|_{corr} \sim (nL^3)^2U^2\tau/(\ln\kappa)^3U\tau/L$ in the limit $U\tau/L \ll 1$ and $D_t|_{corr} \sim (nL^3)^2UL/(\ln\kappa)^3U\tau/L$ for $U\tau/L \gg 1$. The diffusivity scaling of a passive tracer, to $O(nL^3)^2$, can thus be summarized as

$$D_t \equiv \frac{nL^3U^2\tau}{(\ln\kappa)^2}\left(\widetilde{d}_1 + \frac{nL^3}{\ln\kappa}\frac{U\tau}{L}\widetilde{d}_2\right) \tag{2.3}$$

for rapid tumblers ($U\tau/L \ll 1$), and

$$D_t \equiv \frac{nL^4U}{(\ln\kappa)^2}\left(d_1 + \frac{nL^3}{\ln\kappa}\frac{U\tau}{L}d_2\right) \tag{2.4}$$

for persistent RTPs ($U\tau/L \gg 1$), where the d_i and $\tilde{d}_i$ are again an output of the detailed analysis. From (2.4), we see that, at $O(nL^3)^2$, $D_t \propto U\tau/L$ for $U\tau/L \gg 1$. Thus, while the tracer diffusivity is divergent in the straight-swimmer limit, just like the velocity variance, the divergence is stronger than that of the velocity variance, similar to the case of passive sedimenting suspensions (Guazzelli & Hinch 2011). Thus, for persistent RTPs, correlations play an even greater role in the tracer diffusivity than for the fluid velocity variance, and the difference between the pusher and puller tracer diffusivities is expected to be larger than the correspondence difference between the variances (for a given large value of $U\tau/L$).

3. The fluid velocity covariance

In this section, we eventually derive an analytical expression for the fluid velocity covariance, or the equal-time two-point velocity correlation function, for a suspension of interacting microswimmers. The suspension is assumed to be dilute, that is, the hydrodynamic volume fraction nL^3 is assumed to be of order unity or smaller, and pairwise hydrodynamic interactions between swimmers may therefore be assumed to be dominant. The underlying motivation for this analysis is primarily experiments on bacterial suspensions (Dombrowski *et al.* 2004; Gachelin *et al.* 2014; Patteson *et al.* 2016). Typical bacteria used in these experiments, such as *E. coli* and *B. subtilis*, are quite slender, and we therefore examine a dilute interacting suspension of slender microswimmers, with the swimmer aspect ratio $\kappa \gg 1$.

Although bacteria are the swimmers that we have in mind, the analysis does not aim to model the underlying swimming mechanism in complete detail. As will be seen from the detailed analysis below, the pair interactions between slender swimmers that control the amplitude of the suspension velocity fluctuations, and the resulting tracer diffusivities, are those that occur at separations of $O(L)$. Thus, one seeks an accurate representation of the swimmer disturbance field on these length scales. On much smaller scales, of order the bacterium diameter, the rotation of the helical flagellum (with an associated counter-rotation of the head arising from the torque-free constraint) is responsible for propulsion. From viscous slender-body theory, the axial component of the force density that results from this propulsive motion is $O(\eta U/\ln\kappa)$; here, η is the viscosity of the suspending fluid. Thus, the aforementioned swimmer aspect ratio κ may be regarded as

https://doi.org/10.1017/jfm.2020.827 Published online by Cambridge University Press

the aspect ratio of the flagellum to leading logarithmic order. The rotary fluid motion, that is a direct consequence of this rotation, decays on length scales of order the bacterium (head or flagellum) diameter, and is negligible on the aforementioned length scales of $O(L)$. On scales of $O(L)$, the disturbance velocity field may therefore be regarded as that being induced by the $O(\eta U/\ln\kappa)$ force density above. Implicit in the above arguments for swimming bacteria is the fact that the force density and, thence, the amplitude of the disturbance velocity field scales with swimming speed U; in turn, implying that the two (the fluid velocity disturbance and swimming speed) have a common underlying origin. This may not always be the case, and at least within the spherical squirmer model that is often used to analyse algal swimmers (the so-called Lighthill–Blake swimmer; see Blake (1971, 1973)), the primary dipolar disturbance field and the swimming motion arise as independent degrees of freedom, being related to different modes of the slip velocity on the squirmer surface. The implications of our results, in the context of the spherical squirmer model, are briefly discussed later in § 5.

Bearing in mind the above discussion, we begin by considering a suspension of N slender swimmers, each having a length L (with an aspect ratio $\kappa \gg 1$), and swimming with a speed U directed along its axis. The configuration of the swimmer suspension is characterized by the positions ($\boldsymbol{x}_i$) and orientations ($\boldsymbol{p}_i$) of the N swimmers. As explained above, on length scales of order the swimmer length L, the fluid motion induced by the axial force density of $O(\eta U/\ln\kappa)$ is logarithmically dominant, and the disturbance velocity and pressure fields $\boldsymbol{u}_i$ and P_i, due to the ith swimmer, at leading logarithmic order, satisfy the Stokes equations forced by a line distribution of Stokeslets along the swimmer axis, and the equation of continuity,

$$-\boldsymbol{\nabla} P_i + \eta\nabla^2\boldsymbol{u}_i(\boldsymbol{x}-\boldsymbol{x}_i) = \int_{-L/2}^{L/2} f(s)\boldsymbol{p}_i\boldsymbol{\delta}(\boldsymbol{x}-\boldsymbol{x}_i-s\boldsymbol{p}_i)\,\mathrm{d}s, \tag{3.1a}$$

$$\boldsymbol{\nabla}\cdot\boldsymbol{u}_i = 0. \tag{3.1b}$$

Here, $\boldsymbol{\delta}(z)$ represents the Dirac delta function. Assuming the swimmers to be fore-and-aft symmetric and force free, the linear force density along the swimmer axis (the axial coordinate being s) may be expressed as $f(s) = \eta U\,\mathrm{sgn}(s)/\ln\kappa$, where $\mathrm{sgn}(s) = +(-)1$, for $s > (<)0$. For non-fore-and-aft symmetric swimmers, the linear force density can be represented as $f(s) = \eta U/(\alpha\ln\kappa)\{[\mathrm{sgn}(s-(1/2-\alpha)) - \mathrm{sgn}(s-1/2)] - \alpha/(1-\alpha)[\mathrm{sgn}(s+1/2) - \mathrm{sgn}(s-(1/2-\alpha))]\}$, where $\alpha = L_H/L$ is the ratio of the head length (L_H) to the total bacterium length; $\alpha = 1/2$ represents a fore-and-aft symmetric swimmer. This results in an $O(1)$ change in the force density and thence the disturbance fluid velocity it generates. However, none of the principal conclusions detailed below (and summarized in § 2 above) change on account of swimmer asymmetry. Therefore, in the interests of simplicity, the analysis below is restricted to fore-and-aft symmetric swimmers.

The velocity disturbance satisfying (3.1*a*) may be written in terms of the Oseen–Burgers tensor $\boldsymbol{G}(\boldsymbol{x}) = 1/(8\pi\eta r)[\boldsymbol{I} + \boldsymbol{x}\boldsymbol{x}/r^2]$ (Kim & Karrila 1991) as

$$\boldsymbol{u}_i(\boldsymbol{x}-\boldsymbol{x}_i,t) = \int_{-L/2}^{L/2} f(s)\,\boldsymbol{G}(\boldsymbol{x}-\boldsymbol{x}_i-s\boldsymbol{p}_i)\cdot\boldsymbol{p}_i\,\mathrm{d}s \tag{3.2}$$

and, therefore, the suspension velocity field is expressible as

$$\boldsymbol{u}(\boldsymbol{x},t) \equiv \sum_{i=1}^{N}\boldsymbol{u}_i(\boldsymbol{x}-\boldsymbol{x}_i,t) = \sum_{i=1}^{N}\int_{-L/2}^{L/2} f(s)\,\boldsymbol{G}(\boldsymbol{x}-\boldsymbol{x}_i-s\boldsymbol{p}_i)\cdot\boldsymbol{p}_i\,\mathrm{d}s, \tag{3.3}$$

https://doi.org/10.1017/jfm.2020.827 Published online by Cambridge University Press

where the time dependence comes from the evolving swimmer positions and orientations. Now, the fluid velocity covariance in a swimmer suspension is defined as

$$\langle \boldsymbol{u}(\boldsymbol{x},t)\cdot\boldsymbol{u}(\boldsymbol{x}',t)\rangle = \left\langle \sum_{i=1}^{N}\sum_{j=1}^{N}\int_{-L/2}^{L/2} f(s)\,\mathrm{d}s \int_{-L/2}^{L/2} f(s')\,\mathrm{d}s'\boldsymbol{\delta}(\boldsymbol{x}-\boldsymbol{x}_i)\boldsymbol{\delta}(\boldsymbol{p}-\boldsymbol{p}_i)\boldsymbol{\delta}(\boldsymbol{x}'-\boldsymbol{x}_j) \right.$$
$$\left. \times\,\delta(\boldsymbol{p}'-\boldsymbol{p}_j)[\boldsymbol{G}(\boldsymbol{x}-\boldsymbol{x}_i-s\boldsymbol{p}_i)\cdot\boldsymbol{p}_i]\cdot[\boldsymbol{G}(\boldsymbol{x}'-\boldsymbol{x}_j-s\boldsymbol{p}_j)\cdot\boldsymbol{p}_j] \right\rangle, \quad (3.4)$$

with the angular brackets denoting an ensemble average ($\langle\cdot\rangle$) over the configurations of N swimmers. Since the focus in this section is on the single-time covariance, and one does not expect a dependence on time for a swimmer suspension in a statistically stationary state, we will neglect mention of the time dependence from here on. Within the continuum framework ($N \gg 1$), the above average is expressible in terms of the configurational (position–orientation) probability densities. To see this, one may split the double summation in (3.4) into two distinct contributions; one containing only the diagonal terms, with $i=j$, which involves the singlet probability density defined as $\Omega_1 = \langle\sum_{i=1}^{N}\delta(\boldsymbol{x}_1-\boldsymbol{x}_i)\delta(\boldsymbol{p}_1-\boldsymbol{p}_i)\rangle$, and a second contribution containing the off-diagonal terms $i\neq j$, which may be written in terms of the pair-probability density defined as $\Omega_2 = \langle\sum_{i,j=1;i\neq j}^{N}\boldsymbol{\delta}(\boldsymbol{x}_1-\boldsymbol{x}_i)\boldsymbol{\delta}(\boldsymbol{p}_1-\boldsymbol{p}_i)\boldsymbol{\delta}(\boldsymbol{x}_2-\boldsymbol{x}_j)\boldsymbol{\delta}(\boldsymbol{p}_2-\boldsymbol{p}_j)\rangle$. The expression (3.4) above may be written in terms of these probability densities as

$$\langle \boldsymbol{u}(\boldsymbol{x})\cdot\boldsymbol{u}(\boldsymbol{x}')\rangle = \int_{-L/2}^{L/2} f(s)\,\mathrm{d}s\int_{-L/2}^{L/2} f(s')\,\mathrm{d}s'$$
$$\times\left\{\int \mathrm{d}\boldsymbol{x}_1\,\mathrm{d}\boldsymbol{p}_1[\boldsymbol{G}(\boldsymbol{x}-\boldsymbol{x}_1-s\boldsymbol{p}_1)\cdot\boldsymbol{p}_1]\cdot[\boldsymbol{G}(\boldsymbol{x}'-\boldsymbol{x}_1-s\boldsymbol{p}_1)\cdot\boldsymbol{p}_1]\Omega_1(\boldsymbol{x}_1,\boldsymbol{p}_1)\right.$$
$$+\int \mathrm{d}\boldsymbol{x}_1\,\mathrm{d}\boldsymbol{p}_1\,\mathrm{d}\boldsymbol{x}_2\,\mathrm{d}\boldsymbol{p}_2[\boldsymbol{G}(\boldsymbol{x}-\boldsymbol{x}_1-s\boldsymbol{p}_1)\cdot\boldsymbol{p}_1]\cdot[\boldsymbol{G}(\boldsymbol{x}'-\boldsymbol{x}_2-s\boldsymbol{p}_2)\cdot\boldsymbol{p}_2]$$
$$\left.\times\,\Omega_2(\boldsymbol{x}_1,\boldsymbol{x}_2,\boldsymbol{p}_1,\boldsymbol{p}_2)\right\}. \quad (3.5)$$

Our interest here is to examine a spatially homogeneous isotropic suspension of slender swimmers. In this case, one has $\Omega_1 = nL^3/(4\pi)$, and the pair-probability density Ω_2 above only depends on the relative separation $\boldsymbol{r}=\boldsymbol{x}_2-\boldsymbol{x}_1$ of the pair of swimmers under consideration. It is worth noting that the assumption of a statistically homogeneous and isotropic suspension of swimmers, even in the dilute regime, may only remain valid over a time smaller than $O(nUL^2)^{-1}$. Evidence from simulations of spherical squirmers (Evans *et al.* 2011; Alarcón & Pagonabarraga 2013; Alarcón, Valeriani & Pagonabarraga 2017; Oyama, Molina & Yamamoto 2017) does suggest that hydrodynamic interactions, even in a dilute setting, can induce global orientational order over times that are long compared with the aforementioned scale; this orientational order appears to be driven by near-field interactions between the squirmers, being sensitive to the nature of the surface slip. For slender swimmers interacting at length scales of order their lengths, this assumption is not a limiting one, and the isotropic state appears to be stable to orientation perturbations at leading logarithmic order. We therefore proceed with the above expression for Ω_1.

https://doi.org/10.1017/jfm.2020.827 Published online by Cambridge University Press

It is convenient to solve for the pair-probability density Ω_2, in (3.5), in Fourier space, and hence, Fourier transforming (3.5) yields

$$\langle \hat{\boldsymbol{u}}(\boldsymbol{k}) \cdot \hat{\boldsymbol{u}}(\boldsymbol{k}') \rangle = \frac{\delta(\boldsymbol{k}+\boldsymbol{k}')}{(\ln \kappa)^2} \left\{ \frac{nL^3}{16\pi^7 k^4} \int \mathrm{d}\boldsymbol{p}_1 \left[\left(\boldsymbol{I} - \frac{\boldsymbol{k}\boldsymbol{k}}{k^2} \right) \right] : \boldsymbol{p}_1 \boldsymbol{p}_1 \frac{\sin^4\left(\frac{\pi}{2}\boldsymbol{k}\cdot\boldsymbol{p}_1\right)}{(\boldsymbol{k}\cdot\boldsymbol{p}_1)^2} \right.$$
$$+ \frac{1}{4\pi^6 k^4} \int \mathrm{d}\boldsymbol{p}_1 \, \mathrm{d}\boldsymbol{p}_2 \left[\left(\boldsymbol{I} - \frac{\boldsymbol{k}\boldsymbol{k}}{k^2} \right) \right] : \boldsymbol{p}_1 \boldsymbol{p}_2$$
$$\left. \times \frac{\sin^2\left(\frac{\pi}{2}\boldsymbol{k}\cdot\boldsymbol{p}_1\right)}{\boldsymbol{k}\cdot\boldsymbol{p}_1} \frac{\sin^2\left(\frac{\pi}{2}\boldsymbol{k}\cdot\boldsymbol{p}_2\right)}{\boldsymbol{k}\cdot\boldsymbol{p}_2} \hat{\Omega}_2(\boldsymbol{p}_1, \boldsymbol{p}_2; \boldsymbol{k}) \right\}. \tag{3.6}$$

Here, the Fourier-transformed quantities are defined as $\hat{f}(\boldsymbol{k}) = \int \exp(-2\pi \mathrm{i}\boldsymbol{k}\cdot\boldsymbol{x}) f(\boldsymbol{x}) \, \mathrm{d}\boldsymbol{x}$, and the factor $\delta(\boldsymbol{k}+\boldsymbol{k}')$ represents the translational invariance due to the assumed spatial homogeneity. Note that (3.6) has been rendered non-dimensional by using L and U, respectively, as length and velocity scales.

The key quantity to be determined, in order to calculate the covariance above, is the Fourier-transformed pair-probability density $\hat{\Omega}_2(\boldsymbol{p}_1, \boldsymbol{p}_2; \boldsymbol{k})$ in (3.6). In what follows, we first characterize the variance and covariance for the simpler case of a suspension of non-interacting swimmers in § 3.1, in which case the term involving $\hat{\Omega}_2$ may be neglected. We then analyse suspensions of interacting straight-swimmers and RTPs, respectively, in §§ 3.2 and 3.3, since the expression for $\hat{\Omega}_2(\boldsymbol{p}_1, \boldsymbol{p}_2; \boldsymbol{k})$ differs in the two cases.

3.1. *Suspensions of non-interacting swimmers*

In the absence of interactions, only the term involving the single swimmer probability density is relevant, so that (3.6) takes the simplified form

$$\langle \hat{\boldsymbol{u}}(\boldsymbol{k}) \cdot \hat{\boldsymbol{u}}(\boldsymbol{k}') \rangle|_{uncorr} = \frac{nL^3}{16\pi^7 (\ln \kappa)^2 k^4} \delta(\boldsymbol{k}+\boldsymbol{k}') \int \mathrm{d}\boldsymbol{p}_1 \left[1 - \frac{(\boldsymbol{k}\cdot\boldsymbol{p}_1)^2}{k^2} \right] \frac{\sin^4\left(\frac{\pi \boldsymbol{k}\cdot\boldsymbol{p}_1}{2}\right)}{(\boldsymbol{k}\cdot\boldsymbol{p}_1)^2}. \tag{3.7}$$

An inverse Fourier transform of (3.7) yields

$$\langle \boldsymbol{u}(\boldsymbol{x}) \cdot \boldsymbol{u}(\boldsymbol{x}+\boldsymbol{r}) \rangle|_{uncorr} = \frac{nL^3}{4\pi^6 (\ln \kappa)^2 r} \int_0^\infty \mathrm{d}k \frac{\sin(2\pi k r)}{k^5} \int_{-1}^1 \mathrm{d}\mu \left(\frac{1-\mu^2}{\mu^2} \right) \sin^4\left(\frac{\pi k \mu}{2} \right). \tag{3.8}$$

Owing to isotropy, the covariance only depends on the scalar distance r. The variance is obtained on setting $r = 0$ in (3.8), which gives $\langle \boldsymbol{u}(\boldsymbol{x}) \cdot \boldsymbol{u}(\boldsymbol{x}) \rangle|_{uncorr} = nL^3/[96\pi(\ln \kappa)^2]$. One can simplify (3.8) in the far-field ($r \gg 1$) by adopting $\tilde{k} = kr$ as the new variable (in the outer integral) instead of k, and approximating $\sin[\pi \tilde{k}\mu/(2r)] \approx \pi \tilde{k}\mu/(2r)$ (that is, seeking a limiting form of the expression for $\tilde{k} \sim O(1)$, but $r \gg 1$). This yields the far-field limiting form of the covariance which, expectedly, is similar to that obtained earlier for point dipoles (Underhill & Graham 2011; Zaid *et al.* 2011), and is given by $\langle \boldsymbol{u}(\boldsymbol{x}) \cdot \boldsymbol{u}(\boldsymbol{x}+\boldsymbol{r}) \rangle|_{uncorr} = nL^3/[480\pi(\ln \kappa)^2 r]$. Recognizing that the (non-dimensional) dipole strength

https://doi.org/10.1017/jfm.2020.827 Published online by Cambridge University Press

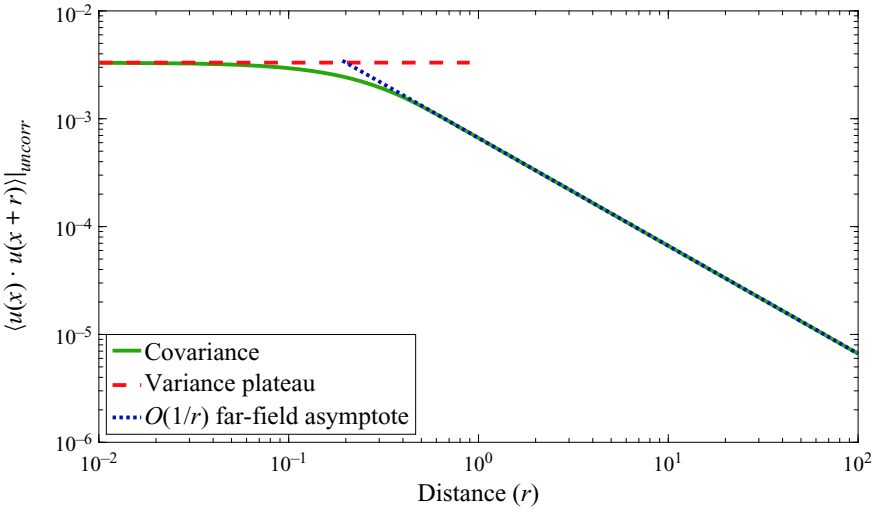


FIGURE 2. The $O(nL^3)$ velocity covariance in a dilute non-interacting suspension of slender swimmers. The covariance transitions from an $O(nL^3)/(\ln\kappa)^2$ variance plateau to a far-field $O(1/r)$ asymptote. The swimmer aspect ratio is chosen to be $\kappa = 8$.

for slender swimmers is $D = 1/(4\ln\kappa)$, one in fact recovers the exact covariance for point force-dipoles, $\langle \boldsymbol{u}(\boldsymbol{x}) \cdot \boldsymbol{u}(\boldsymbol{x}+\boldsymbol{r})\rangle|_{uncorr} = nL^3D^2/[30\pi r]$. The aforementioned variance and far-field covariance have been plotted alongside (3.8), evaluated numerically, in figure 2. Note that the covariance, as given by (3.8), depends only on the single-swimmer statistics at a given instant, and therefore, remains the same both for straight-swimmers and run-and-tumble swimmers provided the tumbles in the latter case are assumed to be instantaneous (so that any disturbance field generated during a tumble is neglected).

3.2. *Suspensions of interacting straight-swimmers*

Herein, we consider the covariance in a suspension of hydrodynamically interacting slender straight-swimmers to $O(nL^3)^2$. The contribution at this order involves the correlations that develop due to pairwise interactions between slender straight-swimmers, and these are characterized by the Fourier-transformed pair-probability density $\hat{\Omega}_2(\boldsymbol{p}_1, \boldsymbol{p}_2; \boldsymbol{k})$ in (3.6). The correlated component of the Fourier transformed velocity variance is given by

$$\langle \hat{\boldsymbol{u}}(\boldsymbol{k}) \cdot \hat{\boldsymbol{u}}(\boldsymbol{k}')\rangle|_{corr} = \frac{\delta(\boldsymbol{k}+\boldsymbol{k}')}{4\pi^6(\ln\kappa)^2k^4}\left[\int \mathrm{d}\boldsymbol{p}_1\,\mathrm{d}\boldsymbol{p}_2\left[\left(\boldsymbol{I}-\frac{\boldsymbol{k}\boldsymbol{k}}{k^2}\right)\right] : \boldsymbol{p}_1\boldsymbol{p}_2\frac{\sin^2\left(\frac{\pi}{2}\boldsymbol{k}\cdot\boldsymbol{p}_1\right)}{\boldsymbol{k}\cdot\boldsymbol{p}_1}\right.$$
$$\left.\times\frac{\sin^2\left(\frac{\pi}{2}\boldsymbol{k}\cdot\boldsymbol{p}_2\right)}{\boldsymbol{k}\cdot\boldsymbol{p}_2}\,\hat{\Omega}_2(\boldsymbol{p}_1,\boldsymbol{p}_2;\boldsymbol{k})\right], \tag{3.9}$$

where $\hat{\Omega}_2$ is to be determined.

As already discussed in § 2, the disturbance field of a slender swimmer is only $O(\ln\kappa)^{-1}$ on length scales of $O(L)$, and this leads to logarithmically weak interactions between

https://doi.org/10.1017/jfm.2020.827 Published online by Cambridge University Press

swimmers on scales of order the swimmer length. The slender swimmer assumption (Berg 2004; Gachelin *et al.* 2014) has, in fact, reasonably reproduced experimentally measured disturbance velocity fields to distances of $O(L)$ (Kasyap *et al.* 2014). This allows one to expand Ω_2 as a series in $(\ln\kappa)^{-1}$ about the base uncorrelated state. One writes $\Omega_2 = \Omega_2^{(0)} + 1/(\ln\kappa)\Omega_2^{(1)} + \ldots$, where $\Omega_2^{(0)}$ is the product of two singlet probability densities, $(nL^3)^2/(4\pi)^2$, and denotes the uncorrelated base state at leading order; $\Omega_2^{(1)} \equiv \Omega_2^{(1)}(\boldsymbol{r}, \boldsymbol{p}_1, \boldsymbol{p}_2)$ gives the correlated probability, at $O(\ln\kappa)^{-1}$, of finding two swimmers with orientations $\boldsymbol{p}_1$ and $\boldsymbol{p}_2$, separated by $\boldsymbol{r}$. Note that the contribution due to $\Omega_2^{(0)}$ in (3.9) is identically zero. This is as expected since the velocity variance in an uncorrelated swimmer suspension must be proportional to nL^3, with no constraints of diluteness involved.

Therefore, to leading logarithmic order, one only needs to determine $\hat{\Omega}_2^{(1)}(\boldsymbol{p}_1, \boldsymbol{p}_2; \boldsymbol{k})$, the Fourier transform of the $O(\ln\kappa)^{-1}$ pair-probability density above, in order to characterize pair-correlations in the swimmer suspension and, thence, determine the correlated contribution to the covariance in (3.9). The leading-order contribution being zero, (3.9) is now expressible as

$$\langle \hat{\boldsymbol{u}}(\boldsymbol{k}) \cdot \hat{\boldsymbol{u}}(\boldsymbol{k}') \rangle|_{corr} = \frac{\delta(\boldsymbol{k}+\boldsymbol{k}')}{4\pi^6(\ln\kappa)^3 k^4} \left[\int \mathrm{d}\boldsymbol{p}_1\, \mathrm{d}\boldsymbol{p}_2 \frac{1}{\boldsymbol{k}\cdot\boldsymbol{p}_1} \frac{1}{\boldsymbol{k}\cdot\boldsymbol{p}_2} \sin^2\left(\frac{\pi}{2}\boldsymbol{k}\cdot\boldsymbol{p}_1\right) \sin^2\left(\frac{\pi}{2}\boldsymbol{k}\cdot\boldsymbol{p}_2\right) \times \left(\boldsymbol{I} - \frac{\boldsymbol{k}\boldsymbol{k}}{k^2}\right) : \boldsymbol{p}_1\boldsymbol{p}_2 \hat{\Omega}_2^{(1)}(\boldsymbol{p}_1, \boldsymbol{p}_2; \boldsymbol{k}) \right]. \tag{3.10}$$

Now, in a macroscopic suspension of N ($\gg 1$) interacting slender straight-swimmers, Ω_N satisfies the Liouville equation, that evolves due to swimming, and due to convection and rotation of each swimmer by the disturbance velocity fields due to the remaining swimmers. In the dilute limit, integrating over the degrees of freedom of the remaining $N-2$ swimmers, while neglecting three-swimmer interactions, one obtains the equation for the pair-probability density Ω_2, at steady-state, as

$$\nabla_{\boldsymbol{r}} \cdot \{[(U\boldsymbol{p}_2 + \bar{\boldsymbol{u}}_{21}) - (U\boldsymbol{p}_1 + \bar{\boldsymbol{u}}_{12})]\Omega_2\} + \nabla_{\boldsymbol{p}_1} \cdot (\dot{\boldsymbol{p}}_{12}\Omega_2) + \nabla_{\boldsymbol{p}_2} \cdot (\dot{\boldsymbol{p}}_{21}\Omega_2) = 0. \tag{3.11}$$

The terms within braces in (3.11) denote the convection of Ω_2 by the relative velocity of the swimmer pair that includes contributions due to swimming ($U\boldsymbol{p}_i$) and due to the disturbance velocity fields $\bar{\boldsymbol{u}}_{ij}$ (of swimmer j at the location of swimmer i); the overbar here denotes an average over the length of swimmer i, a result derivable from viscous slender-body theory (Batchelor 1970). These disturbance fields are $O(\ln\kappa)^{-1}$ since we are considering separations of $O(L)$ and larger, and are thus asymptotically small compared with the swimming-induced convection. The third and fourth terms denote rotation of the swimmer orientations due to the disturbance velocity fields, with $\dot{\boldsymbol{p}}_{ij}$ again denoting the rotation of swimmer i by the disturbance velocity field due to swimmer j; the expression for the $\dot{\boldsymbol{p}}_{ij}$, in Fourier space, are given in appendix A.

Using the aforementioned series expansion of Ω_2 and neglecting the convection by the $O(\ln\kappa)^{-1}$ disturbance velocity fields in (3.11), at leading logarithmic order, pair-correlations develop along straight-swimming trajectories. Thus, at $O(\ln\kappa)^{-1}$, for hydrodynamically interacting slender swimmers, $\Omega_2^{(1)}$ satisfies

$$(\boldsymbol{p}_2 - \boldsymbol{p}_1) \cdot \nabla_{\boldsymbol{r}} \Omega_2^{(1)} = -\frac{(nL^3)^2}{(4\pi)^2} \left[\nabla_{\boldsymbol{p}_1} \cdot \dot{\boldsymbol{p}}_{12} + \nabla_{\boldsymbol{p}_2} \cdot \dot{\boldsymbol{p}}_{21} \right], \tag{3.12}$$

https://doi.org/10.1017/jfm.2020.827 Published online by Cambridge University Press

in non-dimensional terms. Fourier transforming (3.12) leads to

$$2\pi \mathrm{i}\boldsymbol{k}\cdot(\boldsymbol{p}_2-\boldsymbol{p}_1)\hat{\Omega}_2^{(1)} = -\frac{(nL^3)^2}{(4\pi)^2}\left[\boldsymbol{\nabla}_{p_1}\cdot\hat{\boldsymbol{p}}_{12}+\boldsymbol{\nabla}_{p_2}\cdot\hat{\boldsymbol{p}}_{21}\right], \tag{3.13}$$

where the convection in physical space reduces to a multiplicative $\boldsymbol{k}$ factor in Fourier space. The general solution of (3.13) may be written as

$$\hat{\Omega}_2^{(1)} = C\delta\left[\boldsymbol{k}\cdot(\boldsymbol{p}_2-\boldsymbol{p}_1)\right] - \frac{(nL^3)^2}{(4\pi)^2 2\pi\mathrm{i}\boldsymbol{k}\cdot(\boldsymbol{p}_2-\boldsymbol{p}_1)}\left[\boldsymbol{\nabla}_{p_1}\cdot\hat{\boldsymbol{p}}_{12}+\boldsymbol{\nabla}_{p_2}\cdot\hat{\boldsymbol{p}}_{21}\right], \tag{3.14}$$

where the first term on the right-hand side, involving the Dirac delta function, is the homogeneous solution (using the identity $z\delta(z)=0$; see Gelfand & Shilov (1964)), and the expressions for $\hat{\boldsymbol{p}}_{12}$ and $\hat{\boldsymbol{p}}_{21}$ that appear in the second term, the particular solution, are given in appendix A. The constant C is determined from the fact that the swimmers are uncorrelated prior to interaction; that is, $\Omega_2^{(1)}\to 0$ for swimmers when they are infinitely separated in the upstream direction. Choosing a Cartesian coordinate system with the z axis along the relative swimming velocity vector, that is $\hat{\boldsymbol{z}} = (\boldsymbol{p}_2-\boldsymbol{p}_1)/|\boldsymbol{p}_2-\boldsymbol{p}_1|$, implies that $z\to-\infty$ denotes the aforementioned upstream infinity. Therefore, the constraint of uncorrelated swimmers infinitely far upstream may be given as

$$\lim_{z\to-\infty}\Omega_2^{(1)} \equiv \lim_{z\to-\infty}\int \mathrm{d}\boldsymbol{k}\exp\left[2\pi\mathrm{i}\boldsymbol{k}\cdot\boldsymbol{x}\right]\hat{\Omega}_2^{(1)} = 0. \tag{3.15}$$

One can represent $\boldsymbol{x} = (\boldsymbol{x}^\perp, z) \equiv (\boldsymbol{x}\cdot[\boldsymbol{I}-\hat{\boldsymbol{z}}\hat{\boldsymbol{z}}], z)$, and since (3.15) is valid for arbitrary $\boldsymbol{k}^\perp$, one need only consider the integral over k_z, whence one obtains

$$\lim_{z\to-\infty}\int \mathrm{d}k_z\exp\left[2\pi\mathrm{i}k_z z\right] \times\left[C\delta[k_z|\boldsymbol{p}_2-\boldsymbol{p}_1|] - \frac{(nL^3)^2}{(4\pi)^2 2\pi\mathrm{i}k_z|\boldsymbol{p}_2-\boldsymbol{p}_1|}\left[\boldsymbol{\nabla}_{p_1}\cdot\hat{\boldsymbol{p}}_{12}+\boldsymbol{\nabla}_{p_2}\cdot\hat{\boldsymbol{p}}_{21}\right]\right] = 0. \tag{3.16}$$

While the first term within brackets in (3.16) may be evaluated readily, for $z\to-\infty$, the dominant contribution to the second term arises when $k_z\to 0$ such that $k_z z$ remains finite. This results in the following expression for C:

$$C = -\frac{(nL^3)^2}{32\pi^2}\lim_{k_z\to 0}\left[\boldsymbol{\nabla}_{p_1}\cdot\hat{\boldsymbol{p}}_{12}+\boldsymbol{\nabla}_{p_2}\cdot\hat{\boldsymbol{p}}_{21}\right]. \tag{3.17}$$

We now choose $\boldsymbol{x}^\perp = (x, y)$ such that $\hat{\boldsymbol{x}} = (\boldsymbol{p}_2\wedge\boldsymbol{p}_1)/|\boldsymbol{p}_2\wedge\boldsymbol{p}_1|$ and $\hat{\boldsymbol{y}} = (\boldsymbol{p}_2+\boldsymbol{p}_1)/|\boldsymbol{p}_2+\boldsymbol{p}_1|$, are the unit vectors in the plane orthogonal to $\hat{\boldsymbol{z}}$. For $k_z\to 0$, we have, $\boldsymbol{k}\cdot\boldsymbol{p}_1 = \boldsymbol{k}\cdot\boldsymbol{p}_2$ with each of them being given by $k_y|\boldsymbol{p}_2+\boldsymbol{p}_1|/2$. Using these relations in (3.17), and after some algebra, C is given by

$$C = \frac{3(nL^3)^2}{8\pi^5}\left[\frac{|\boldsymbol{p}_2-\boldsymbol{p}_1|^2}{[\boldsymbol{k}\wedge(\boldsymbol{p}_2-\boldsymbol{p}_1)]\cdot[\boldsymbol{k}\wedge(\boldsymbol{p}_2-\boldsymbol{p}_1)]}\right]\frac{1}{\left(\boldsymbol{k}\cdot(\boldsymbol{p}_1+\boldsymbol{p}_2)\right)}\sin^2\left(\frac{\pi}{4}\boldsymbol{k}\cdot(\boldsymbol{p}_1+\boldsymbol{p}_2)\right) \times\sin\left(\frac{\pi}{2}\boldsymbol{k}\cdot(\boldsymbol{p}_1+\boldsymbol{p}_2)\right)\left[\boldsymbol{p}_2\cdot\boldsymbol{p}_1 - \frac{\left(\boldsymbol{k}\cdot(\boldsymbol{p}_1+\boldsymbol{p}_2)\right)^2|\boldsymbol{p}_2-\boldsymbol{p}_1|^2}{4\left(\boldsymbol{k}\wedge(\boldsymbol{p}_2-\boldsymbol{p}_1)\right)\cdot\left(\boldsymbol{k}\wedge(\boldsymbol{p}_2-\boldsymbol{p}_1)\right)}\right]. \tag{3.18}$$

https://doi.org/10.1017/jfm.2020.827 Published online by Cambridge University Press

Using (3.18) in (3.14), the Fourier-transformed pair-probability density at, $O(\ln\kappa)^{-1}$, may be expressed as

$$\begin{aligned}\hat{\Omega}_2^{(1)} = {} & \frac{3(nL^3)^2}{8\pi^5}\left[\frac{|\boldsymbol{p}_2-\boldsymbol{p}_1|^2}{(\boldsymbol{k}\wedge(\boldsymbol{p}_2-\boldsymbol{p}_1))\cdot(\boldsymbol{k}\wedge(\boldsymbol{p}_2-\boldsymbol{p}_1))}\right]\frac{1}{(\boldsymbol{k}\cdot(\boldsymbol{p}_1+\boldsymbol{p}_2))}\sin^2\left(\frac{\pi}{4}\boldsymbol{k}\cdot(\boldsymbol{p}_1+\boldsymbol{p}_2)\right)\\ & \times\sin\left(\frac{\pi}{2}\boldsymbol{k}\cdot(\boldsymbol{p}_1+\boldsymbol{p}_2)\right)\left[\boldsymbol{p}_2\cdot\boldsymbol{p}_1-\frac{(\boldsymbol{k}\cdot(\boldsymbol{p}_1+\boldsymbol{p}_2))^2|\boldsymbol{p}_2-\boldsymbol{p}_1|^2}{4(\boldsymbol{k}\wedge(\boldsymbol{p}_2-\boldsymbol{p}_1))\cdot(\boldsymbol{k}\wedge(\boldsymbol{p}_2-\boldsymbol{p}_1))}\right]\delta\left[\boldsymbol{k}\cdot(\boldsymbol{p}_2-\boldsymbol{p}_1)\right]\\ & -\frac{3\mathrm{i}(nL^3)^2}{32\pi^6k^3}PV\left[\frac{1}{\hat{\boldsymbol{k}}\cdot(\boldsymbol{p}_2-\boldsymbol{p}_1)}\right]\left(\boldsymbol{I}-\hat{\boldsymbol{k}}\hat{\boldsymbol{k}}\right):\boldsymbol{p}_1\boldsymbol{p}_2\left[\frac{1}{(\boldsymbol{k}\cdot\boldsymbol{p}_1)}\sin^2\left(\frac{\pi}{2}\boldsymbol{k}\cdot\boldsymbol{p}_1\right)\sin\left(\pi\boldsymbol{k}\cdot\boldsymbol{p}_2\right)\right.\\ & \left.+\frac{1}{(\boldsymbol{k}\cdot\boldsymbol{p}_2)}\sin^2\left(\frac{\pi}{2}\boldsymbol{k}\cdot\boldsymbol{p}_2\right)\sin\left(\pi\boldsymbol{k}\cdot\boldsymbol{p}_1\right)\right],\end{aligned}\tag{3.19}$$

where both terms in (3.19) are generalized functions. Thus, the integral involving the argument of $PV[\cdot]$ needs to be interpreted in the sense of a Cauchy principal value. The analysis of the homogeneous solution above is crucial, since it is this term alone that contributes to the covariance.

One can now use (3.19) in (3.10), and express the Fourier transformed correlated covariance in a $\boldsymbol{k}$-aligned polar coordinate system. Denoting the polar angles of the two swimmers as θ_1 and θ_2, and their relative azimuthal angle as ϕ, one has $\boldsymbol{p}_1=\cos\theta_1\hat{\boldsymbol{k}}+\sin\theta_1\cos\phi\hat{\boldsymbol{k}}_\perp+\sin\theta_1\sin\phi\hat{\boldsymbol{k}}'_\perp$ and $\boldsymbol{p}_2=\cos\theta_2\hat{\boldsymbol{k}}+\sin\theta_2\hat{\boldsymbol{k}}_\perp$. The correlated component of the covariance in Fourier space may then be written as

$$\begin{aligned}&\langle\hat{\boldsymbol{u}}(\boldsymbol{k})\cdot\hat{\boldsymbol{u}}(\boldsymbol{k}')\rangle|_{corr}\\ &=\frac{3(nL^3)^2\delta(\boldsymbol{k}+\boldsymbol{k}')}{256\pi^6(\ln\kappa)^3k^7}\left[\int_{-1}^{1}\mathrm{d}\mu_2(1-\mu_2^2)^2\sin(\pi k\mu_2)\sin^3\left(\frac{\pi}{2}k\mu_2\right)\left(j_0\left(\frac{\pi}{2}k\mu_2\right)\right)^3\right.\\ &\quad+\mathrm{i}\int_{-1}^{1}\mathrm{d}\mu_1\int_{-1}^{1}\mathrm{d}\mu_2\frac{(1-\mu_1^2)^2(1-\mu_2^2)^2}{\mu_2-\mu_1}j_0\left(\frac{\pi}{2}k\mu_1\right)j_0\left(\frac{\pi}{2}k\mu_2\right)\sin^2\left(\frac{\pi}{2}k\mu_1\right)\\ &\quad\left.\times\sin^2\left(\frac{\pi}{2}k\mu_2\right)\left\{j_0\left(\frac{\pi}{2}k\mu_1\right)\cos\left(\frac{\pi}{2}k\mu_2\right)+j_0\left(\frac{\pi}{2}k\mu_2\right)\cos\left(\frac{\pi}{2}k\mu_1\right)\right\}\right],\end{aligned}\tag{3.20}$$

where $\mu_i\equiv\cos\theta_i$ and $j_0(z)=\sin z/z$ is the spherical Bessel function of the first kind (Gradshteyn & Ryzhik 1980). Here, we have performed the simpler ϕ integration for both the homogeneous and the particular solutions, and the delta function in the homogeneous solution of $\hat{\Omega}_2^{(1)}$ has enabled us to evaluate the μ_1 integral (the first term on the right-hand side of (3.20)). The contribution from the particular solution of $\hat{\Omega}_2^{(1)}$, represented by the second term on the right-hand side of (3.20) vanishes upon integration. To see this, one may transform from (μ_1,μ_2) to (μ_+,μ_-), where $\mu_+=\mu_1+\mu_2$ and $\mu_-=\mu_2-\mu_1$. In terms of the new integration variables, the particular solution integrand is odd in μ_- and therefore vanishes on applying the integration limits, implying that the $O(nL^3)^2$ contribution to the covariance comes only from the homogeneous solution as stated above. On inverse Fourier transforming (3.20), one obtains the $O(nL^3)^2$ component of

https://doi.org/10.1017/jfm.2020.827 Published online by Cambridge University Press

the covariance in physical space, which is expressible as

$$\langle \boldsymbol{u}(\boldsymbol{x}) \cdot \boldsymbol{u}(\boldsymbol{x}+\boldsymbol{r})\rangle|_{corr} = \frac{3(nL^3)^2}{128\pi^6(\ln\kappa)^3 r}\int_0^\infty \mathrm{d}k \frac{\sin(2\pi kr)}{k^6}\int_{-1}^{1}\mathrm{d}\mu(1-\mu^2)^2\sin(\pi k\mu) \times \sin^3\left(\frac{\pi}{2}k\mu\right)\left(j_0\left(\frac{\pi}{2}k\mu_2\right)\right)^3. \tag{3.21}$$

Again, the variance is obtained by setting $r = 0$ in (3.21), which gives

$$\langle \boldsymbol{u}(\boldsymbol{x}) \cdot \boldsymbol{u}(\boldsymbol{x})\rangle|_{corr} = \frac{3(nL^3)^2}{64\pi^5(\ln\kappa)^3}\int_0^\infty \mathrm{d}k \frac{1}{k^5}\int_{-1}^{1}\mathrm{d}\mu(1-\mu^2)^2\sin(\pi k\mu)\frac{1}{\left(\frac{\pi}{2}k\mu\right)^3}\sin^6\left(\frac{\pi}{2}k\mu\right). \tag{3.22}$$

The integrand for k in (3.22) scales as $1/k$ as $k \to 0$, implying that the integral itself is logarithmically divergent. Thus, the $O(nL^3)^2$ contribution to the covariance is not well defined for any r and, in particular, results in a logarithmically divergent variance on setting $r = 0$, in agreement with the scaling arguments in § 2. The physical arguments for this logarithmic divergence may now be laid out in a little more of an equation-specific manner than in § 2. As mentioned therein, the divergence arises from the slow $O(1/r^2)$ decay of the pair-probability density in the far-field. One may observe this from the physical space form of $\Omega_2^{(1)}$, given by (3.12), wherein integrating along the trajectory of relative swimming, that is $\Omega_2^{(1)} = -(nL^3)^2/[(4\pi)^2|\boldsymbol{p}_2 - \boldsymbol{p}_1|]\int_{-\infty}^{z}\mathrm{d}z'(\boldsymbol{\nabla}_{\boldsymbol{p}_1}\cdot\dot{\boldsymbol{p}}_{12} + \boldsymbol{\nabla}_{\boldsymbol{p}_2}\cdot\dot{\boldsymbol{p}}_{21})$, with $\dot{\boldsymbol{p}}_{ij} \sim O(1/r^3)$, the velocity gradient scaling in the far-field, leads to the $O(1/r^2)$ decay. This can be readily inferred from (3.19) as well, where power counting in k, as $k \to 0$ suggests that $\hat{\Omega}_2^{(1)} \sim O(1/k)$ (which in real space would imply $\Omega_2^{(1)} \sim O(1/r^2)$ in the far-field); here, we have used the scaling $\delta(k) \sim O(1/k)$ to arrive at the aforementioned argument. In this scenario, where a given swimmer interacts pairwise with a cloud of swimmers surrounding it (see figure 1*b*), one has the fluid velocity variance due to a 'correlated cloud', of radius r, scaling as $[\boldsymbol{u}(\boldsymbol{x})\cdot\boldsymbol{u}(\boldsymbol{x})]_{cloud} \equiv nL^3\int U^2 r'^2\,\mathrm{d}r'/(r^4 r'^2) \sim nL^3U^2/r^3$, which when integrated over all such correlation clouds in position space, gives $\langle \boldsymbol{u}(\boldsymbol{x})\cdot\boldsymbol{u}(\boldsymbol{x})\rangle|_{corr} \equiv (nL^3)^2\ln(L_{box}/L)$, a logarithmically divergent variance.

In practice, the logarithmic divergence above will be cut off at an appropriate screening length L_{screen}, such that the total variance, including the uncorrelated contribution given by (3.8), and the correlated one given above, takes the form $c_1(nL^3) + (nL^3)^2\{c_2\ln[L_{screen}/L] + c_3\}$, with the constants c_i being functions of swimmer aspect ratio. The screening length depends on the particular physical scenario. In box-size-limited simulations, the largest admissible wavelength is set by the computational domain, so $L_{screen} = k_{min}^{-1} \equiv L_{box}$. In figure 3, we highlight this box-size-dependent divergence of the correlated contribution as a function of k_{min}, with k_{min} replacing 0 as the lower limit of the Fourier integral in (3.22) and, thereby, enforcing a long wavelength cutoff. For suspensions of interacting straight-swimmers, the box-size limitation arises provided the swimmer mean free path, which is $O(nL^2)^{-1}$, is larger than L_{box}. Note that, for $L_{box} \gg (nL^2)^{-1}$, such suspensions are always unstable to sufficiently long wavelength orientation and velocity perturbations regardless of the swimmer volume fraction (Saintillan & Shelley 2008; Subramanian & Koch 2009); this may be seen from the threshold criterion for instability (collective motion) given in the introduction, but with τ being set to infinity for straight-swimmers. One expects a transition to collective motion to be accompanied by a sharp box-size-dependent increase in the fluid velocity variance and tracer diffusivities

https://doi.org/10.1017/jfm.2020.827 Published online by Cambridge University Press

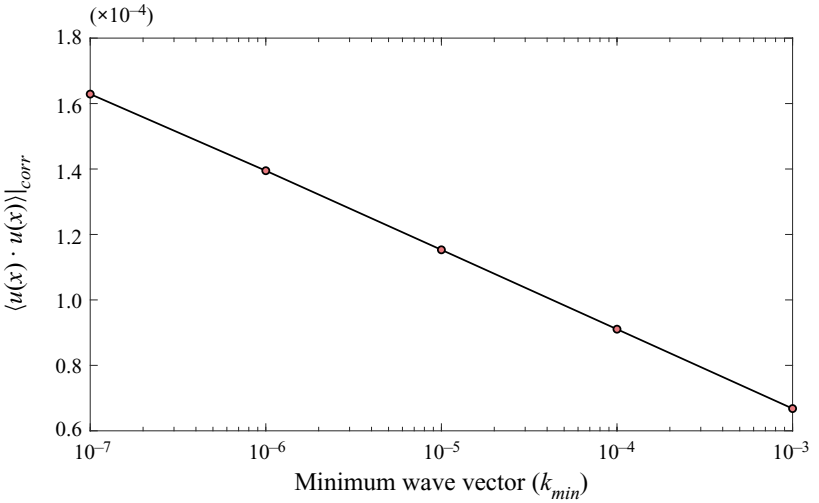


FIGURE 3. The $O(nL^3)^2$ correlated straight-swimmer variance plotted against the infrared cutoff (k_{min}) used to evaluate (3.22). As expected, it exhibits a logarithmic divergence with decreasing k_{min}. The swimmer aspect ratio is chosen to be $\kappa = 8$.

(Saintillan & Shelley 2011; Krishnamurthy & Subramanian 2015; Stenhammar *et al.* 2017). The longest wavelength orientation (and velocity) modes that control the onset of collective motion and, thence, the amplitude of the velocity variance, have a nematic symmetry. The assumption of a homogeneous isotropic state in the analysis above therefore concerns the long-ranged correlations that develop either prior to the onset of collective motion (implying box sizes $L_{box} \sim O(nL^2)^{-1}$), or on length scales smaller than those corresponding to the aforementioned long wavelength (nematic) modes after onset. Simulations of interacting regularized force dipole swimmers carried out by Underhill & Graham (2011), at $nL^3 \sim 10^{-2}$ (and in the regime $L_{box} < (nL^2)^{-1}$), do point to a logarithmic divergence of the variance, as may be inferred from the $O(1/r^2)$ far-field decay of the spatial orientation correlations and, thence, the pair-probability density (see figure 7, Underhill & Graham (2011)). Interestingly, the authors observe a logarithmically diverging variance in simulations, even at higher volume fractions ($nL^3 \sim 10^{-1}$), for a range of box sizes $L_{box} \geqslant (nL^2)^{-1}$. For slender swimmers, owing to the weak pair-correlations (at least by a factor of $\ln \kappa$), the orientation decorrelation is expected to occur over a logarithmically large number of pair interactions, implying a larger effective mean free path. Thus, our analysis may remain valid for suspension of slender swimmers at even higher volume fractions than for the regularized point dipoles considered in earlier simulations (Underhill *et al.* 2008; Underhill & Graham 2011; Stenhammar *et al.* 2017; Bárdfalvy *et al.* 2019).

For real bacteria, intrinsic decorrelation mechanisms such as rotary diffusion and/or run-and-tumble dynamics, lead to $L_{screen} = U/D_r$ or $U\tau$, where D_r is the rotary diffusivity and τ the mean run duration. Recall that in § 2, we presented scaling arguments for the latter case. It is worth pointing out here that the rotary diffusion above could have an entirely hydrodynamic origin. For slender straight-swimmer suspensions not limited by box size, one expects the logarithmic divergence to nevertheless be cut off at $L_{screen} \sim O(U/D_r^h)$, where $D_r^h \sim O(nUL^2/(\ln \kappa)^2)$ is a hydrodynamic rotary diffusivity arising from logarithmically weak pairwise interactions between slender swimmers each of which lead to an $O(1/\ln \kappa)$ angular displacement. This diffusivity has been calculated earlier (Subramanian & Koch 2009), and accounting for this finite D_r^h leads

https://doi.org/10.1017/jfm.2020.827 Published online by Cambridge University Press

to a suspension velocity variance of the form $c_1(nL^3) + (nL^3)^2\{c_2 \ln[(\ln\kappa)^2/(nL^3)] + c_3\}$; although, for reasons discussed above, this estimate will be significantly modified by collective motion (authors' unpublished observations). In the next subsection, we analyse a suspension of interacting RTPs in detail, deriving the above asymptotic forms with the precise expressions for the constants that appear in them. The covariance integral, (3.21), in the strict straight-swimmer limit ($U\tau/L = \infty$) is ill-posed, and therefore, the straight-swimmer limit is better interpreted as a limiting case of persistent RTPs analysed below.

3.3. *Suspensions of interacting RTPs*

The covariance expression in a suspension of interacting slender RTPs remains the same as derived above, and is given by (3.10). However, the kinetic equation governing the pair-probability density must include additional terms compared to (3.12) that describe the tumble dynamics of the individual bacteria. Therefore, in this case, $\hat{\Omega}_2^{(1)}$ satisfies

$$\left(\frac{U\tau}{L}\right)(\boldsymbol{p}_2 - \boldsymbol{p}_1)\cdot\nabla_r\Omega_2^{(1)} + \left(\Omega_2^{(1)} - \frac{1}{4\pi}\int \mathrm{d}\boldsymbol{p}_1\Omega_2^{(1)}\right) + \left(\Omega_2^{(1)} - \frac{1}{4\pi}\int \mathrm{d}\boldsymbol{p}_2\Omega_2^{(1)}\right)$$
$$= -\frac{(nL^3)^2}{(4\pi)^2}\left(\frac{U\tau}{L}\right)\left[\nabla_{p_1}\cdot\dot{\boldsymbol{p}}_{12} + \nabla_{p_2}\cdot\dot{\boldsymbol{p}}_{21}\right]. \tag{3.23}$$

The bracketed terms on the left-hand side of (3.23) correspond to the individual swimmers undergoing tumbles in accordance with Poisson statistics (Subramanian & Koch 2009; Othmer, Dunbar & Alt 1988), with there being no correlation between pre- and post-tumble orientations (random tumbles); τ is the mean run duration (that is, the mean interval between successive random tumbles). In the absence of additional forcing, tumbling causes the single-swimmer distribution to relax to isotropy on a time scale of $O(\tau)$. Here, $U\tau/L$ is a non-dimensional mean run length; thus, $U\tau/L \to \infty$ corresponds to the limiting case of straight-swimmers analysed in the previous subsection. Again, on Fourier transforming, one gets

$$\left(\frac{U\tau}{L}\right)2\pi\mathrm{i}\boldsymbol{k}\cdot(\boldsymbol{p}_2 - \boldsymbol{p}_1)\hat{\Omega}_2^{(1)} + \left(2\hat{\Omega}_2^{(1)} - \frac{1}{4\pi}\int \mathrm{d}\boldsymbol{p}_1\hat{\Omega}_2^{(1)} - \frac{1}{4\pi}\int \mathrm{d}\boldsymbol{p}_2\hat{\Omega}_2^{(1)}\right)$$
$$= -\frac{(nL^3)^2}{(4\pi)^2}\left(\frac{U\tau}{L}\right)\left[\nabla_{p_1}\cdot\hat{\dot{\boldsymbol{p}}}_{12} + \nabla_{p_2}\cdot\hat{\dot{\boldsymbol{p}}}_{21}\right]. \tag{3.24}$$

One may, in fact, obtain an analytical solution for $\hat{\Omega}_2^{(1)}(\boldsymbol{p}_1, \boldsymbol{p}_2; \boldsymbol{k})$ in (3.24), for arbitrary $U\tau/L$, by determining of the linear operator on the left-hand side. This requires one to first solve the time dependent operator, and then obtain the steady-state pair-probability density by taking the long-time limit. The solution procedure involves the spectral representation of the Green's function in terms of an eigenfunction expansion. Further, the singular nature of the linear operator implies that both the discrete and (singular) continuous spectra need to be accounted for in this expansion. For the sake of brevity, we will be reporting this detailed Green's function analysis elsewhere (authors' unpublished observations).

For purposes of the present calculation, one notes that the symmetry of the orientation dilatation forcing terms on the right-hand side of (3.24) ensures that one does not require information contained in the full Green's function. A representation of $\hat{\Omega}_2^{(1)}$ as a convolution of the Green's function with the right-hand side of (3.24) implies that

https://doi.org/10.1017/jfm.2020.827 Published online by Cambridge University Press

only those eigenfunctions in the aforementioned spectral expansion, that the orientation dilatation terms project onto, contribute. To see this, we again choose a spherical polar coordinate system with its polar axis along $\hat{\boldsymbol{k}}$, with θ_1 and θ_2 representing the polar angles, and ϕ being the relative azimuthal angle between the two swimmers, measured in a plane perpendicular to $\boldsymbol{k}$ (similar to that described in § 3.2). In this coordinate system, the orientation dilatation terms are proportional to $\cos\phi$ and, hence, vanish when integrated in orientation space. Thus, one only needs to solve for the eigenmodes proportional to $\cos\phi$ in the full expansion for the pair-probability density. Now, eigenmodes proportional to $\cos(n\phi)$ or $\sin(m\phi)$ remain unaffected by the integral terms in (3.24) for $m, n \neq 0$, since the latter vanish for all such cases; physically, the orientation dilatation terms lead to pure-orientation correlations without concentration (number density) perturbations. Thus, one may set $\int \hat{\Omega}_2^{(1)}\,\mathrm{d}\boldsymbol{p}_1 = \int \hat{\Omega}_2^{(1)}\,\mathrm{d}\boldsymbol{p}_2 = 0$ in (3.24), and the governing equation for $\hat{\Omega}_2^{(1)}$ (for purposes of determining the covariance) reduces to the following much simpler algebraic form:

$$\left(\frac{U\tau}{L}\right) 2\pi\mathrm{i}\boldsymbol{k}\cdot(\boldsymbol{p}_2-\boldsymbol{p}_1)\hat{\Omega}_2^{(1)} + 2\hat{\Omega}_2^{(1)} = -\frac{(nL^3)^2}{(4\pi)^2}\left(\frac{U\tau}{L}\right)\left[\nabla_{p_1}\cdot\hat{\dot{\boldsymbol{p}}}_{12} + \nabla_{p_2}\cdot\hat{\dot{\boldsymbol{p}}}_{21}\right]. \tag{3.25}$$

Solving (3.25) is straightforward, and yields the following exact expression:

$$\hat{\Omega}_2^{(1)} = \frac{3(nL^3)^2}{32\pi^5 k^2}\left(\frac{U\tau}{L}\right)\left(\frac{1}{\pi\mathrm{i}(U\tau/L)\boldsymbol{k}\cdot(\boldsymbol{p}_2-\boldsymbol{p}_1)+1}\right)\left(\boldsymbol{I}-\hat{\boldsymbol{k}}\hat{\boldsymbol{k}}\right):\boldsymbol{p}_2\boldsymbol{p}_1$$
$$\times\left[\frac{1}{(\boldsymbol{k}\cdot\boldsymbol{p}_1)}\sin^2\left(\frac{\pi}{2}\boldsymbol{k}\cdot\boldsymbol{p}_1\right)\sin\left(\pi\boldsymbol{k}\cdot\boldsymbol{p}_2\right) + \frac{1}{(\boldsymbol{k}\cdot\boldsymbol{p}_2)}\sin^2\left(\frac{\pi}{2}\boldsymbol{k}\cdot\boldsymbol{p}_2\right)\sin\left(\pi\boldsymbol{k}\cdot\boldsymbol{p}_1\right)\right]. \tag{3.26}$$

The pair-correlation function for RTPs above does not involve any concentration fluctuations, as may be seen by integrating (3.26) over orientation space ($\boldsymbol{p}_1$ and $\boldsymbol{p}_2$). This implies that the pair distribution function, $g(r) = (nL^3)^{-2}\int \Omega_2\,\mathrm{d}\boldsymbol{p}_1\,\mathrm{d}\boldsymbol{p}_2$ is just unity. Therefore, pair-correlations between slender swimmers involve only the orientation degrees of freedom, with the swimmer concentration (positional) fluctuations still predicted to be similar to that in the absence of interactions (and, therefore, Poissonian in character); this is consistent with the simulation results of Underhill & Graham (2011). In fact, recent simulations show that the pair distribution function remains close to unity even after the onset of collective motion (Krishnamurthy & Subramanian 2015; Bárdfalvy *et al.* 2019). From (3.26), one can also infer that for large $U\tau/L$, $\hat{\Omega}_2^{(1)} \sim O(1/k)$ in the range $U\tau/L \gg 1/k \gg 1$ and, therefore, $\Omega_2^{(1)}$ has the character of an $O(1/r^2)$ decay for $1 \ll r \ll U\tau/L$. Recall the discussion in § 3.2, where this algebraic decay of $\Omega_2^{(1)}$ led to a logarithmically divergent variance in the limit $U\tau/L \to \infty$ (straight-swimmers); in appendix B, we recover the straight-swimmer form of the pair-probability density from (3.26). For any large but finite $U\tau/L$, however, $\Omega_2^{(1)}$ exhibits faster-than-algebraic decay for $r \gg U\tau/L$, on account of decorrelations induced by tumbling. In the other limit of rapid tumblers, corresponding to $U\tau/L \ll 1$, $\Omega_2^{(1)}$ directly transitions to a faster-than-algebraic decay for $r \gg 1$.

Now, using (3.26) in (3.10), and on inverse Fourier transforming, one obtains the correlated contribution to the fluid velocity covariance in a suspension of interacting RTPs

https://doi.org/10.1017/jfm.2020.827 Published online by Cambridge University Press

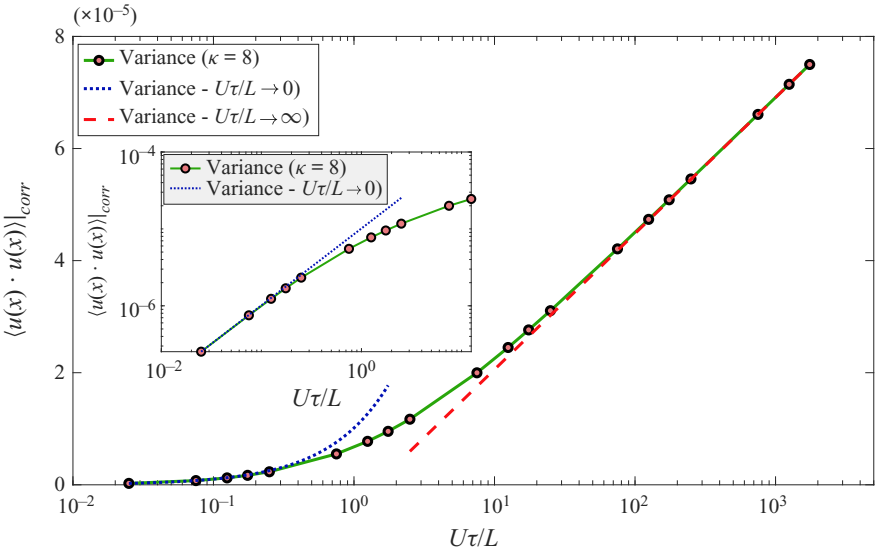


FIGURE 4. The $O(nL^3)^2$ correlated variance, as given by (3.28), plotted as a function of $U\tau/L$. The small (dotted) and large (dash-dotted) $U\tau/L$ asymptotes are shown; the inset highlights the linear scaling of the correlated variance with $U\tau/L$ for $U\tau/L \ll 1$.

to be

$$\langle \boldsymbol{u}(\boldsymbol{x}) \cdot \boldsymbol{u}(\boldsymbol{x}+\boldsymbol{r})\rangle|_{corr} = \frac{3(nL^3)^2}{128\pi^6(\ln\kappa)^3 r}\left(\frac{U\tau}{L}\right)\int_0^\infty \mathrm{d}k \frac{\sin(2\pi k r)}{k^5}\int_{-1}^{1}\mathrm{d}\mu_1\int_{-1}^{1}\mathrm{d}\mu_2(1-\mu_1^2) \times (1-\mu_2^2)\left(\frac{1}{1+\pi\mathrm{i}(U\tau/L)k(\mu_2-\mu_1)}\right)\sin^2\left(\frac{\pi}{2}k\mu_1\right)\sin^2\left(\frac{\pi}{2}k\mu_2\right) \times j_0\left(\frac{\pi}{2}k\mu_1\right)j_0\left(\frac{\pi}{2}k\mu_2\right)\left[\cos\left(\frac{\pi}{2}k\mu_2\right)j_0\left(\frac{\pi}{2}k\mu_1\right) + \cos\left(\frac{\pi}{2}k\mu_1\right)j_0\left(\frac{\pi}{2}k\mu_2\right)\right], \tag{3.27}$$

where $\mu_i \equiv \cos\theta_i$. The correlated variance is obtained by setting $r = 0$ in (3.27), and is expressible as

$$\langle \boldsymbol{u}(\boldsymbol{x}) \cdot \boldsymbol{u}(\boldsymbol{x})\rangle|_{corr} = \frac{3(nL^3)^2}{64\pi^5(\ln\kappa)^3}\left(\frac{U\tau}{L}\right)\int_0^\infty \mathrm{d}k \frac{1}{k^4}\int_{-1}^{1}\mathrm{d}\mu_1\int_{-1}^{1}\mathrm{d}\mu_2(1-\mu_1^2)(1-\mu_2^2) \times\left(\frac{1}{1+\pi\mathrm{i}(U\tau/L)k(\mu_2-\mu_1)}\right)\sin^2\left(\frac{\pi}{2}k\mu_1\right)\sin^2\left(\frac{\pi}{2}k\mu_2\right)j_0\left(\frac{\pi}{2}k\mu_1\right) \times j_0\left(\frac{\pi}{2}k\mu_2\right)\left[\cos\left(\frac{\pi}{2}k\mu_2\right)j_0\left(\frac{\pi}{2}k\mu_1\right) + \cos\left(\frac{\pi}{2}k\mu_1\right)j_0\left(\frac{\pi}{2}k\mu_2\right)\right]. \tag{3.28}$$

In figure 4, we plot the correlated variance given by (3.28). For $U\tau/L \ll 1$, owing to the aforementioned rapid decay of $\Omega_2^{(1)}$, the correlated variance scales as $c_1(U\tau/L)(nL^3)^2$ (see inset of figure 4). This estimate arises from neglecting the factor $\pi\mathrm{i}(U\tau/L)k(\mu_2-\mu_1)$ in the denominator of the right-hand side in (3.28). For large $U\tau/L$, in accordance with earlier scaling arguments, the correlated variance in suspensions of interacting RTPs takes

https://doi.org/10.1017/jfm.2020.827 Published online by Cambridge University Press

the form $c_2(nL^3)^2/(\ln\kappa)^3\ln(U\tau/L)$. As stated above, this is a consequence of the $O(1/k)$ scaling of $\Omega_2^{(1)}$ for persistent RTPs, which leads to a logarithmic divergence in (3.28) that is eventually cut off for $k\sim O(U\tau/L)^{-1}$.

In figure 5, the correlated covariance is plotted for pusher-type suspensions. For rapid tumblers ($U\tau/L\ll 1$), the covariance directly transitions from the initial variance plateau to an $O(1/r)$ far-field decay for $r\gg 1$. The nature of this far-field decay remains the same irrespective of $U\tau/L$. For $U\tau/L\ll 1$, the far-field decay occurs when $r\gg 1$, whereas, for $U\tau/L\gg 1$, this only occurs when $r\gg U\tau/L$. To obtain this far-field dipole asymptote, one may rescale the outer integral variable to be $\tilde{k}=kr$, and seek the asymptotic form of (3.27) for $\tilde{k}\sim O(1)$ but $r\gg 1$. Using the approximations $\sin[\pi\tilde{k}\mu_i/(2r)]\approx\pi\tilde{k}\mu_i/(2r)$, $j_0[\pi\tilde{k}\mu_i/(2r)]\approx 1$ and neglecting the term involving $(\mu_2-\mu_1)$, one finally obtains the covariance as $\langle\boldsymbol{u}(\boldsymbol{x})\cdot\boldsymbol{u}(\boldsymbol{x}+\boldsymbol{r})\rangle|_{corr}=3(nL^3)^2(U\tau/L)(28\,800\pi r)^{-1}$. The inset in figure 5 plots the correlated covariance as a function of $r(U\tau/L)^{-1}$, highlighting the far-field collapse of the far-field asymptotes for $r\gg U\tau/L$. Both from figure 5 and the inset therein, one notes, for $U\tau/L\gg 1$, the emergence of an intermediate asymptotic regime following the variance plateau, characterized by a weak decay in the range $1\ll r\ll U\tau/L$. As is shown in detail in appendix C, the weak decay of the covariance in the intermediate region is a logarithmic one, scaling as $O(\ln[r/(U\tau)])$.

One may now write down the expression for the total variance in a suspension of interacting RTPs by adding the variance expression for suspensions of non-interacting swimmers given below (3.8) (see § 3.1), and the correlated contribution to the variance given by (3.28) above. This is expressible as

$$\begin{aligned}&\langle\boldsymbol{u}(\boldsymbol{x})\cdot\boldsymbol{u}(\boldsymbol{x})\rangle\\&=\frac{(nL^3)}{96\pi(\ln\kappa)^2}\pm\frac{3(nL^3)^2}{64\pi^5(\ln\kappa)^3}\left(\frac{U\tau}{L}\right)\int_0^\infty\frac{\mathrm{d}k}{k^4}\int_{-1}^1\mathrm{d}\mu_1\int_{-1}^1\mathrm{d}\mu_2(1-\mu_1^2)(1-\mu_2^2)\\&\times\left(\frac{1}{1+\pi\mathrm{i}(U\tau/L)k(\mu_2-\mu_1)}\right)\sin^2\left(\frac{\pi}{2}k\mu_1\right)\sin^2\left(\frac{\pi}{2}k\mu_2\right)\\&\times j_0\left(\frac{\pi}{2}k\mu_1\right)j_0\left(\frac{\pi}{2}k\mu_2\right)\left[\cos\left(\frac{\pi}{2}k\mu_2\right)j_0\left(\frac{\pi}{2}k\mu_1\right)+\cos\left(\frac{\pi}{2}k\mu_1\right)j_0\left(\frac{\pi}{2}k\mu_2\right)\right],\end{aligned}\tag{3.29}$$

where the positive and negative signs pertain to suspensions of pushers and pullers, respectively. Based on the preceding arguments, in a suspension of pusher-type swimmers, the total variance scales as $c_1(nL^3)/(\ln\kappa)^2+(nL^3)^2/(\ln\kappa)^3[c_2\ln[U\tau/L]+c_3]$ for large $U\tau/L$, and as $c_1(nL^3)/(\ln\kappa)^2+c_2(U\tau/L)(nL^3)^2/(\ln\kappa)^3$ for $U\tau/L\ll 1$. An important implication of including correlations is the scaling of the variance with the dipole strength. The $O(nL^3)$ contribution of the variance involves a dimensional scaling of $(U/\ln\kappa)^2$, implying that it scales as the square of the dipole strength D (measured in units of ηUL^2). However, the correlated contribution to the variance is proportional to $(U/\ln\kappa)^3$ and, thence, to D^3. Thus, the variance for a suspension of pairwise interacting RTPs depends on the sign of D ($D<0$ for pushers and >0 for pullers) and, therefore, on the swimming mechanism. Consistent with recent simulations (Krishnamurthy & Subramanian 2015; Stenhammar *et al.* 2017), at $O(nL^3)^2$, (3.29) predicts enhanced fluctuations in suspensions of pusher-type swimmers. In figure 6, this enhancement is approximately 30 % for an nL^3 of approximately 4, and for $U\tau/L=125$. As mentioned in § 2, the enhancement is much greater for tracer diffusivities on account of the linear scaling in $U\tau/L$ (see § 4.3).

https://doi.org/10.1017/jfm.2020.827 Published online by Cambridge University Press

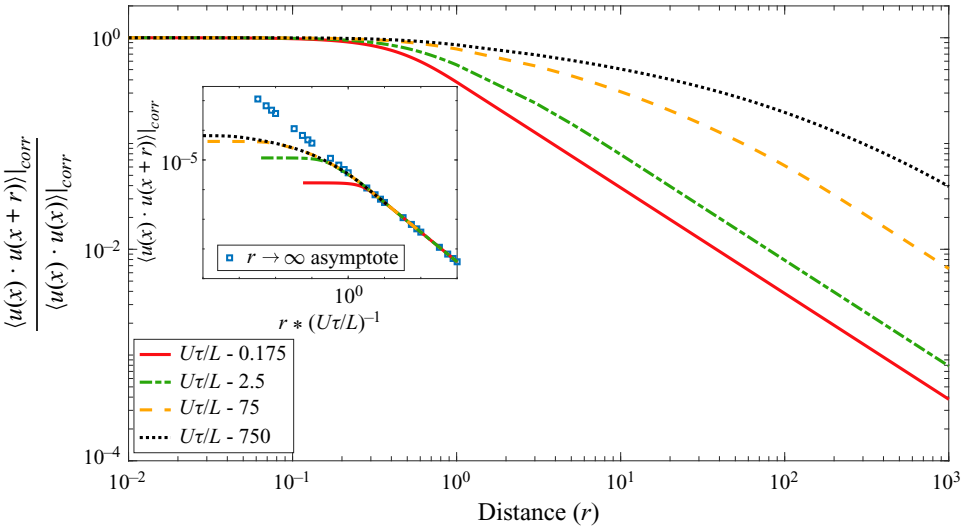


FIGURE 5. The $O(nL^3)^2$ component of the (normalized) fluid velocity covariance as a function of r. In the inset the covariance curves collapse onto the far-field dipole asymptote (represented by the □ symbols) stated below (3.27), for $r \gg U\tau/L$, when the abscissa is scaled with $(U\tau/L)^{-1}$.

The total covariance in a suspension of interacting RTPs can be similarly expressed by combining (3.8) and (3.27), which gives

$$\begin{aligned}
&\langle \boldsymbol{u}(\boldsymbol{x})\cdot\boldsymbol{u}(\boldsymbol{x}+\boldsymbol{r})\rangle \\
&\quad= \frac{1}{4\pi^6 r}\int_0^\infty \mathrm{d}k \frac{\sin(2\pi k r)}{k^5}\left\{\frac{(nL^3)}{(\ln\kappa)^2}\int_{-1}^{1}\mathrm{d}\mu\left(\frac{1-\mu^2}{\mu^2}\right)\sin^4\left(\frac{\pi k\mu}{2}\right)\right. \\
&\qquad\pm \frac{3(nL^3)^2}{32(\ln\kappa)^3}\left(\frac{U\tau}{L}\right)\int_{-1}^{1}\mathrm{d}\mu_1\int_{-1}^{1}\mathrm{d}\mu_2(1-\mu_1^2)(1-\mu_2^2) \\
&\qquad\times\left(\frac{1}{1+\pi\mathrm{i}(U\tau/L)k(\mu_2-\mu_1)}\right)\sin^2\left(\frac{\pi}{2}k\mu_1\right)\sin^2\left(\frac{\pi}{2}k\mu_2\right) \\
&\qquad\left.\times j_0\left(\frac{\pi}{2}k\mu_1\right)j_0\left(\frac{\pi}{2}k\mu_2\right)\left[\cos\left(\frac{\pi}{2}k\mu_2\right)j_0\left(\frac{\pi}{2}k\mu_1\right)+\cos\left(\frac{\pi}{2}k\mu_1\right)j_0\left(\frac{\pi}{2}k\mu_2\right)\right]\right\},
\end{aligned} \tag{3.30}$$

where the positive sign, corresponding to an increase in the covariance due to correlations, pertains to suspensions of pushers. Figure 7 shows a plot of (3.30) as a function of r for $nL^3 = 5$, for pusher suspensions (the positive sign in (3.30)). Note that the chosen nL^3 is a little greater than unity. There is evidence, from earlier calculations for suspensions of non-Brownian slender fibres, that the dilute theory, with pair interactions accounted for, remains valid for nL^3 up until around 7 (Mackaplow & Shaqfeh 1996); the extended regime of validity for the dilute approximation is also evident for Brownian fibre suspensions, where the transition of the single fibre self-diffusivity from the isolated Stokes–Einstein value (valid in the dilute regime) to an $O(nL^3)^{-2}$ scaling arising from steric hindrance, characteristic of the semidilute regime, occurs only at an nL^3 of approximately 16 (see chapter 10 in Larson (2013)). In figure 7, for large $U\tau/L$, while the variance plateau only grows slowly with increasing $U\tau/L$, owing to the $\ln U\tau/L$ scaling of the correlated

https://doi.org/10.1017/jfm.2020.827 Published online by Cambridge University Press

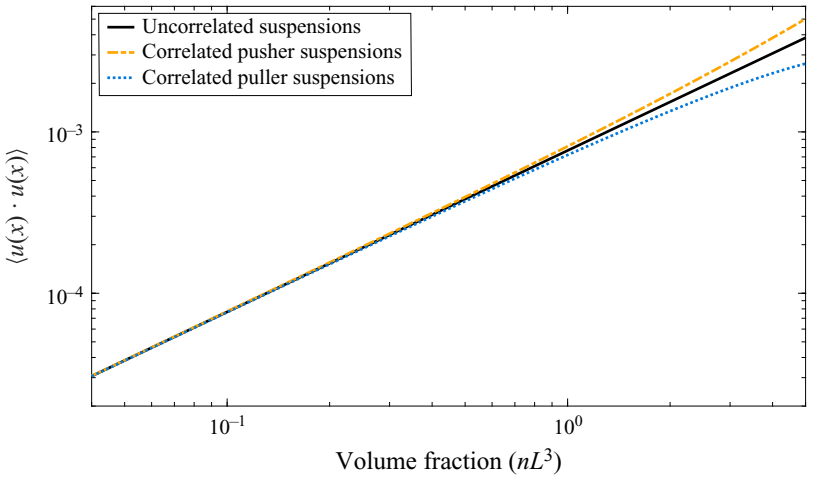


FIGURE 6. The total velocity variance plotted as a function of the swimmer volume fraction (nL^3) at $U\tau/L = 125$, for both pushers and pullers, along with the uncorrelated contribution (solid line). The swimmer aspect ratio is chosen to be $\kappa = 8$.

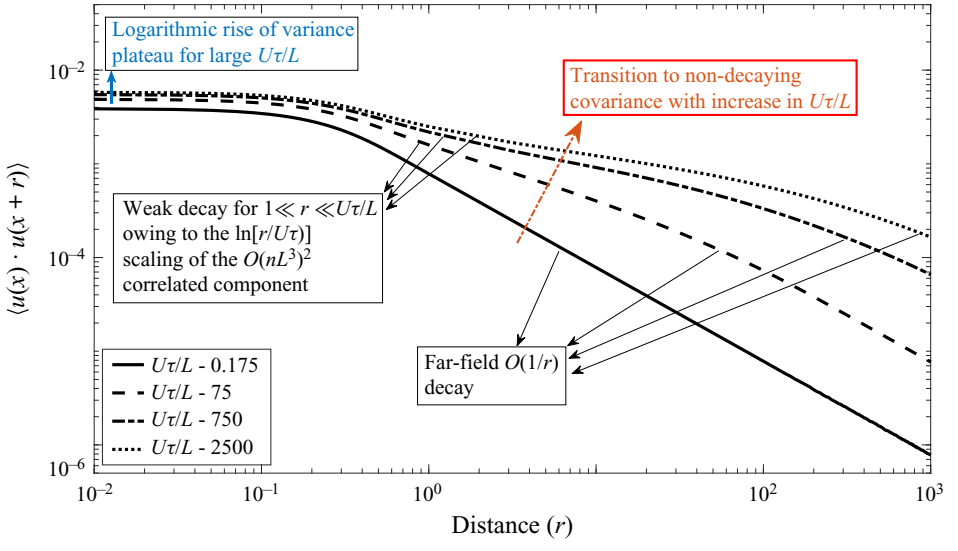


FIGURE 7. The total fluid velocity covariance for a suspension of pusher-type RTPs plotted as a function of r over a range of $U\tau/L \in [0.125, 750]$, and for $nL^3 = 5$. The red (dash-dotted) arrow highlights the direction of increasing $U\tau/L$. The swimmer aspect ratio is chosen to be $\kappa = 8$.

component, the far-field $O(1/r)$ scaling grows faster on account of the linear scaling with $U\tau/L$ (see the expression for the far-field asymptote below (3.28)). This differential growth results in the total covariance developing a shoulder in the intermediate regime ($1 \ll r \ll U\tau/L$).

We now analyse the weak decay of the correlated component of the covariance in the intermediate asymptotic regime (corresponding to the shoulder) mentioned in the above discussion. Although the exact solution given by (3.27) is valid for arbitrary $U\tau/L$, the form of the intermediate regime is not obvious. Therefore, for large $U\tau/L$, we derive an alternate simpler approximation which reveals an intermediate asymptotic regime

https://doi.org/10.1017/jfm.2020.827 Published online by Cambridge University Press

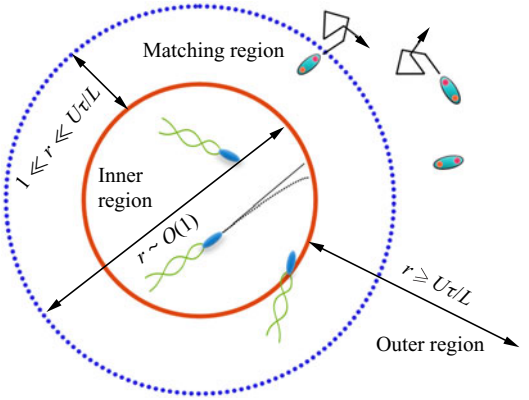


FIGURE 8. A schematic showing the three distinct physical regions for $U\tau/L \gg 1$. The inner region corresponds to $r \sim O(1)$, where we have slender straight-swimmers, and the correlations develop over straight trajectories. The outer region $r \sim U\tau/L$ corresponds to the run-and-tumble dynamics of point force-dipoles. In the intermediate region of overlap, $1 \ll r \ll U\tau/L$, the inner and outer solutions must assume a common asymptotic form.

of shallow decay for separations in the range $1 \ll r \ll U\tau/L$ (as implied by figures 5 and 7). In this limit, owing to a separation of scales corresponding to those of order the swimmer size and those comparable to the run length, the method of matched asymptotic expansions is applicable. The details of the analysis are quite involved, and are therefore relegated to appendix C. The nature of the different asymptotic regions involved may, however, be readily explained. In a reference frame moving with one of the swimmers (termed the 'test swimmer'), the physical domain may be divided into the following two regions.

(i) An inner region $r \sim O(1) \ll U\tau/L$, where the pair of swimmers move relative to each other predominantly in straight trajectories. In this region, one may approximate the correlations induced by the swimmer disturbance velocity fields as those that develop along straight-swimmer trajectories. The expressions pertaining to this region have already been obtained as part of the straight-swimmer analysis given in § 3.2.

(ii) An outer region $r \sim O(U\tau/L)(\gg 1)$, where orientation decorrelation due to random tumbles need to be taken into account. However, given the large separations, the pair of swimmers may be treated as point force-dipoles. Neglect of the finite swimmer size allows for a considerable simplification of the expressions of the rotation rates ($\dot{\boldsymbol{p}}_{ij}$) involved (see appendix A).

The matching region, which therefore corresponds to straight-swimming point force-dipoles interacting in the range $1 \ll r \ll U\tau/L$, is the region where the expressions in both the inner and outer regions must reduce to a common form. A schematic highlighting the aforementioned demarcation of the physical domain, is shown in figure 8 (see also appendix C). One expects that in the inner region the covariance has a non-decaying character on account of the strong correlations between interacting straight-swimmers. In the outer region, there is a transition to the eventual $O(1/r)$ decay for $r \geqslant U\tau/L$, characteristic of interacting RTPs; the covariance plotted in figure 5 does conform to these scalings. The matched asymptotic expansions calculation in appendix C

https://doi.org/10.1017/jfm.2020.827 Published online by Cambridge University Press

yields the following expression for the correlated component of the covariance:

$$\begin{aligned}
&\langle \boldsymbol{u}(\boldsymbol{x})\cdot\boldsymbol{u}(\boldsymbol{x}+\boldsymbol{r})\rangle_{corr-matched}\\
&= \frac{(nL^3)^2D^3}{\pi^2 r}\left\{\int_0^1 \mathrm{d}k\int_{-1}^1 \mathrm{d}\mu\left[\frac{3}{2\pi^4}\frac{\sin(2\pi kr)}{k^6}(1-\mu^2)^2\right.\right.\\
&\quad\left.\times\sin(\pi k\mu)\left(j_0\left(\frac{\pi}{2}k\mu\right)\right)^3\sin^3\left(\frac{\pi}{2}k\mu\right)-\frac{1}{105}\frac{\sin(2\pi kr)}{k^2}\right]\\
&\quad+\int_1^\infty \mathrm{d}k\frac{\sin(2\pi kr)}{k^6}\int_{-1}^1 \mathrm{d}\mu\frac{3}{2\pi^4}(1-\mu^2)^2\left(j_0\left(\frac{\pi}{2}k\mu\right)\right)^3\sin^3\left(\frac{\pi}{2}k\mu\right)\Bigg\}\\
&\quad+(nL^3)^2D^3\left\{\frac{3}{16\pi^2 r_1}\int_0^\infty\frac{1}{k_1}\sin(2\pi k_1 r_1)\,\mathrm{d}k_1\int_{-1}^1\mathrm{d}\mu_1\right.\\
&\quad\times\int_{-1}^1\mathrm{d}\mu_2\frac{\mu_1^2\mu_2^2(1-\mu_1^2)(1-\mu_2^2)}{1+\pi^2\left(\dfrac{U\tau}{L}\right)k_1^2(\mu_2-\mu_1)^2}-\frac{2}{105\pi}\left[j_0(2\pi r_1)-C_i(2\pi r_1)\right]\Bigg\}\\
&\quad+\frac{2(nL^3)^2D^3}{105\pi}\left\{\ln(2\pi r)-j_0(2\pi r)+\int_0^{2\pi r}\frac{\cos(t)-1}{t}\,\mathrm{d}t\right.\\
&\quad\left.+j_0(2\pi r_1)-C_i(2\pi r_1)+\gamma_E\right\},
\end{aligned}\tag{3.31}$$

where $C_i(x)$ represents the cosine integral (Gradshteyn & Ryzhik 1980), $r_1 = rL/(U\tau)$ and k_1 the corresponding wavenumber; $D = 1/(4\ln\kappa)$ is the non-dimensional dipole strength corresponding to dipole swimmers. There are three sets of braced terms on the right-hand side of (3.31), and we briefly explain these in the following. In applying the matched asymptotic expansions method, one needs to take care of the apparent divergences that arise in a naïve straight-swimmer approximation. In the outer region, the slender straight-swimmer covariance has a non-decaying character, whereas, in the inner region, the far-field dipole approximation diverges, owing to the $O(1/r^2)$ scaling of the dipole velocity field. Therefore, one must ensure that both of the aforementioned divergences are accounted for and isolated in the matching scheme. In (3.31), the first set of braces on the right-hand side corresponds to the slender straight-swimmer contribution with a far-field divergence due to straight-swimming dipoles subtracted off. To avoid the (obvious) divergence of the subtracted dipoles in the inner region $k \to \infty$ ($r \to 0$), we set an upper bound on the k-integration of the subtracted component. The second set of braces corresponds to the far-field dipole contribution, now, with the inner-region divergence due to straight-swimming dipoles subtracted off. Thus, in this case, we set a lower bound in the k_1 integration of the subtracted quantity to again ensure that the region $k_1 \to 0$ ($r_1 \to \infty$) is removed. We add back these subtracted contributions in the third set of braces in (3.31). Note that it is the third grouping alone that depends on $U\tau/L$, and exhibits the required logarithmic scaling.

In figure 9, we compare the correlated contributions to the covariance calculated from (3.27) and (3.31). The matched asymptotic expansions approach yields excellent agreement with the exact covariance for the three largest values of $U\tau/L$, and remains a good approximation down to $U\tau/L = 7.5$. As stated in the aforementioned discussion, it is the straight-swimming point force-dipole contribution in the third set of braces on the right-hand side of (3.31), that captures the functional form in the intermediate

https://doi.org/10.1017/jfm.2020.827 Published online by Cambridge University Press

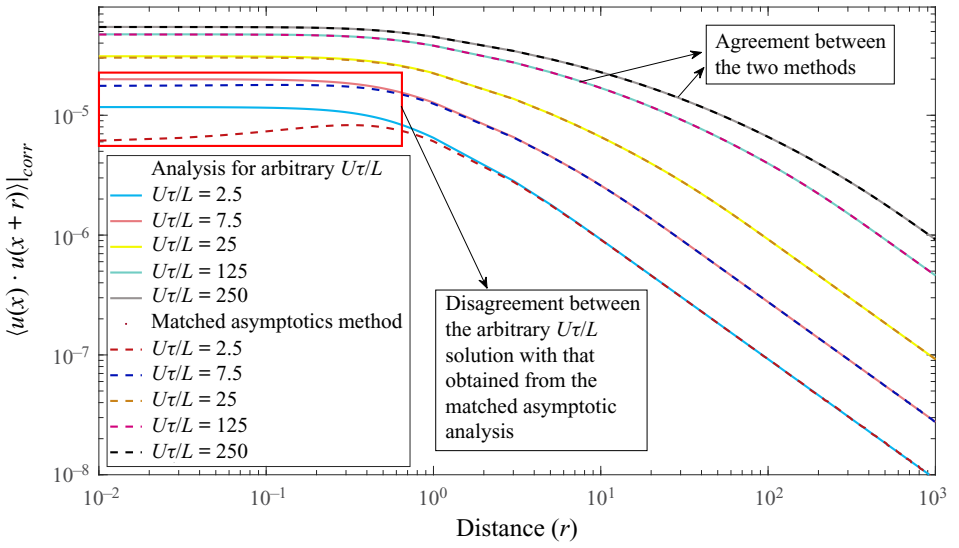


FIGURE 9. The fluid velocity covariance for arbitrary $U\tau/L$ from (3.27) (straight curves) is plotted alongside the same determined by the method of matched asymptotic expansion (3.31) (dashed curves), for $U\tau/L = 2.5, 7.5, 25, 125, 250$. The swimmer aspect ratio is chosen to be $\kappa = 8$.

asymptote regime. This term simplifies to $2(nL^3)^2/(105\pi)[1 - \gamma_E - \ln(2\pi r_1)]$, thereby exhibiting an $O(\ln[rL/(U\tau)])$ decay. Thus, the aforementioned weak decay of the $O(nL^3)^2$ component of the covariance, is a logarithmic one, and as $U\tau/L \to \infty$, one asymptotes to a non-decaying covariance in the straight-swimmer limit. The logarithmic functional form alone is compared with the exact solution for the full covariance, for $U\tau/L = 750$ in figure 10; a good agreement is obtained in the intermediate range of separations $1 \ll r \ll U\tau/L$.

Therefore, for $U\tau/L \gg 1$, the behaviour of the covariance, in an interacting suspension may be summarized as follows:

(i) for $r \ll 1$, it exhibits a finite variance plateau, with the variance itself scaling as $\ln U\tau/L$;
(ii) for $1 \ll r \ll U\tau/L$, it exhibits a weak decay proportional to $O(\ln[rL/(U\tau)])$;
(iii) for $r \gg U\tau/L$, corresponding to the far-field, it decays as $O(1/r)$.

4. Tracer diffusivity

The fluctuating suspension velocity field analysed in § 3 convects an immersed passive tracer. The dynamics of such a non-Brownian tracer is governed by

$$\dot{\boldsymbol{x}} = \boldsymbol{u}(\boldsymbol{x}, t), \tag{4.1}$$

where $\boldsymbol{u}(\boldsymbol{x}, t)$ is the suspension velocity field defined in (3.3). During a tracer–slender swimmer interaction, the convecting velocity field, that of a slender swimmer, is $O(U/\ln\kappa)$ on the length scales of interest, while the relative tracer–swimmer velocity is $O(U)$. Thus, the tracer displacement during an interaction event is of a logarithmically smaller order, and the tracer statistics may be calculated within the

https://doi.org/10.1017/jfm.2020.827 Published online by Cambridge University Press

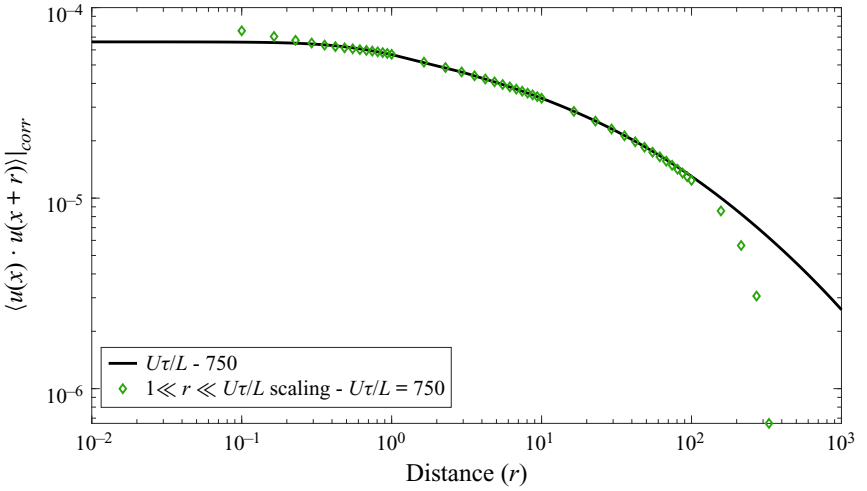


FIGURE 10. The correlated contribution to the fluid velocity covariance for $U\tau/L = 750$ and $\kappa = 8$ obtained from (3.27) (straight curves), along with the intermediate logarithmic scaling ($\diamond$) in the regime $1 \ll r \ll U\tau/L$ obtained from (C 8) in appendix C.

Eulerian approximation – that is, to leading logarithmic order, the tracer position may be regarded as fixed when calculating the interaction-induced displacement (Kasyap *et al.* 2014). The expression for the MSD of the tracer, at time t, is then given in terms of the fluid velocity autocorrelation function as

$$\langle x^2(t)\rangle = \int_0^t \mathrm{d}t_1 \int_0^t \mathrm{d}t_2 \langle \boldsymbol{u}(\boldsymbol{r}, t_1) \cdot \boldsymbol{u}(\boldsymbol{r}, t_2)\rangle, \tag{4.2}$$

where the angular brackets again denote an ensemble average over the swimmer configurations (Zwanzig 2001; Balakrishnan 2008). In terms of the Fourier-transformed variables, the tracer MSD is

$$\langle x^2(t)\rangle = \int \mathrm{d}\boldsymbol{k} \int_0^t \mathrm{d}t_1 \int_0^t \mathrm{d}t_2 \langle \hat{\boldsymbol{u}}(\boldsymbol{k}, t_1) \cdot \hat{\boldsymbol{u}}(-\boldsymbol{k}, t_2)\rangle. \tag{4.3}$$

Following the discussion in § 3, we analyse the tracer MSD to $O(nL^3)^2$; thus, one may write

$$\langle x^2(t)\rangle = \langle x^2(t)\rangle|_{uncorr} + \langle x^2(t)\rangle|_{corr}, \tag{4.4}$$

where $\langle x^2(t)\rangle|_{uncorr} \sim O(nL^3)$ is the tracer MSD in a non-interacting suspension arising from the cumulative effects of all possible single-swimmer–tracer interactions, while $\langle x^2(t)\rangle|_{corr} \sim O(nL^3)^2$ denotes the correlated contribution arising from interactions between a tracer and a pair of correlated swimmers, with the latter correlation being characterized by the pair-probability density derived above. It is worth reiterating that, as for the variance, the dominant interactions that contribute to the tracer diffusivity correspond to swimmer–tracer separations of $O(L)$.

https://doi.org/10.1017/jfm.2020.827 Published online by Cambridge University Press

4.1. *Suspensions of non-interacting swimmers*

For non-interacting swimmers, the Fourier-transformed velocity correlation function is given by

$$\langle \hat{\boldsymbol{u}}(\boldsymbol{k}, t_1) \cdot \hat{\boldsymbol{u}}(-\boldsymbol{k}, t_2)\rangle|_{uncorr} = \int \hat{\boldsymbol{u}}(\boldsymbol{k}) \cdot \hat{\boldsymbol{u}}(-\boldsymbol{k}) \hat{G}_1 \left(\boldsymbol{p}_1, t_1 | \boldsymbol{p}_1', t_2; \boldsymbol{k}\right) \Omega_1 \, \mathrm{d}\boldsymbol{p}_1 \, \mathrm{d}\boldsymbol{p}_1', \tag{4.5}$$

where $\hat{\boldsymbol{u}}(\boldsymbol{k})$ is the Fourier-transformed disturbance velocity field (see (A 2)), $\Omega_1 = nL^3/4\pi$ is the steady-state singlet probability density and $\hat{G}_1(\boldsymbol{p}_1, t_1|\boldsymbol{p}_1', t_2; \boldsymbol{k})$ is the Fourier-transformed transition probability of finding a swimmer with orientation $\boldsymbol{p}_1$ at time t_1 given that the swimmer had an orientation $\boldsymbol{p}_1'$ at t_2. The governing equation for $\hat{G}_1$ is

$$\frac{\mathrm{d}\hat{G}_1}{\mathrm{d}t} + \left(\frac{U\tau}{L}\right) 2\pi \mathrm{i}\boldsymbol{k} \cdot \boldsymbol{p}_1 \hat{G}_1 + \left(\hat{G}_1 - \frac{1}{4\pi}\int \mathrm{d}\boldsymbol{p}_1 \hat{G}_1\right) = \boldsymbol{\delta}(\boldsymbol{p}_1 - \boldsymbol{p}_1')\delta(t - t'). \tag{4.6}$$

The orientation-space eigenmodes of the operator governing the transition probability density, $\hat{G}_1$ in (4.6), that contribute to the velocity-correlation function, have no concentration fluctuations. Thus, for these modes, the inverse-tumbling term in (4.6) vanishes and the expression for $\hat{G}_1$ is then easily given as

$$\hat{G}_1 \left(\boldsymbol{p}_1, t | \boldsymbol{p}_1', t'; \boldsymbol{k}\right) = \delta(\boldsymbol{p}_1 - \boldsymbol{p}_1') \exp\left(\left(-2\pi \mathrm{i}\boldsymbol{k} \cdot \boldsymbol{p}_1 \frac{U\tau}{L} - 1\right)(t - t')\right). \tag{4.7}$$

We emphasize that this expression for $\hat{G}_1$ does not capture the relaxation of the concentration modes. The complete expression for $\hat{G}_1$, including the concentration modes, is needed to characterize the time-dependent evolution of an initially localized population of run-and-tumble swimmers, and will be reported separately (authors' unpublished observations). Using the above result, and upon simplifying, we obtain the expression for the MSD of a passive tracer as

$$\begin{aligned}\langle x^2(t)\rangle|_{uncorr} = {} & \frac{nL^3}{(\ln\kappa)^2 8\pi^7} \int \mathrm{d}\boldsymbol{p}_1 \int \frac{\mathrm{d}\boldsymbol{k}}{k^4} \left(\frac{-1 + \exp\left(-\left(2\pi \mathrm{i}\boldsymbol{k} \cdot \boldsymbol{p}_1 \dfrac{U\tau}{L} + 1\right) t\right)}{\left(2\pi \mathrm{i}\boldsymbol{k} \cdot \boldsymbol{p}_1 \dfrac{U\tau}{L} + 1\right)^2}\right) \\ & \times \left(\boldsymbol{I} - \frac{\boldsymbol{k}\boldsymbol{k}}{k^2}\right) : \boldsymbol{p}_1\boldsymbol{p}_1 \frac{\sin^4\left(\dfrac{\pi}{2}\boldsymbol{k} \cdot \boldsymbol{p}_1\right)}{(\boldsymbol{k} \cdot \boldsymbol{p}_1)^2} \\ & + \frac{nL^3}{(\ln\kappa)^2 8\pi^7} t \int \mathrm{d}\boldsymbol{p}_1 \int \frac{\mathrm{d}\boldsymbol{k}}{k^4} \left(\frac{1}{2\pi \mathrm{i}\boldsymbol{k} \cdot \boldsymbol{p}_1 \frac{U\tau}{L} + 1}\right) \left(\boldsymbol{I} - \frac{\boldsymbol{k}\boldsymbol{k}}{k^2}\right) : \boldsymbol{p}_1\boldsymbol{p}_1 \\ & \times \frac{\sin^4\left(\dfrac{\pi}{2}\boldsymbol{k} \cdot \boldsymbol{p}_1\right)}{(\boldsymbol{k} \cdot \boldsymbol{p}_1)^2}. \end{aligned} \tag{4.8}$$

In (4.8), the term of $O(U\tau/L)$ in the argument of the exponential may be neglected in the limit $U\tau/L \ll 1$, and this leads to a (dimensional) correlation time of $O(\tau)$. For

https://doi.org/10.1017/jfm.2020.827 Published online by Cambridge University Press

$U\tau/L \gg 1$, the integral in (4.8) has a dominant contribution for $k \sim L/(U\tau)$ and hence the dimensional correlation time is $O(L/U)$ (Kasyap *et al.* 2014). For times much shorter than the velocity correlation time, the tracer shows ballistic motion and the MSD simplifies to

$$\langle x^2(t)\rangle|_{uncorr} = \frac{nL^3}{(\ln\kappa)^2 16\pi^7} t^2 \int \mathrm{d}\boldsymbol{p}_1 \int \frac{\mathrm{d}\boldsymbol{k}}{k^4} \frac{\sin^4\left(\frac{\pi}{2}\boldsymbol{k}\cdot\boldsymbol{p}_1\right)}{(\boldsymbol{k}\cdot\boldsymbol{p}_1)^2} \left(\boldsymbol{I} - \frac{\boldsymbol{k}\boldsymbol{k}}{k^2}\right) : \boldsymbol{p}_1\boldsymbol{p}_1. \tag{4.9}$$

The coefficient of $\mathrm{O}(t^2)$ in (4.9) is the fluid velocity variance given in (3.7). On the other hand, for times much longer than the velocity correlation time, the tracer shows diffusive motion with $\langle x^2(t)\rangle|_{uncorr} = 6D_t|_{uncorr}t$, where the effective diffusivity is given by

$$D_t|_{uncorr} = \frac{nL^3}{(\ln\kappa)^2 48\pi^7} \int \mathrm{d}\boldsymbol{p}_1 \int \frac{\mathrm{d}\boldsymbol{k}}{k^4} \left(\frac{1}{2\pi\mathrm{i}\boldsymbol{k}\cdot\boldsymbol{p}_1 \dfrac{U\tau}{L} + 1}\right) \left(\boldsymbol{I} - \frac{\boldsymbol{k}\boldsymbol{k}}{k^2}\right) : \boldsymbol{p}_1\boldsymbol{p}_1 \frac{\sin^4\left(\frac{\pi}{2}\boldsymbol{k}\cdot\boldsymbol{p}_1\right)}{(\boldsymbol{k}\cdot\boldsymbol{p}_1)^2}. \tag{4.10}$$

The above expression may also be derived using the Green–Kubo formula (Balakrishnan 2008) and has also been obtained by Kasyap *et al.* (2014) using a different approach. On the other hand, to the best of our knowledge, the complete expression for the MSD in (4.8) has not been given in the literature even for non-interacting swimmers. As discussed earlier in § 3.1, the integrals in (4.8) may be numerically evaluated with the choice of a $\boldsymbol{k}$-aligned spherical coordinate system. Recall that the tracer diffusivity ($D_t|_{uncorr}$) in (4.10) is non-dimensionalised using $U^2\tau$ as the scale. For $U\tau/L \ll 1$, the integral in (4.10) is $O(1)$, and hence $D_t|_{uncorr} \sim nL^3/(\ln\kappa)^2U^2\tau$. For $U\tau/L \gg 1$, the dominant contribution results from $k \sim O(L/U\tau)$ and, using this scale, the integral in (4.10) is $O(L/U\tau)$, with the tracer diffusivity, $D_t|_{uncorr} \sim nL^3/(\ln\kappa)^2UL$ (Kasyap *et al.* 2014). Recall that these scalings were obtained earlier in § 2 using physical arguments.

4.2. *Suspensions of interacting swimmers*

For interacting swimmers, the Fourier-transformed velocity correlation function at $O(nL^3)^2$ is given by

$$\langle \hat{\boldsymbol{u}}(\boldsymbol{k}, t_1)\cdot\hat{\boldsymbol{u}}(-\boldsymbol{k}, t_2)\rangle|_{corr} = \int \hat{\boldsymbol{u}}(\boldsymbol{k})\cdot\hat{\boldsymbol{u}}(-\boldsymbol{k})\hat{G}_2\left(\boldsymbol{p}_1, \boldsymbol{p}_2, t_1|\boldsymbol{p}_1', \boldsymbol{p}_2', t_2; \boldsymbol{k}\right)\hat{\Omega}_2^{(1)}\left(\boldsymbol{k}, \boldsymbol{p}_1', \boldsymbol{p}_2'\right) \times \mathrm{d}\boldsymbol{p}_1\,\mathrm{d}\boldsymbol{p}_1'\,\mathrm{d}\boldsymbol{p}_2\,\mathrm{d}\boldsymbol{p}_2', \tag{4.11}$$

where $\hat{\Omega}_2^{(1)}$ is the pair-probability density derived in § 3.3 and $\hat{G}_2$ gives the Fourier-transformed transition probability of finding a pair of swimmers with orientations $\boldsymbol{p}_1$ and $\boldsymbol{p}_2$ at time t_1, given that the pair had orientations $\boldsymbol{p}_1'$ and $\boldsymbol{p}_2'$ at time t_2. The governing equation for $\hat{G}_2$ is

$$\frac{\mathrm{d}\hat{G}_2}{\mathrm{d}t} + 2\pi\mathrm{i}\left(\frac{U\tau}{L}\right)\boldsymbol{k}\cdot(\boldsymbol{p}_2 - \boldsymbol{p}_1)\hat{G}_2 + \left(2\hat{G}_2 - \frac{1}{4\pi}\int \mathrm{d}\boldsymbol{p}_1\hat{G}_2 - \frac{1}{4\pi}\int \mathrm{d}\boldsymbol{p}_2\hat{G}_2\right) = \boldsymbol{\delta}(\boldsymbol{p}_2 - \boldsymbol{p}_2')\boldsymbol{\delta}(\boldsymbol{p}_1 - \boldsymbol{p}_1')\delta(t - t'). \tag{4.12}$$

https://doi.org/10.1017/jfm.2020.827 Published online by Cambridge University Press

The inverse tumbling terms in (4.12) again don't contribute (see § 3.3), and the expression for $\hat{G}_2$ relevant to evaluating the velocity correlation function is given by

$$\hat{G}_2\left(\boldsymbol{p}_1, \boldsymbol{p}_2, t|\boldsymbol{p'}_1, \boldsymbol{p}'_2, 0; \boldsymbol{k}\right) = \delta(\boldsymbol{p}_1 - \boldsymbol{p}'_1)\delta(\boldsymbol{p}_2 - \boldsymbol{p}'_2)\exp\left(\left(-2\pi\mathrm{i}\boldsymbol{k}\cdot(\boldsymbol{p}_2 - \boldsymbol{p}_1)\frac{U\tau}{L} - 2\right)t\right). \tag{4.13}$$

Using this result and simplifying, we obtain the final expression for the MSD of a passive tracer at $O(nL^3)^2$ as

$$\begin{aligned}\langle x^2(t)\rangle|_{corr} = {} & \frac{1}{(\ln\kappa)^3 2\pi^6}\int \mathrm{d}\boldsymbol{p}_1 \int \mathrm{d}\boldsymbol{p}_2 \int \frac{\mathrm{d}\boldsymbol{k}}{k^4}\left(\frac{-1+\exp\left(\left(-2\pi\mathrm{i}\boldsymbol{k}\cdot(\boldsymbol{p}_2-\boldsymbol{p}_1)\frac{U\tau}{L}-2\right)t\right)}{\left(2\pi\mathrm{i}\boldsymbol{k}\cdot(\boldsymbol{p}_2-\boldsymbol{p}_1)\frac{U\tau}{L}+2\right)^2}\right) \\ & \times\left(\boldsymbol{I}-\frac{\boldsymbol{k}\boldsymbol{k}}{k^2}\right):\boldsymbol{p}_1\boldsymbol{p}_2\frac{\sin^2\left(\frac{\pi}{2}\boldsymbol{k}\cdot\boldsymbol{p}_1\right)}{(\boldsymbol{k}\cdot\boldsymbol{p}_1)}\frac{\sin^2\left(\frac{\pi}{2}\boldsymbol{k}\cdot\boldsymbol{p}_2\right)}{(\boldsymbol{k}\cdot\boldsymbol{p}_2)}\hat{\Omega}_2^{(1)}\left(\boldsymbol{p}_1,\boldsymbol{p}_2;\boldsymbol{k}\right) \\ & + \frac{1}{(\ln\kappa)^3 2\pi^6}t\int \mathrm{d}\boldsymbol{p}_1 \int \mathrm{d}\boldsymbol{p}_2 \int \frac{\mathrm{d}\boldsymbol{k}}{k^4}\left(\frac{1}{2\pi\mathrm{i}\boldsymbol{k}\cdot(\boldsymbol{p}_2-\boldsymbol{p}_1)\frac{U\tau}{L}+2}\right) \\ & \times\left(\boldsymbol{I}-\frac{\boldsymbol{k}\boldsymbol{k}}{k^2}\right):\boldsymbol{p}_1\boldsymbol{p}_2\frac{\sin^2\left(\frac{\pi}{2}\boldsymbol{k}\cdot\boldsymbol{p}_1\right)}{(\boldsymbol{k}\cdot\boldsymbol{p}_1)}\frac{\sin^2\left(\frac{\pi}{2}\boldsymbol{k}\cdot\boldsymbol{p}_2\right)}{(\boldsymbol{k}\cdot\boldsymbol{p}_2)}\hat{\Omega}_2^{(1)}\left(\boldsymbol{p}_1,\boldsymbol{p}_2;\boldsymbol{k}\right).\end{aligned} \tag{4.14}$$

The correlation time is now $O(\tau)$ irrespective of $U\tau/L$, since correlations between swimmers do not decay in the absence of tumbling. For times smaller than $O(\tau)$, the MSD simplifies to

$$\begin{aligned}\langle x^2(t)\rangle_{corr} = {} & \frac{t^2}{(\ln\kappa)^3 4\pi^6}\int \mathrm{d}\boldsymbol{p}_1 \int \mathrm{d}\boldsymbol{p}_2 \int \frac{\mathrm{d}\boldsymbol{k}}{k^4}\left(\boldsymbol{I}-\frac{\boldsymbol{k}\boldsymbol{k}}{k^2}\right):\boldsymbol{p}_1\boldsymbol{p}_2 \\ & \times\frac{\sin^2\left(\frac{\pi}{2}\boldsymbol{k}\cdot\boldsymbol{p}_1\right)}{(\boldsymbol{k}\cdot\boldsymbol{p}_1)}\frac{\sin^2\left(\frac{\pi}{2}\boldsymbol{k}\cdot\boldsymbol{p}_2\right)}{(\boldsymbol{k}\cdot\boldsymbol{p}_2)}\hat{\Omega}_2^{(1)}\left(\boldsymbol{k},\boldsymbol{p}_1,\boldsymbol{p}_2\right).\end{aligned} \tag{4.15}$$

The coefficient of t^2 is now the correlated component of the velocity variance given in (3.28). On the other hand, for times much longer than the velocity correlation time, the tracer shows diffusive motion with $\langle x^2(t)\rangle|_{corr} = 6D_t|_{corr}t$ for any finite swimmer run length ($U\tau/L$). The effective diffusivity is given by

$$\begin{aligned}D_t|_{corr} = {} & \frac{1}{(\ln\kappa)^3 12\pi^6}\int \mathrm{d}\boldsymbol{p}_1 \int \mathrm{d}\boldsymbol{p}_2 \int \frac{\mathrm{d}\boldsymbol{k}}{k^4}\left(\frac{1}{2\pi\mathrm{i}\boldsymbol{k}\cdot(\boldsymbol{p}_2-\boldsymbol{p}_1)\frac{U\tau}{L}+2}\right)\left(\boldsymbol{I}-\frac{\boldsymbol{k}\boldsymbol{k}}{k^2}\right):\boldsymbol{p}_1\boldsymbol{p}_2 \\ & \times\frac{\sin^2\left(\frac{\pi}{2}\boldsymbol{k}\cdot\boldsymbol{p}_1\right)}{(\boldsymbol{k}\cdot\boldsymbol{p}_1)}\frac{\sin^2\left(\frac{\pi}{2}\boldsymbol{k}\cdot\boldsymbol{p}_2\right)}{(\boldsymbol{k}\cdot\boldsymbol{p}_2)}\hat{\Omega}_2^{(1)}\left(\boldsymbol{k},\boldsymbol{p}_1,\boldsymbol{p}_2\right).\end{aligned} \tag{4.16}$$

The integrals in (4.14) and (4.16) are again evaluated numerically (see § 3.1 for the coordinate system used). Recall that the tracer diffusivity ($D_t|_{corr}$) in (4.10) is also

https://doi.org/10.1017/jfm.2020.827 Published online by Cambridge University Press

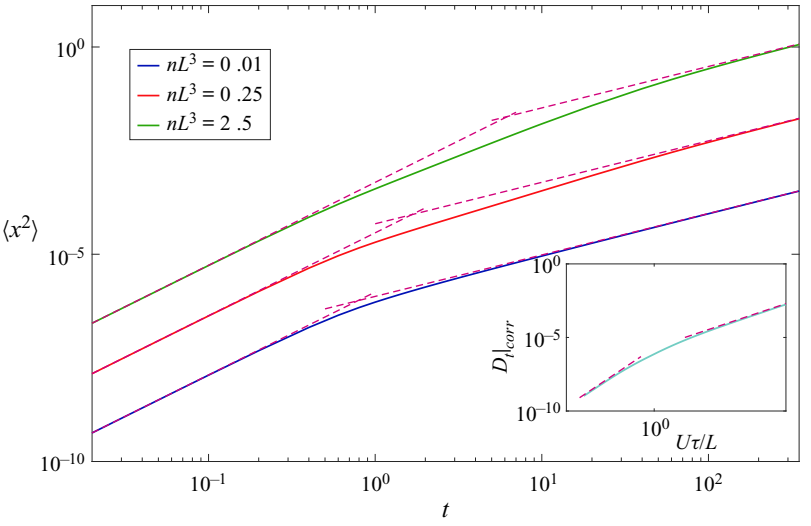


FIGURE 11. The evolution of the MSD of the passive tracer, in a suspension of pushers, with time for $U\tau/L = 50$ and $\kappa = 8$ for varying nL^3. The inset shows the correlated tracer diffusivity $(D_t|_{corr})$ at $O(nL^3)^2$ as a function of the run length, $U\tau/L$, for $\kappa = 8$; the dashed lines show the asymptotic scalings discussed in the text.

non-dimensionalised using $U^2\tau$ as the scale. For $U\tau/L \ll 1$, the integral in (4.16) is seen to be $O(nL^3)^2(U\tau/L)$, and hence $D_t|_{corr} \sim (nL^3)^2/(\ln\kappa)^3 U^2\tau(U\tau/L)$. However, for $U\tau/L \gg 1$ the integral in (4.16) is $\mathrm{O}(nL^3)^2$, and hence $D_t|_{corr} \sim (nL^3)^2/(\ln\kappa)^3 U^2\tau$. The scaling was earlier obtained in § 2 using physical arguments.

4.3. *Effective tracer MSD*

The total MSD of the tracer, to $O(nL^3)^2$, is obtained by combining the expressions in (4.8) and (4.14), and is plotted in figure 11, as a function of nL^3, for a suspension of pushers. Figure 11 shows that the time taken to transition from the ballistic to the diffusive regime increases with increasing volume-fraction of the swimmers. This surprising behaviour can be explained by noting the differing time scales for the decay of the velocity correlations at $O(nL^3)$ and $O(nL^3)^2$. At $O(nL^3)$, this time scale (t_c) is set by the swimmer–tracer interaction time. For rapid tumblers $(U\tau/L \ll 1)$, the interaction is cut off by the decorrelation of the swimmer orientation, implying $t_c \sim O(\tau)$. On the other hand for persistent swimmers $(U\tau/L \gg 1)$, the distance that the tracer is convected asymptotes to a finite value for tracer–swimmer separations greater than $O(L)$, and thus $t_c \sim O(L/U)$. At $O(nL^3)^2$, the decay of the velocity correlations, irrespective of $U\tau/L$, only occurs due to orientation decorrelation of the swimmers on the time scale τ. As a result for nL^3 of order unity, the transition time between the ballistic and diffusive regimes diverges as $U\tau/L$. The resulting broad crossover gives the impression of an nL^3-dependent anomalous exponent in the interval $L/U \ll t \ll \tau$ (see the curve for $nL^3 = 2.5$ in figure 11). For rapid tumblers $(U\tau/L \ll 1)$, the transition time is $O(\tau)$ regardless of nL^3, and there is no intermediate anomalous scaling.

The inset of figure 11 shows the $O(nL^3)^2$ correlated contribution to the tracer diffusivity $(D_t|_{corr})$. In the straight-swimmer limit, $D_t|_{corr}$ diverges linearly in $U\tau/L$. This scaling may be rationalized by starting from $D_t \sim U_t^2 t_c$ where U_t is the scale of the velocity

https://doi.org/10.1017/jfm.2020.827 Published online by Cambridge University Press

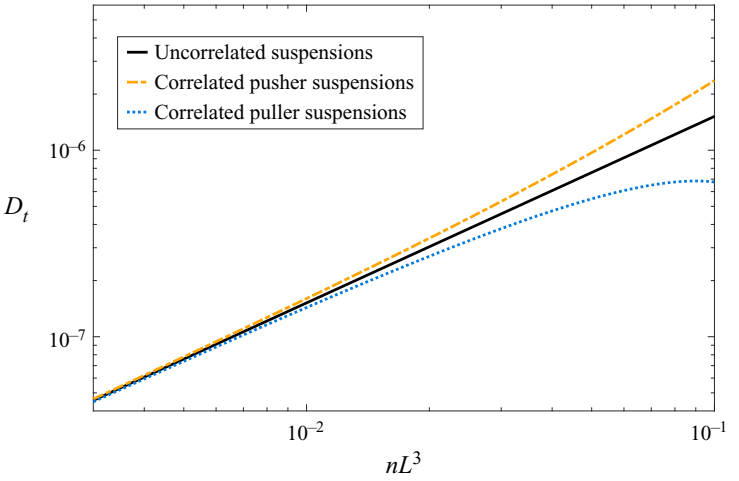


FIGURE 12. The variation of the diffusivity of a passive tracer versus the volume fraction of swimmers (nL^3) for a fixed run length, $U\tau/L = 50$, and aspect-ratio $\kappa = 8$.

convecting the tracer and t_c is the time scale of decay of the velocity correlations. Here, U_t is $O(U/\ln\kappa)$ regardless of the swimmer volume-fraction (nL^3), while the t_c scaling is discussed above. The resulting scaling for tracer diffusivity in an interacting suspension, to $O(nL^3)^2$, is therefore given by

$$\frac{nL^3U^2\tau}{(\ln\kappa)^2}\left(\widetilde{d}_1 + \frac{nL^3}{\ln\kappa}\frac{U\tau}{L}\widetilde{d}_2\right) \quad \text{for } U\tau/L \ll 1 \tag{4.17}$$

and

$$\frac{nL^4U}{(\ln\kappa)^2}\left(d_1 + \frac{nL^3}{\ln\kappa}\frac{U\tau}{L}d_2\right) \quad \text{for } U\tau/L \gg 1, \tag{4.18}$$

and confirms the scalings shown in figure 11 (inset) at $O(nL^3)^2$. The tracer diffusivity variation with volume fraction also shows a pusher–puller bifurcation similar to the velocity variance as shown in figure 12. Importantly, we see that correlations significantly enhance the tracer diffusivity in a pusher suspension; figure 12 already shows an enhancement of 55.51% at $nL^3 = 0.1$ for a swimmer with the run length, $U\tau/L = 50$. Thus, the enhancement for the tracer diffusivity due to correlations is much more pronounced than that for the velocity variance discussed earlier in § 3.3.

Several experiments probing bacterial suspension dynamics with passive tracers have reported an intermediate super-diffusive regime and a volume fraction dependent crossover time (Wu & Libchaber 2000; Kim & Breuer 2004; Chen *et al.* 2007; Valeriani *et al.* 2011; Argun *et al.* 2016; Patteson *et al.* 2016; Peng *et al.* 2016). To the best of our knowledge, this is the first theoretical explanation for these observations. Our analysis thus shows that in a bath of interacting persistent swimmers ($U\tau/L \gg 1$), the temporal and spatial correlations of the (effective) noise experienced by the passive tracer increase to $O(\tau)$ and $O(U\tau)$, respectively. The simplistic approximation for the active noise often found in the literature is thus seen to be insufficient (Maggi *et al.* 2014; Argun *et al.* 2016; Kanazawa *et al.* 2019). Further, when confined by a harmonic potential with a trap radius of $O(U\tau)$, the probability distribution of the tracer displacements is thus expected to become pronouncedly non-Gaussian with increasing nL^3. This has indeed been seen in experiments (Argun *et al.* 2016; Krishnamurthy *et al.* 2016).

https://doi.org/10.1017/jfm.2020.827 Published online by Cambridge University Press

5. Conclusion

In this paper, we have shown that long-ranged pair-correlations lead to divergent velocity fluctuations and tracer diffusivities in straight-swimmer suspensions. For suspensions of RTPs, this divergence is replaced by a logarithmic increase of the velocity variance as shown in figure 4, and a linear increase of the tracer diffusivity as highlighted in figure 11, with the run length for $U\tau/L \gg 1$ (see (3.27) and (3.28), respectively, for the correlated covariance and variance expressions and (4.16) for the correlated tracer diffusivity). Pair-correlations are also crucially dependent on the swimming mechanism (pusher *vis-á-vis* puller), and lead to larger velocity variance and tracer diffusivities in suspensions of pushers (see figures 6 and 12). Thus, in contrast to recent work emphasizing the role of anisotropic tracers (Peng *et al.* 2016; Yang *et al.* 2016), spherical tracers already discriminate between pusher and puller suspensions on account of hydrodynamically induced correlations.

While our detailed analysis is limited to slender swimmers, the scaling arguments presented in § 2 only involve far-field hydrodynamics. It is thus expected that the arguments would be applicable to suspensions of anisotropic swimmers (Toppaladoddi & Balmforth 2014; Kyoya *et al.* 2015) in general (not necessarily slender), provided far-field interactions dominate over near-field ones. The relative importance of the near-field *vis-á-vis* far-field interactions for general swimmers is not obvious, however. As argued in § 2, an $O(1/r^2)$ pair-orientation correlation arises from the cumulative (weak) rotation, of the same order, arising from the integrated effect of the far-field $O(1/r^3)$ velocity gradient along a swimming trajectory that reaches the given point (at a distance r from the test swimmer), with the pair-separation at all points along this trajectory being much larger than the swimmer size. Interestingly, a correlation of the same order may be induced by a near-field interaction where the induced rotation is of order unity, and the smallness of the correlation arises instead from the small $O(1/r^2)$ collision cross-section corresponding to the rarity of near-field interactions. Although the nature of the correlations induced by the near- and far-field interactions is expected to be quite different in general, the $O(1/r^2)$ decay of pair-probability density suggests that a logarithmic growth of the velocity variance arises regardless of which of these interactions dominate (and, thence, of the shape of the swimmers, provided they are non-spherical); although, on account of the contribution of near-field interactions of a comparable magnitude, the prefactor involved in the aforementioned $O(1/r^2)$ pair-probability density cannot be predicted in closed form for non-slender swimmers. The robustness of the logarithmic divergence in suspensions of non-slender straight-swimmers is perhaps evidenced by the logarithmic scaling for the velocity variance in simulations of regularized point dipoles by Underhill & Graham (2011). In light of the logarithmic scaling that is expected to arise in any dilute suspension of non-spherical squirmers, the spherical squirmer model often used in studies of active suspensions may therefore represent an exceptional scenario and the results obtained need to be extrapolated with care (Ishikawa, Simmonds & Pedley 2006; Ishikawa & Pedley 2007*b*, 2008; Mehandia & Nott 2008; Alarcón & Pagonabarraga 2013; Delmotte *et al.* 2018).

For the slender (bacterial) swimmers analysed in this paper, as explained at the start of § 2, the swimming speed and the disturbance velocity field arise due to a common underlying propulsive mechanism and, therefore, cannot be varied independently. However, theoretically speaking, one may treat these two facets as independent degrees of freedom; the latter is indeed the case for the Lighthill–Blake spherical squirmer model (Blake 1971; Pedley 2016). For such a squirmer, the tangential slip velocity at the surface

https://doi.org/10.1017/jfm.2020.827 Published online by Cambridge University Press

($\boldsymbol{u}_s$) is of the following general form:

$$\boldsymbol{u}_s = \sum_{n=1}^{2} \frac{2}{n(n+1)} B_n \left(\frac{\boldsymbol{p}\cdot\boldsymbol{r}}{r}\frac{\boldsymbol{r}}{r} - \boldsymbol{p} \right) P_n' \left(\frac{\boldsymbol{p}\cdot\boldsymbol{r}}{r} \right), \tag{5.1}$$

where $\boldsymbol{p}$ is the orientation vector, $\boldsymbol{r}$ is the position vector and P_n is the nth Legendre polynomial (Blake 1971; Ishikawa & Pedley 2007*a*). In the most commonly used version of this model, only the modes proportional to B_1 and B_2, in (5.1), are accounted for. Such a squirmer swims with a speed $2B_1/3$, while the disturbance velocity in the far-field has a dipolar character with amplitude B_2 (see, for instance, Ishikawa & Pedley (2007*a*)). There also exist ellipsoidal generalizations of the squirmer model, with an expansion similar to (5.1) for the slip velocity (Toppaladoddi & Balmforth 2014; Kyoya *et al.* 2015; Felderhof 2016; Poehnl, Popescu & Uspal 2020).

In light of the use of the ellipsoidal squirmer models above, it is of interest to derive scaling estimates for the tracer diffusivity when the dipole disturbance field and swimming speed may be assumed independent. The corresponding scales are denoted as U_d and U_s; for the Lighthill–Blake model above, $U_s \propto B_1$ while $U_d \propto B_2$. Since we are interested in distinguishing between these two effects, we confine the scaling arguments to persistent swimmers such that $U_s\tau/L \gg 1$. Recall from § 2 that the tracer diffusivity scaling, in the Eulerian approximation, is given by $D_t \sim \langle u^2\rangle t_c$ where t_c is the correlation time. Using $\langle u^2\rangle \sim \mathrm{O}\ (U_t^2)$, where U_t is the magnitude of the velocity by which the tracer is convected, we finally get $D_t \sim (U_t)^2 t_c$. Now, $U_t \sim U_d$, but the time scale of tracer–swimmer interaction is set by the swim speed for persistent swimmers and, hence, $t_c \sim L/U_s$. Thus, at $O(nL^3)$, the tracer diffusivity scaling is

$$D_t|_{uncorr} \sim (nL^3)(U_d L)\frac{U_d}{U_s}. \tag{5.2}$$

Thus we see that, even for non-interacting swimmers, the tracer diffusivity reduces when increasing the swim speed (U_s) for a constant dipole strength (U_d). Using $U_d = U/\ln\kappa$ and $U_s = U$ in (5.2), we recover the scaling given earlier for slender swimmers in (4.18). The scaling in (5.2) is an Eulerian estimate, which is rigorously valid in the limit $U_d \ll U_s$. In this limit, the tracer is only negligibly displaced in each swimmer–tracer interaction and hence a reduction in the diffusivity is expected when increasing the swim speed relative to the dipole strength. Note that (5.2) cannot be used to estimate the tracer diffusivity if $U_d > U_s$. Next, using the fact that the correlations scale as $U_d\tau/L$, we obtain the following scaling for the tracer diffusivity at $O(nL^3)^2$:

$$D_t|_{corr} \sim (nL^3)^2(U_d L)\frac{U_d}{U_s}\frac{U_d\tau}{L}. \tag{5.3}$$

Thus, increasing swimming speed for a constant disturbance velocity field again reduces the tracer diffusivity for the same reason as that for uncorrelated swimmers.

To conclude, in this paper, we have examined correlations due to direct pairwise hydrodynamic interactions between swimmers, while not accounting for those induced (indirectly) by long-wavelength fluctuations in the suspension velocity and orientation fields. It is well known that these fluctuations lead to an instability of a suspension of pushers (manifesting as bacterial turbulence in experiments, as discussed in the introduction), in turn implying diverging contributions of the 'collective effects' to statistical correlations at the threshold (Subramanian & Koch 2009; Krishnamurthy &

https://doi.org/10.1017/jfm.2020.827 Published online by Cambridge University Press

Subramanian 2015; Stenhammar *et al.* 2017; Qian *et al.* 2017; Bárdfalvy *et al.* 2019). This divergence is distinct from the one described here. Nevertheless, the framework needed for this calculation requires the $U\tau/L$-dependent pair-probability, determined here, as an input, and will be reported in future work. Our work thus lays a rigorous foundation for understanding hydrodynamic interactions between anisotropic swimmers and their role in bacterial turbulence (Wensink *et al.* 2012).

Declaration of interests

The authors report no conflict of interest.

Appendix A. Rotation rates of slender swimmers

Herein, we derive the expression for the rates of rotation $\dot{\boldsymbol{p}}_{ij}$ for a pair of interacting slender swimmers. One can define the rate of rotation of swimmer 1 due to swimmer 2 as $\dot{\boldsymbol{p}}_{12} = \boldsymbol{\omega}_1 \wedge \boldsymbol{p}_1$, with $\boldsymbol{\omega}_1$ representing its angular velocity. The velocity at any point s on a rigid slender body may be written as $\boldsymbol{u}_1^s(s\boldsymbol{p}_1) = \boldsymbol{u}_1^T + \boldsymbol{\omega}_1 \wedge \boldsymbol{p}_1 s$, where $\boldsymbol{u}_1^T$ is the translational velocity of the geometric centre ($s = 0$). From viscous slender-body theory (Batchelor 1970; Kim & Karrila 1991), one has the relation $\boldsymbol{u}_1^s(s\boldsymbol{p}_1) - \boldsymbol{u}^\infty(s\boldsymbol{p}_1) = (\ln\kappa/\eta) f(s)\boldsymbol{p}_1 \cdot (\boldsymbol{I} + \boldsymbol{p}_1\boldsymbol{p}_1)$ to leading logarithmic order. Here, $\boldsymbol{u}^\infty$ is the ambient field which in the present problem is the velocity field generated by the swimmer 2, that is, $\boldsymbol{u}^\infty \equiv \boldsymbol{u}_2$; the force density $f(s) = \eta U\,\mathrm{sgn}(s)/\ln\kappa$. To determine, $\boldsymbol{u}_2$, one solves the Stokes equations (3.1*a*) at any location $(-\boldsymbol{r} + s\boldsymbol{p}_1)$ along swimmer 1; that is

$$-\boldsymbol{\nabla} P_2 + \eta \nabla_r^2 \boldsymbol{u}_2(-\boldsymbol{r} + s\boldsymbol{p}_1) = \int_{-L/2}^{L/2} \mathrm{d}s' f(s') \boldsymbol{\delta}(-\boldsymbol{r} + s\boldsymbol{p}_1 - s'\boldsymbol{p}_2)\boldsymbol{p}_2. \tag{A 1}$$

Again, it is convenient to solve (A 1) in Fourier space, and the Fourier-transformed ambient field along the length of swimmer 1, $\hat{u}_2(\boldsymbol{k})$, can be written as

$$\hat{\boldsymbol{u}}_2(\boldsymbol{k}) = -\frac{\mathrm{i}}{2\pi^3 k^2}\,[\boldsymbol{I} - \boldsymbol{k}\boldsymbol{k}] \cdot \boldsymbol{p}_2 \exp(-2\pi \mathrm{i} s \boldsymbol{k} \cdot \boldsymbol{p}_1) \frac{1}{(\boldsymbol{k} \cdot \boldsymbol{p}_2)} \sin^2\left(\frac{\pi}{2}\boldsymbol{k} \cdot \boldsymbol{p}_2\right), \tag{A 2}$$

on applying the non-dimensionalizations stated below (3.6). The force-free condition ensures that the swimmer propagates with the sum of the swimming and disturbance velocities averaged over its length. However, given that the latter is $O(\ln\kappa)^{-1}$ smaller, it may be neglected. Applying the torque-free condition, $\int_{-1}^{1} s\boldsymbol{p}_1 \wedge [\boldsymbol{u}_1^s(s\boldsymbol{p}_1) - \boldsymbol{u}_2(s\boldsymbol{p}_1)]\,\mathrm{d}s = 0$, results in the following expression for $\hat{\dot{\boldsymbol{p}}}_{12}$:

$$\hat{\dot{\boldsymbol{p}}}_{12} = -\frac{3}{\pi^3 k^2} \frac{1}{(\boldsymbol{k} \cdot \boldsymbol{p}_2)} \sin^2\left(\frac{\pi}{2}\boldsymbol{k} \cdot \boldsymbol{p}_2\right) j_1(\pi \boldsymbol{k} \cdot \boldsymbol{p}_1) \left\{\left[\boldsymbol{p}_1 \wedge (\boldsymbol{I} - \hat{\boldsymbol{k}}\hat{\boldsymbol{k}}) \cdot \boldsymbol{p}_2\right] \wedge \boldsymbol{p}_1\right\}, \tag{A 3}$$

where $j_1(x) = \sin(z)/z^2 - \cos(z)/z$ is the spherical Bessel function of the first kind (Gradshteyn & Ryzhik 1980). The Fourier-transformed rate of rotation of the second swimmer $\hat{\dot{\boldsymbol{p}}}_{21}$ is given by interchanging the indices 1 and 2 in (A 3). Note that the corresponding expression for the Fourier-transformed rotation rate of point force-dipole swimmers (in which case the swimmer length $L \to 0$) is derivable from (A 3) by extracting the $k \to 0$ limit (or in dimensional terms $kL \to 0$). Upon approximating $\sin(\pi \boldsymbol{k} \cdot \boldsymbol{p}_2/2) \approx$

https://doi.org/10.1017/jfm.2020.827 Published online by Cambridge University Press

$\pi \boldsymbol{k}\cdot\boldsymbol{p}_2/2$ and $j_1(\pi \boldsymbol{k}\cdot\boldsymbol{p}_1)\approx \pi \boldsymbol{k}\cdot\boldsymbol{p}_1/3$, we get

$$\hat{\hat{\boldsymbol{p}}}_{12}|_{dp} = -\frac{1}{4}(\hat{\boldsymbol{k}}\cdot\boldsymbol{p}_2)(\hat{\boldsymbol{k}}\cdot\boldsymbol{p}_1)\left\{\left[\boldsymbol{p}_1\wedge(\boldsymbol{I}-\hat{\boldsymbol{k}}\hat{\boldsymbol{k}})\cdot\boldsymbol{p}_2\right]\wedge\boldsymbol{p}_1\right\}, \tag{A 4}$$

where the subscript on the left-hand side indicates point force-dipoles.

Appendix B. Recovering the straight-swimmer pair-probability density from the analysis of RTPs

One may recover the straight-swimmer limiting case, obtained in § 3.2, from (3.26), in the limit of large $U\tau/L$. To see this, we first rewrite (3.26) as

$$\hat{\Omega}_2^{(1)} = -\frac{3(nL^3)^2}{32\pi^6k^3}\left(\frac{\mathrm{i}}{\hat{\boldsymbol{k}}\cdot(\boldsymbol{p}_2-\boldsymbol{p}_1)-\mathrm{i}\vartheta}\right)\left(\boldsymbol{I}-\hat{\boldsymbol{k}}\hat{\boldsymbol{k}}\right):\boldsymbol{p}_2\boldsymbol{p}_1 \times\left[\frac{1}{(\boldsymbol{k}\cdot\boldsymbol{p}_1)}\sin^2\left(\frac{\pi}{2}\boldsymbol{k}\cdot\boldsymbol{p}_1\right)\sin\left(\pi\boldsymbol{k}\cdot\boldsymbol{p}_2\right)+\frac{1}{(\boldsymbol{k}\cdot\boldsymbol{p}_2)}\sin^2\left(\frac{\pi}{2}\boldsymbol{k}\cdot\boldsymbol{p}_2\right)\sin\left(\pi\boldsymbol{k}\cdot\boldsymbol{p}_1\right)\right], \tag{B 1}$$

where $\vartheta = L/(\pi k U\tau)$. In the limit $U\tau/L\gg 1$, or equivalently, $\vartheta\ll 1$, implying that $i\vartheta\to 0$. Interpreting the bracketed term on the right-hand side of (B 1), in this limit, needs careful consideration. Naïvely setting $\vartheta=0$ only leads to the particular solution corresponding to the straight-swimmer pair-probability density, as given in (3.19). To obtain the correct answer in the straight-swimmer limiting form of $\hat{\Omega}_2^{(1)}$, one needs to apply the Plemelj–Sokhotski formula (Gakhov 1966; Fokas & Ablowitz 2012), which may be written as $\lim_{\epsilon\to 0} 1/(x-\mathrm{i}\epsilon) = -\delta(x)+PV[1/x]$, and this yields

$$\hat{\Omega}_2^{(1)}|_{st} = \frac{3(nL^3)^2}{32\pi^6k^3}\left(\delta(\hat{\boldsymbol{k}}\cdot(\boldsymbol{p}_2-\boldsymbol{p}_1))-PV\left[\frac{\mathrm{i}}{\hat{\boldsymbol{k}}\cdot(\boldsymbol{p}_2-\boldsymbol{p}_1)}\right]\right)\left(\boldsymbol{I}-\hat{\boldsymbol{k}}\hat{\boldsymbol{k}}\right):\boldsymbol{p}_2\boldsymbol{p}_1 \times\left[\frac{1}{(\boldsymbol{k}\cdot\boldsymbol{p}_1)}\sin^2\left(\frac{\pi}{2}\boldsymbol{k}\cdot\boldsymbol{p}_1\right)\sin\left(\pi\boldsymbol{k}\cdot\boldsymbol{p}_2\right)+\frac{1}{(\boldsymbol{k}\cdot\boldsymbol{p}_2)}\sin^2\left(\frac{\pi}{2}\boldsymbol{k}\cdot\boldsymbol{p}_2\right)\sin\left(\pi\boldsymbol{k}\cdot\boldsymbol{p}_1\right)\right]. \tag{B 2}$$

One may now readily note that the term involving $\delta(\hat{\boldsymbol{k}}\cdot(\boldsymbol{p}_2-\boldsymbol{p}_1))$ in (B 2) constitutes the homogeneous solution, whereas, the term involving $PV[\cdot]$ is the particular solution of the straight-swimmer pair-probability density given by (3.19).

Appendix C. Suspensions of interacting RTPs – large $U\tau/L$ covariance using matched asymptotic expansions

Based on the arguments presented in § 3.3, one may partition the original covariance integral in (3.10) into inner and outer contributions, to arrive at an asymptotic expression

https://doi.org/10.1017/jfm.2020.827 Published online by Cambridge University Press

for large $U\tau/L$ in the following manner:

$$\langle \boldsymbol{u}(\boldsymbol{x})\cdot\boldsymbol{u}(\boldsymbol{x}+\boldsymbol{r})\rangle|_{corr} = \frac{2}{r_1}\int_0^{(U\tau/L)^{\epsilon}} \mathrm{d}k_1 \sin(2\pi k_1 r_1)\zeta_{dpT}(\boldsymbol{k}_1,\boldsymbol{p}_1,\boldsymbol{p}_2) + \frac{2}{r}\int_{(U\tau/L)^{(\epsilon-1)}}^{\infty} \mathrm{d}k \sin(2\pi k r)\zeta_{SS}(\boldsymbol{k},\boldsymbol{p}_1,\boldsymbol{p}_2), \tag{C 1}$$

where we have introduced a parameter $\epsilon \in (0,1)$ (Subramanian & Brady 2006). In (C 1), the subscripts *SS* and *dpT* denote slender straight-swimmers and tumbling force-dipole swimmers; here, $\zeta_{SS}(\boldsymbol{k},\boldsymbol{p}_1,\boldsymbol{p}_2)$ and $\zeta_{dpT}(\boldsymbol{k}_1,\boldsymbol{p}_1,\boldsymbol{p}_2)$, respectively, represent the factors multiplying $\boldsymbol{\delta}(\boldsymbol{k}+\boldsymbol{k}')$ in (3.10) and (C 3) (see below). Note that, in terms of the wavenumber k, the inner and outer regions above correspond to kL and $kU\tau$, respectively, being $O(1)$, and this differing non-dimensionalzation is accounted for in (C 1). Thus, in the second integral, the scalings are the same as before, with r being the radial distance scaled by L; on the other hand, in the first integral $r_1 = rL/(U\tau)$.

Now, the point force-dipole, used for modelling the swimmers in the intermediate and outer regions, has velocity disturbance and pressure fields that satisfy the following equations:

$$-\boldsymbol{\nabla}P_i + \eta\nabla^2\boldsymbol{u}_i(\boldsymbol{x}-\boldsymbol{x}_i) = D\boldsymbol{p}_i\boldsymbol{p}_i : \boldsymbol{\nabla}_x\boldsymbol{\delta}(\boldsymbol{x}-\boldsymbol{x}_i), \tag{C 2a}$$

$$\boldsymbol{\nabla}\cdot\boldsymbol{u}_i = 0, \tag{C 2b}$$

where $D = 1/(4\ln\kappa)$ is the non-dimensional dipole strength and $\boldsymbol{p}_i$ denotes the orientation of the ith dipole swimmer. The Fourier-transformed velocity covariance for interacting point force-dipoles is then expressible as

$$\langle\hat{\boldsymbol{u}}(\boldsymbol{k})\cdot\hat{\boldsymbol{u}}(\boldsymbol{k}')\rangle|^{dp}_{corr} = \frac{D^2}{4\pi^2(\ln\kappa)k^4}\delta(\boldsymbol{k}+\boldsymbol{k}')\int \mathrm{d}\boldsymbol{p}_1\,\mathrm{d}\boldsymbol{p}_2(\boldsymbol{k}\cdot\boldsymbol{p}_1)(\boldsymbol{k}\cdot\boldsymbol{p}_2)(\boldsymbol{I}-\hat{\boldsymbol{k}}\hat{\boldsymbol{k}}) : \boldsymbol{p}_1\boldsymbol{p}_2\hat{\Omega}^{(1)}_{2\,dp}. \tag{C 3}$$

where $\hat{\Omega}^{(1)}_{2\,dp}$ denotes the Fourier-transformed pair-probability density, and the subscript *dp* denotes dipoles. The use of the Fourier-transformed point-dipole fields obtained from (C 2*a*), along with the procedure outlined in § 3.3, leads to the following simplified expression for $\hat{\Omega}^{(1)}_{2\,dp}$ in the outer region:

$$\hat{\Omega}^{(1)}_{2\,dp} = \frac{3D(nL^3)^2}{16\pi^2}\left(\frac{1}{1+\pi\mathrm{i}\dfrac{U\tau}{L}\boldsymbol{k}\cdot(\boldsymbol{p}_2-\boldsymbol{p}_1)}\right)(\boldsymbol{I}-\hat{\boldsymbol{k}}\hat{\boldsymbol{k}}) : \boldsymbol{p}_1\boldsymbol{p}_2(\boldsymbol{k}\cdot\boldsymbol{p}_1)(\boldsymbol{k}\cdot\boldsymbol{p}_2), \tag{C 4}$$

On naïvely applying the limit $U\tau/L \to \infty$ in (C 1), one encounters divergent integrals. This is because ζ_{dpT} diverges for $k_1 \to \infty$ (point dipoles exhibit a divergence as $r_1 \to 0$), while ζ_{SS} diverges for $k \to 0$ (the logarithmic divergence of straight-swimmers as $r \to \infty$). Subtracting the straight-swimming point force dipole contribution (corresponding to the contribution of the overlap region described above) from the respective integrands can,

https://doi.org/10.1017/jfm.2020.827 Published online by Cambridge University Press

however, account for the said divergences. Therefore one can recast (C 1) as

$$\begin{aligned}\langle \boldsymbol{u}(\boldsymbol{x})\cdot\boldsymbol{u}(\boldsymbol{x}+\boldsymbol{r})\rangle|_{corr} = {}& \frac{2}{r_1}\int_0^{(U\tau/L)^{\epsilon}} \mathrm{d}k_1 \sin(2\pi k_1 r_1)\left[\zeta_{dpT}(\boldsymbol{k}_1,\boldsymbol{p}_1,\boldsymbol{p}_2)\right.\\ & \left.-H(k_1-L_o)\zeta_{dpS}(\boldsymbol{k}_1,\boldsymbol{p}_1,\boldsymbol{p}_2)\right]\\ & +\frac{2}{r}\int_{(U\tau/L)^{(\epsilon-1)}}^{\infty} \mathrm{d}k \sin(2\pi k r)\left[\zeta_{SS}(\boldsymbol{k},\boldsymbol{p}_1,\boldsymbol{p}_2)\right.\\ & \left.-H(k-U_p)\zeta_{dpS}(\boldsymbol{k},\boldsymbol{p}_1,\boldsymbol{p}_2)\right]\\ & +\frac{2}{r_1}\int_0^{(U\tau/L)^{\epsilon}} \mathrm{d}k_1 \sin(2\pi k_1 r_1)H(k_1-L_o)\zeta_{dpS}(\boldsymbol{k}_1,\boldsymbol{p}_1,\boldsymbol{p}_2)\\ & +\frac{2}{r}\int_{(U\tau/L)^{(\epsilon-1)}}^{\infty} \mathrm{d}k \sin(2\pi k r)H(k-U_p)\zeta_{dpS}(\boldsymbol{k},\boldsymbol{p}_1,\boldsymbol{p}_2), \end{aligned} \tag{C 5}$$

such that the divergent contributions are now contained in the final two terms on the right-hand side of (C 5). Here, the subscript *dpS* denotes straight-swimming point force-dipoles. Now, the added integral terms are divergent both as $k\to 0$ and as $k\to\infty$, and the Heaviside functions $H(x)$ included in (C 5) ensure that these added terms solely account for the divergences already present (in the limit $U\tau/L\to\infty$) in (C 5). Note that both $\zeta_{dpS}(\boldsymbol{k},\boldsymbol{p}_1,\boldsymbol{p}_2)$ and $\zeta_{dpT}(\boldsymbol{k},\boldsymbol{p}_1,\boldsymbol{p}_2)$ have a common form as $U\tau/L\to\infty$. To see this one may use the Plemelj–Sokhotski formula on the pair-probability density appearing in ζ_{dpT}, as explained in appendix B for slender swimmers. Alternatively, one can determine the pair-probability in ζ_{dpS} following the method outlined in § 3.2, which gives:

$$\begin{aligned}\hat{\Omega}^{(1)}_{2dpS} = {}& \frac{3D(nL^3)^2}{64\pi^2}\left[\frac{|\boldsymbol{p}_2-\boldsymbol{p}_1|^2}{\left(\boldsymbol{k}\wedge(\boldsymbol{p}_2-\boldsymbol{p}_1)\right)\cdot\left(\boldsymbol{k}\wedge(\boldsymbol{p}_2-\boldsymbol{p}_1)\right)}\right]\left(\boldsymbol{k}\cdot(\boldsymbol{p}_1+\boldsymbol{p}_2)\right)^2\\ & \times\left[\boldsymbol{p}_2\cdot\boldsymbol{p}_1-\frac{\left(\boldsymbol{k}\cdot(\boldsymbol{p}_1+\boldsymbol{p}_2)\right)^2|\boldsymbol{p}_2-\boldsymbol{p}_1|^2}{4\left(\boldsymbol{k}\wedge(\boldsymbol{p}_2-\boldsymbol{p}_1)\right)\cdot\left(\boldsymbol{k}\wedge(\boldsymbol{p}_2-\boldsymbol{p}_1)\right)}\right]\delta\left[\boldsymbol{k}\cdot(\boldsymbol{p}_2-\boldsymbol{p}_1)\right]\\ & -\frac{3Di(nL^3)^2}{16\pi^3k^2\boldsymbol{k}\cdot(\boldsymbol{p}_2-\boldsymbol{p}_1)}\left(\boldsymbol{I}-\hat{\boldsymbol{k}}\hat{\boldsymbol{k}}\right):\boldsymbol{p}_2\boldsymbol{p}_1(\boldsymbol{k}\cdot\boldsymbol{p}_1)(\boldsymbol{k}\cdot\boldsymbol{p}_2). \end{aligned} \tag{C 6}$$

The 'difference integrals' in (C 5) that involve the Heaviside functions are now convergent and, therefore, we set $(U\tau/L)^{\epsilon}=\infty$ and $(U\tau/L)^{(\epsilon-1)}=0$ in (C 5) to get

$$\begin{aligned}\langle \boldsymbol{u}(\boldsymbol{x})\cdot\boldsymbol{u}(\boldsymbol{x}+\boldsymbol{r})\rangle|_{corr} = {}& \left[\frac{2}{r_1}\int_0^{\infty} \mathrm{d}k_1 \sin(2\pi k_1 r_1)\zeta_{dpT}(\boldsymbol{k}_1,\boldsymbol{p}_1,\boldsymbol{p}_2)\right.\\ & \left.-\frac{2}{r_1}\int_{L_o}^{\infty} \mathrm{d}k_1 \sin(2\pi k_1 r_1)\zeta_{dpS}(\boldsymbol{k}_1,\boldsymbol{p}_1,\boldsymbol{p}_2)\right]\\ & +\left[\frac{2}{r}\int_0^{\infty} \mathrm{d}k \sin(2\pi k r)\zeta_{SS}(\boldsymbol{k},\boldsymbol{p}_1,\boldsymbol{p}_2)\right.\end{aligned}$$

https://doi.org/10.1017/jfm.2020.827 Published online by Cambridge University Press

$$-\frac{2}{r}\int_0^{U_p} \mathrm{d}k\,\sin(2\pi kr)\zeta_{dpS}(\boldsymbol{k},\boldsymbol{p}_1,\boldsymbol{p}_2)\Bigg] + \frac{2}{r_1}\int_{L_o}^{(U\tau/L)^{\epsilon}} \mathrm{d}k_1\,\sin(2\pi k_1 r_1)\zeta_{dpS}(\boldsymbol{k}_1,\boldsymbol{p}_1,\boldsymbol{p}_2) + \frac{2}{r}\int_{(U\tau/L)^{\epsilon-1}}^{U_p} \mathrm{d}k\,\sin(2\pi kr)\zeta_{dpS}(\boldsymbol{k},\boldsymbol{p}_1,\boldsymbol{p}_2), \tag{C 7}$$

We designate the first two terms on the right-hand side of (C 7) as $\langle \boldsymbol{u}(\boldsymbol{x})\cdot\boldsymbol{u}(\boldsymbol{x}+\boldsymbol{r})\rangle|^{dpT-dpS}_{corr}$, the next two as $\langle \boldsymbol{u}(\boldsymbol{x})\cdot\boldsymbol{u}(\boldsymbol{x}+\boldsymbol{r})\rangle|^{SS-dpS}_{corr}$ and the last two $U\tau/L$-dependent terms as $\langle \boldsymbol{u}(\boldsymbol{x})\cdot\boldsymbol{u}(\boldsymbol{x}+\boldsymbol{r})\rangle|^{Div}_{corr}$ and evaluate them separately. Note that terms containing ϵ are now restricted to $\langle \boldsymbol{u}(\boldsymbol{x})\cdot\boldsymbol{u}(\boldsymbol{x}+\boldsymbol{r})\rangle|^{Div}_{corr}$. To obtain a leading-order ϵ-independent form from (C 7), we first evaluate $\langle \boldsymbol{u}(\boldsymbol{x})\cdot\boldsymbol{u}(\boldsymbol{x}+\boldsymbol{r})\rangle|^{Div}_{corr}$. This will also yield natural choices of L_o and U_p that are most convenient for the analysis.

After some algebra the $U\tau/L$-dependent terms on the right-hand side of (C 7) are expressible as

$$\langle \boldsymbol{u}(\boldsymbol{x})\cdot\boldsymbol{u}(\boldsymbol{x}+\boldsymbol{r})\rangle|^{Div}_{corr} = \frac{2(nL^3)^2D^3}{105\pi}\left\{Ci\left[2\pi r_1\left(\frac{U\tau}{L}\right)^{\epsilon}\right] - Ci\left[2\pi r_1 L_o\right] - j_0\left[2\pi r_1\left(\frac{U\tau}{L}\right)^{\epsilon}\right] + j_0\left[2\pi r_1 L_o\right] - Ci\left[2\pi r\left(\frac{L}{U\tau}\right)^{1-\epsilon}\right] + Ci\left[2\pi r U_p\right] - j_0\left[2\pi r U_p\right] + j_0\left[2\pi r\left(\frac{L}{U\tau}\right)^{1-\epsilon}\right]\right\}, \tag{C 8}$$

where *Ci* represents the cosine integral (Gradshteyn & Ryzhik 1980).

We use the additive method of constructing a uniformly valid approximation of (C 8) at leading order in ϵ (Van Dyke 1964; Subramanian & Brady 2006). To do so we simplify (C 8) in the inner ($r_1 \ll 1$ and $r \sim O(1)$), outer ($r_1 \sim O(1)$ and $r \gg 1$) and matching region ($r_1 \ll 1$ and $r \gg 1$) to construct the leading-order ϵ-independent form of $\langle \boldsymbol{u}(\boldsymbol{x})\cdot\boldsymbol{u}(\boldsymbol{x}+\boldsymbol{r})\rangle|^{Div}_{corr}$. We find that $L_o = U_p = 1$ is a convenient choice for the analysis, using which one gets

$$\langle \boldsymbol{u}(\boldsymbol{x})\cdot\boldsymbol{u}(\boldsymbol{x}+\boldsymbol{r})\rangle|^{Div}_{corr} = \frac{2(nL^3)^2D^3}{105\pi}\left\{\ln(2\pi r) - j_0\left[2\pi r\right] + \int_0^{2\pi r}\frac{\cos(t)-1}{t}\,\mathrm{d}t + j_0\left[2\pi r_1\right] - Ci\left[2\pi r_1\right] + \gamma_E\right\}, \tag{C 9}$$

where γ_E is the Euler–Mascheroni constant.

With L_o and U_p fixed, we now evaluate the remaining terms in (C 7). Following standard procedure presented in §§ 3.2 and 3.3, and additionally using (C 3), (C 4) and (C 6),

https://doi.org/10.1017/jfm.2020.827 Published online by Cambridge University Press

$\langle \boldsymbol{u}(\boldsymbol{x}) \cdot \boldsymbol{u}(\boldsymbol{x}+\boldsymbol{r})\rangle|_{corr}^{dpT-dpS}$ can be simplified as

$$\langle \boldsymbol{u}(\boldsymbol{x}) \cdot \boldsymbol{u}(\boldsymbol{x}+\boldsymbol{r})\rangle|_{corr}^{dpT-dpS} = (nL^3)^2 D^3 \left\{ \frac{3}{16\pi^2 r_1} \int_0^\infty \frac{1}{k_1} \sin(2\pi k_1 r_1)\, \mathrm{d}k_1 \right. \\ \times \int_{-1}^{1} \mathrm{d}\mu_1 \int_{-1}^{1} \mathrm{d}\mu_2 \frac{\mu_1^2 \mu_2^2 (1-\mu_1^2)(1-\mu_2^2)}{1+\pi^2 \left(\frac{U\tau}{L}\right) k_1^2 (\mu_2-\mu_1)^2} \\ \left. - \frac{2}{105\pi} \left[j_0(2\pi r_1) - Ci(2\pi r_1) \right] \right\}. \tag{C 10}$$

Similarly, using (3.21) for slender straight-swimmers, and (C 3) and (C 6) for straight-swimming point force-dipole swimmers, $\langle \boldsymbol{u}(\boldsymbol{x}) \cdot \boldsymbol{u}(\boldsymbol{x}+\boldsymbol{r})\rangle|_{corr}^{SS-dpS}$ can be written as

$$\langle \boldsymbol{u}(\boldsymbol{x}) \cdot \boldsymbol{u}(\boldsymbol{x}+\boldsymbol{r})\rangle|_{corr}^{SS-dpS} = \frac{(nL^3)^2 D^3}{\pi^2 r} \left\{ \int_0^1 \mathrm{d}k \int_{-1}^{1} \mathrm{d}\mu \left[\frac{3}{2\pi^4} \frac{\sin(2\pi k r)}{k^6} (1-\mu^2)^2 \sin(\pi k \mu) \right. \right. \\ \left. \times \left(j_o\left(\frac{\pi}{2} k\mu\right)^3 \right)^3 \sin^3\left(\frac{\pi}{2} k\mu\right) - \frac{1}{105} \frac{\sin(2\pi k r)}{k^2} \right] \\ + \int_1^\infty \mathrm{d}k \frac{\sin(2\pi k r)}{k^6} \int_{-1}^{1} \mathrm{d}\mu \frac{3}{2\pi^4} (1-\mu^2)^2 \left(j_o\left(\frac{\pi}{2} k\mu\right)^3 \right)^3 \\ \left. \times \sin^3\left(\frac{\pi}{2} k\mu\right) \right\}. \tag{C 11}$$

Now, given that the asymptotic form of the correlated component to the covariances, in the limit $U\tau/L \gg 1$, as stated below (C 6), is expressible as

$$\langle \boldsymbol{u}(\boldsymbol{x}) \cdot \boldsymbol{u}(\boldsymbol{x}+\boldsymbol{r})\rangle_{corr-matched} \equiv \langle \boldsymbol{u}(\boldsymbol{x}) \cdot \boldsymbol{u}(\boldsymbol{x}+\boldsymbol{r})\rangle|_{corr}^{SS-dpS} + \langle \boldsymbol{u}(\boldsymbol{x}) \cdot \boldsymbol{u}(\boldsymbol{x}+\boldsymbol{r})\rangle|_{corr}^{dpT-dpS} \\ + \langle \boldsymbol{u}(\boldsymbol{x}) \cdot \boldsymbol{u}(\boldsymbol{x}+\boldsymbol{r})\rangle|_{corr}^{Div}; \tag{C 12}$$

we get (3.31) on using (C 9)–(C 11) in (C 12). It is worth reiterating that while (3.27) is the exact expression for the velocity covariance valid for arbitrary $U\tau/L$, (3.31) is valid only for large $U\tau/L$. Note that in this regime, $\langle \boldsymbol{u}(\boldsymbol{x}) \cdot \boldsymbol{u}(\boldsymbol{x}+\boldsymbol{r})\rangle|_{corr}^{Div}$ is given by (C 9), and with $r_1 \equiv r * L/(U\tau)$, the weak decay arises from the $O(\ln[rL/(U\tau)])$ scaling of the $O(nL^3)^2$ term in the covariance, as stated in § 3.3.

REFERENCES

ALARCÓN, F. & PAGONABARRAGA, I. 2013 Spontaneous aggregation and global polar ordering in squirmer suspensions. *J. Mol. Liq.* **185**, 56–61.

ALARCÓN, F., VALERIANI, C. & PAGONABARRAGA, I. 2017 Morphology of clusters of attractive dry and wet self-propelled spherical particle suspensions. *Soft Matt.* **13** (4), 814–826.

ARANSON, I. S., SOKOLOV, A., KESSLER, J. O. & GOLDSTEIN, R. E. 2007 Model for dynamical coherence in thin films of self-propelled microorganisms. *Phys. Rev.* E **75** (4), 040901(R).

ARGUN, A., MORADI, A.-R., PINÇE, E., BAGCI, G. B., IMPARATO, A. & VOLPE, G. 2016 Non-Boltzmann stationary distributions and nonequilibrium relations in active baths. *Phys. Rev.* E **94** (6), 062150.

https://doi.org/10.1017/jfm.2020.827 Published online by Cambridge University Press

BALAKRISHNAN, V. 2008 *Elements of Nonequilibrium Statistical Mechanics*. Ane Books.

BATCHELOR, G. K. 1970 Slender-body theory for particles of arbitrary cross-section in Stokes flow. *J. Fluid Mech.* **44** (3), 419–440.

BERG, H. C. 2004 *E. coli in Motion*. Springer.

BERG, H. C. 1993 *Random Walks in Biology*. Princeton University Press.

BLAKE, J. 1973 A finite model for ciliated micro-organisms. *Trans. ASME: J. Biomech.* **6** (2), 133–140.

BLAKE, J. R. 1971 A spherical envelope approach to ciliary propulsion. *J. Fluid Mech.* **46** (1), 199–208.

BÁRDFALVY, D., NORDANGER, H., NARDINI, C., MOROZOV, A. & STENHAMMAR, J. 2019 Particle-resolved lattice Boltzmann simulations of 3-dimensional active turbulence. *Soft Matt.* **15** (39), 7747–7756.

CAFLISCH, R. E. & LUKE, J. H. C. 1985 Variance in the sedimentation speed of a suspension. *Phys. Fluids* **28** (3), 759–760.

CHEN, D. T. N., LAU, A. W. C., HOUGH, L. A., ISLAM, M. F., GOULIAN, M., LUBENSKY, T. C. & YODH, A. G. 2007 Fluctuations and rheology in active bacterial suspensions. *Phys. Rev. Lett.* **99** (14), 148302.

CLEMENT, E., LINDNER, A., DOUARCHE, C. & AURADOU, H. 2016 Bacterial suspensions under flow. *Eur. Phys. J.: Spec. Top.* **225** (11-12), 2389–2406.

COLIN, R., DRESCHER, K. & SOURJIK, V. 2019 Chemotactic behaviour of Escherichia coli at high cell density. *Nat. Commun.* **10**, 5329.

DELMOTTE, B., KEAVENY, E. E., CLIMENT, E. & PLOURABOUÉ, F. 2018 Simulations of Brownian tracer transport in squirmer suspensions. *IMA J. Appl. Maths* **83** (4), 680–699.

DOMBROWSKI, C., CISNEROS, L., CHATKAEW, S., GOLDSTEIN, R. E. & KESSLER, J. O. 2004 Self-concentration and large-scale coherence in bacterial dynamics. *Phys. Rev. Lett.* **93** (9), 098103.

DUNKEL, J., HEIDENREICH, S., BÄR, M. & GOLDSTEIN, R. E. 2013*a* Minimal continuum theories of structure formation in dense active fluids. *New J. Phys.* **15** (4), 045016.

DUNKEL, J., HEIDENREICH, S., DRESCHER, K., WENSINK, H. H., BÄR, M. & GOLDSTEIN, R. E. 2013*b* Fluid dynamics of bacterial turbulence. *Phys. Rev. Lett.* **110** (22), 228102.

EVANS, A. A., ISHIKAWA, T., YAMAGUCHI, T. & LAUGA, E. 2011 Orientational order in concentrated suspensions of spherical microswimmers. *Phys. Fluids* **23** (11), 111702.

FELDERHOF, B. U. 2016 Stokesian swimming of a prolate spheroid at low Reynolds number. *Eur. J. Mech.* B*/Fluids* **60**, 230–236.

FOKAS, A. S. & ABLOWITZ, M. J. 2012 *Complex Variables: Introduction and Applications*. Cambridge University Press.

GACHELIN, J., ROUSSELET, A., LINDNER, A. & CLEMENT, E. 2014 Collective motion in an active suspension of Escherichia coli bacteria. *New J. Phys.* **16** (2), 025003.

GAKHOV, F. D. 1966 *Boundary Value Problems*. Pergamon Press.

GELFAND, I. M. & SHILOV, G. E. 1964 *Generalized Functions, Volume 1, Properties and Operators*. AMS Chelsea Publishing.

GOLDFRIEND, T., DIAMANT, H. & WITTEN, T. A. 2017 Screening, hyperuniformity, and instability in the sedimentation of irregular objects. *Phys. Rev. Lett.* **118** (15), 158005.

GOLDSTEIN, R. E. 2015 Green algae as model organisms for biological fluid dynamics. *Annu. Rev. Fluid Mech.* **47**, 343–375.

GRADSHTEYN, I. M. & RYZHIK, I. S. 1980 *Table of Integrals, Series, and Products*, vol. 980. Academic Press.

GUASTO, J. S, RUSCONI, R. & STOCKER, R. 2012 Fluid mechanics of planktonic microorganisms. *Annu. Rev. Fluid Mech.* **44**, 373–400.

GUAZZELLI, E. & HINCH, J. 2011 Fluctuations and instability in sedimentation. *Annu. Rev. Fluid Mech.* **43**, 97–116.

GUO, S., SAMANTA, D., PENG, Y., XU, X. & CHENG, X. 2018 Symmetric shear banding and swarming vortices in bacterial superfluids. *Proc. Natl Acad. Sci. USA* **115** (28), 7212–7217.

HEIDENREICH, S., DUNKEL, J., KLAPP, S. H. L. & BÄR, M. 2016 Hydrodynamic length-scale selection in microswimmer suspensions. *Phys. Rev.* E **94** (2), 020601(R).

https://doi.org/10.1017/jfm.2020.827 Published online by Cambridge University Press

HINCH, E. J. 1988 Hydrodynamics at low Reynolds numbers: a brief and elementary introduction. In *Disorder and Mixing*, pp. 43–56. Springer.

ISHIKAWA, T. & PEDLEY, T. J. 2007*a* Diffusion of swimming model micro-organisms in a semi-dilute suspension. *J. Fluid Mech.* **588**, 437–462.

ISHIKAWA, T. & PEDLEY, T. J. 2007*b* The rheology of a semi-dilute suspension of swimming model micro-organisms. *J. Fluid Mech.* **588**, 399–435.

ISHIKAWA, T. & PEDLEY, T. J. 2008 Coherent structures in monolayers of swimming particles. *Phys. Rev. Lett.* **100** (8), 088103.

ISHIKAWA, T., SIMMONDS, M. P. & PEDLEY, T. J. 2006 Hydrodynamic interaction of two swimming model micro-organisms. *J. Fluid Mech.* **568**, 119–160.

JEPSON, A., MARTINEZ, V. A., SCHWARZ-LINEK, J., MOROZOV, A. & POON, W. C. K. 2013 Enhanced diffusion of nonswimmers in a three-dimensional bath of motile bacteria. *Phys. Rev.* E **88** (4), 041002(R).

KANAZAWA, K., SANO, T. G., CAIROLI, A. & BAULE, A. 2020 Loopy Lévy flights enhance tracer diffusion in active suspensions. *Nature* **579**, 364–367.

KASYAP, T. V., KOCH, D. L. & WU, M. 2014 Hydrodynamic tracer diffusion in suspensions of swimming bacteria. *Phys. Fluids (1994-present)* **26** (8), 081901.

KESSLER, J. O. 1986 Individual and collective fluid dynamics of swimming cells. *J. Fluid Mech.* **173**, 191–205.

KIM, M. J. & BREUER, K. S. 2004 Enhanced diffusion due to motile bacteria. *Phys. Fluids* **16** (9), L78–L81.

KIM, S. & KARRILA, S. J. 1991 *Microhydrodynamics: Principles and Selected Applications*. Butterworth-Henemann.

KOCH, D. L. & SHAQFEH, E. S. G. 1991 Screening in sedimenting suspensions. *J. Fluid Mech.* **224**, 275–303.

KOCH, D. L. & SUBRAMANIAN, G. 2011 Collective hydrodynamics of swimming microorganisms: living fluids. *Annu. Rev. Fluid Mech.* **43**, 637–659.

KRISHNAMURTHY, D. & SUBRAMANIAN, G. 2015 Collective motion in a suspension of micro-swimmers that run-and-tumble and rotary diffuse. *J. Fluid Mech.* **781**, 422–466.

KRISHNAMURTHY, S., GHOSH, S., CHATTERJI, D., GANAPATHY, R. & SOOD, A. K. 2016 A micrometre-sized heat engine operating between bacterial reservoirs. *Nat. Phys.* **12** (12), 1134.

KYOYA, K., MATSUNAGA, D., IMAI, Y., OMORI, T. & ISHIKAWA, T. 2015 Shape matters: near-field fluid mechanics dominate the collective motions of ellipsoidal squirmers. *Phys. Rev.* E **92** (6), 063027.

LADD, A. J. C. 1996 Hydrodynamic screening in sedimenting suspensions of non-Brownian spheres. *Phys. Rev. Lett.* **76** (8), 1392.

LADD, A. J. C. 1997 Sedimentation of homogeneous suspensions of non-Brownian spheres. *Phys. Fluids* **9** (3), 491–499.

LARSON, R. G. 2013 *Constitutive Equations for Polymer Melts and Solutions: Butterworths Series in Chemical Engineering*. Butterworth-Heinemann.

LAUGA, E. & POWERS, T. R. 2009 The hydrodynamics of swimming microorganisms. *Rep. Prog. Phys.* **72**, 096601.

LAXMINARSIMHARAO, V., GARG, P. & SUBRAMANIAN, G. 2020 Concentration banding instability of a sheared bacterial suspension. *Journal: J. Fluid Mech.* **904**, A7.

LEPTOS, K. C., GUASTO, J. S., GOLLUB, J. P., PESCI, A. I. & GOLDSTEIN, R. E. 2009 Dynamics of enhanced tracer diffusion in suspensions of swimming eukaryotic microorganisms. *Phys. Rev. Lett.* **103** (19), 198103.

LEVINE, A., RAMASWAMY, S., FREY, E. & BRUINSMA, R. 1998 Screened and unscreened phases in sedimenting suspensions. *Phys. Rev. Lett.* **81** (26), 5944.

LIN, Z., THIFFEAULT, J.-L. & CHILDRESS, S. 2011 Stirring by squirmers. *J. Fluid Mech.* **669**, 167–177.

LIU, Z., ZHANG, K. & CHENG, X. 2019 Rheology of bacterial suspensions under confinement. *Rheol. Acta* **58** (8), 439–451.

LOPEZ, H. M., GACHELIN, J., DOUARCHE, C., AURADOU, H. & CLEMENT, E. 2015 Turning bacteria suspensions into superfluids. *Phys. Rev. Lett.* **115**, 028301.

https://doi.org/10.1017/jfm.2020.827 Published online by Cambridge University Press

LUKE, J. H. C. 2000 Decay of velocity fluctuations in a stably stratified suspension. *Phys. Fluids* **12** (6), 1619–1621.

LUSHI, E., WIOLAND, H. & GOLDSTEIN, R. E. 2014 Fluid flows created by swimming bacteria drive self-organization in confined suspensions. *Proc. Natl Acad. Sci. USA* **111** (27), 9733–9738.

MACKAPLOW, M. B. & SHAQFEH, E. S. G. 1996 A numerical study of the rheological properties of suspensions of rigid, non-Brownian fibres. *J. Fluid Mech.* **329**, 155–186.

MAGGI, C., PAOLUZZI, M., PELLICCIOTTA, N., LEPORE, A., ANGELANI, L. & DI LEONARDO, R. 2014 Generalized energy equipartition in harmonic oscillators driven by active baths. *Phys. Rev. Lett.* **113** (23), 238303.

MARCHETTI, M. C., JOANNY, J.-F., RAMASWAMY, S., LIVERPOOL, T. B., PROST, J., RAO, M. & SIMHA, R. A. 2013 Hydrodynamics of soft active matter. *Rev. Mod. Phys.* **85** (3), 1143.

MARTINEZ, V. A., CLÉMENT, E., ARLT, J., DOUARCHE, C., DAWSON, A., SCHWARZ-LINEK, J., CREPPY, A. K., ŠKULTÉTY, V., MOROZOV, A. N., AURADOU, H., *et al.* 2020 A combined rheometry and imaging study of viscosity reduction in bacterial suspensions. *Proc. Natl Acad. Sci. USA* **117** (5), 2326–2331.

MEHANDIA, V. & NOTT, P. R. 2008 The collective dynamics of self-propelled particles. *J. Fluid Mech.* **595**, 239–264.

NAMBIAR, S., NOTT, P. R. & SUBRAMANIAN, G. 2017 Stress relaxation in a dilute bacterial suspension. *J. Fluid Mech.* **812**, 41–64.

NAMBIAR, S., PHANIKANTH, S., NOTT, P. R. & SUBRAMANIAN, G. 2019 Stress relaxation in a dilute bacterial suspension: the active–passive transition. *J. Fluid Mech.* **870**, 1072–1104.

NICOLAI, H., HERZHAFT, B., HINCH, E. J., OGER, L. & GUAZZELLI, E. 1995 Particle velocity fluctuations and hydrodynamic self-diffusion of sedimenting non-Brownian spheres. *Phys. Fluids* **7** (1), 12–23.

OTHMER, H. G., DUNBAR, S. R. & ALT, W. 1988 Models of dispersal in biological systems. *J. Math. Biol.* **26** (3), 263–298.

OYAMA, N., MOLINA, J. J. & YAMAMOTO, R. 2017 Do hydrodynamically assisted binary collisions lead to orientational ordering of microswimmers? *Eur. Phys. J.* E **40** (11), 95.

PATTESON, A. E., GOPINATH, A., PUROHIT, P. K. & ARRATIA, P. E. 2016 Particle diffusion in active fluids is non-monotonic in size. *Soft Matt.* **12** (8), 2365–2372.

PEDLEY, T. J. 2016 Spherical squirmers: models for swimming micro-organisms. *IMA J. Appl. Maths* **81** (3), 488–521.

PENG, Y., LAI, L., TAI, Y.-S., ZHANG, K., XU, X. & CHENG, X. 2016 Diffusion of ellipsoids in bacterial suspensions. *Phys. Rev. Lett.* **116** (6), 068303.

POEHNL, R., POPESCU, M. N. & USPAL, W. E. 2020 Axisymmetric spheroidal squirmers and self-diffusiophoretic particles. *J. Phys.: Condens. Matter* **32** (16), 164001.

PUSHKIN, D. O. & YEOMANS, J. M. 2014 Stirring by swimmers in confined microenvironments. *J. Stat. Mech.* **2014** (4), P04030.

QIAN, Y., KRAMER, P. R. & UNDERHILL, P. T. 2017 Stochastic kinetic theory for collective behavior of hydrodynamically interacting active particles. *Phys. Rev. Fluids* **2** (4), 043104.

RAMASWAMY, S. 2001 Issues in the statistical mechanics of steady sedimentation. *Adv. Phys.* **50** (3), 297–341.

RAMASWAMY, S. 2010 The mechanics and statistics of active matter. *Annu. Rev. Condens. Matter Phys.* **1** (1), 323–345.

SAINTILLAN, D. 2010 The dilute rheology of swimming suspensions: a simple kinetic model. *Exp. Mech.* **50**, 1275–1281.

SAINTILLAN, D. 2018 Rheology of active fluids. *Annu. Rev. Fluid Mech.* **50**, 563–592.

SAINTILLAN, D. & SHELLEY, M. J. 2007 Orientational order and instabilities in suspensions of self-locomoting rods. *Phys. Rev. Lett.* **99** (5), 058102.

SAINTILLAN, D. & SHELLEY, M. J. 2008 Instabilities and pattern formation in active particle suspensions: kinetic theory and continuum simulations. *Phys. Rev. Lett.* **100** (17), 178103.

SAINTILLAN, D. & SHELLEY, M. J. 2011 Emergence of coherent structures and large-scale flows in motile suspensions. *J. R. Soc. Interface* **9** (68), 571–585.

https://doi.org/10.1017/jfm.2020.827 Published online by Cambridge University Press

SEGRE, P. N., HERBOLZHEIMER, E. & CHAIKIN, P. M. 1997 Long-range correlations in sedimentation. *Phys. Rev. Lett.* **79** (13), 2574.

SIMHA, R. A. & RAMASWAMY, S. 2002 Hydrodynamic fluctuations and instabilities in ordered suspensions of self-propelled particles. *Phys. Rev. Lett.* **89** (5), 058101.

SOKOLOV, A. & ARANSON, I. S. 2009 Reduction of viscosity in suspension of swimming bacteria. *Phys. Rev. Lett.* **103** (14), 148101.

SOKOLOV, A. & ARANSON, I. S. 2012 Physical properties of collective motion in suspensions of bacteria. *Phys. Rev. Lett.* **109** (24), 248109.

SOKOLOV, A., GOLDSTEIN, R. E., FELDCHTEIN, F. I. & ARANSON, I. S. 2009 Enhanced mixing and spatial instability in concentrated bacterial suspensions. *Phys. Rev.* E **80** (3), 031903.

STENHAMMAR, J., NARDINI, C., NASH, R. W., MARENDUZZO, D. & MOROZOV, A. 2017 Role of correlations in the collective behavior of microswimmer suspensions. *Phys. Rev. Lett.* **119** (2), 028005.

SUBRAMANIAN, G. & BRADY, J. F. 2006 Trajectory analysis for non-brownian inertial suspensions in simple shear flow. *J. Fluid Mech.* **559**, 151–203.

SUBRAMANIAN, G. & KOCH, D. L. 2009 Critical bacterial concentration for the onset of collective swimming. *J. Fluid Mech.* **632**, 359–400.

SUBRAMANIAN, G. & NOTT, P. R. 2011 The fluid dynamics of swimming microorganisms and cells. *J. Indian I. Sci.* **91**, 283–313.

THIFFEAULT, J.-L. 2015 Distribution of particle displacements due to swimming microorganisms. *Phys. Rev.* E **92** (2), 023023.

TONER, J., TU, Y. & RAMASWAMY, S. 2005 Hydrodynamics and phases of flocks. *Ann. Phys.* **318** (1), 170–244.

TOPPALADODDI, S. & BALMFORTH, N. J. 2014 Slender axisymmetric Stokesian swimmers. *J. Fluid Mech.* **746**, 273–299.

UNDERHILL, P. T. & GRAHAM, M. D. 2011 Correlations and fluctuations of stress and velocity in suspensions of swimming microorganisms. *Phys. Fluids* **23**, 121902.

UNDERHILL, P. T., HERNANDEZ-ORTIZ, J. P. & GRAHAM, M. D. 2008 Diffusion and spatial correlations in suspensions of swimming particles. *Phys. Rev. Lett.* **100** (24), 248101.

VALERIANI, C., LI, M., NOVOSEL, J., ARLT, J. & MARENDUZZO, D. 2011 Colloids in a bacterial bath: simulations and experiments. *Soft Matt.* **7** (11), 5228–5238.

VAN DYKE, M. 1964 *Perturbation Methods in Fluid Mechanics*, vol. 964. Academic Press.

WENSINK, H. H., DUNKEL, J., HEIDENREICH, S., DRESCHER, K., GOLDSTEIN, R. E., LÖWEN, H. & YEOMANS, J. M. 2012 Meso-scale turbulence in living fluids. *Proc. Natl Acad. Sci. USA* **109** (36), 14308–14313.

WIOLAND, H., LUSHI, E. & GOLDSTEIN, R. E. 2016 Directed collective motion of bacteria under channel confinement. *New J. Phys.* **18** (7), 075002.

WOODHOUSE, F. G. & GOLDSTEIN, R. E. 2012 Spontaneous circulation of confined active suspensions. *Phys. Rev. Lett.* **109** (16), 168105.

WU, K.-T., HISHAMUNDA, J. B., CHEN, D. T. N., DECAMP, S. J., CHANG, Y.-W., FERNÁNDEZ-NIEVES, A., FRADEN, S. & DOGIC, Z. 2017 Transition from turbulent to coherent flows in confined three-dimensional active fluids. *Science* **355** (6331), eaal1979.

WU, X. L. & LIBCHABER, A. 2000 Particle diffusion in a quasi-two-dimensional bacterial bath. *Phys. Rev. Lett.* **84**, 3017–3020.

YANG, O., PENG, Y., LIU, Z., TANG, C., XU, X. & CHENG, X. 2016 Dynamics of ellipsoidal tracers in swimming algal suspensions. *Phys. Rev.* E **94** (4), 042601.

ZAID, I. M., DUNKEL, J. & YEOMANS, J. M. 2011 Lévy fluctuations and mixing in dilute suspensions of algae and bacteria. *J. R. Soc. Interface* **8** (62), 1314–1331.

ZWANZIG, R. 2001 *Nonequilibrium Statistical Mechanics*. Oxford University Press.

https://doi.org/10.1017/jfm.2020.827 Published online by Cambridge University Press